COMMUNICATIONS FOR CUBESAT NETWORKS AND FRACTIONALISED SPACECRAFT

PHILIPPOS KARAGIANNAKIS

SUBMITTED IN FULFILMENT OF THE REQUIREMENTS FOR THE DEGREE OF
Doctor of Philosophy

CENTRE FOR SIGNAL & IMAGE PROCESSING

DEPARTMENT OF ELECTRONIC & ELECTRICAL ENGINEERING
UNIVERSITY OF STRATHCLYDE

MAY 2017

Declaration

This thesis is the result of the author's original research. It has been composed by the author and has not been previously submitted for examination which has led to the award of a degree.

Signed:

Date:

Abstract

The use of low-cost CubeSats in the context of satellite formation flying appears favourable due to their small size, relatively low launch cost, short development cycle and utilisation of commercial off the shelf components. However, the task of managing complex formations using a large number of satellites in Earth orbit is not a trivial one, and is further exacerbated by low-power and processing constraints in CubeSats. With this in mind, a Field Programmable Gate Array (FPGA) based system has been developed to provide next generation on-board computing capability. The features and functionality provided by this on-board computer, as well as the steps taken to ensure reliability, including design processes and mitigation techniques are presented in this work and compared to state of the art technology.

Coupling reliable formation flying capabilities with the possibility of producing complex patterns using spacecraft will enable the potential of grouping a number of antenna elements into a cooperative structure. The key point in the exploitation of formation flying techniques for the deployment of an antenna array is that the performance of a homogeneous pattern of array elements can be matched or surpassed by fractal geometries. This thesis analyses the Purina fractal array when utilised for beamforming. A new metric termed power concentration is introduced, which assesses the power dissipated within a cone aligned with the array's look direction, i.e. an assessment how much of the radiated power will reach a specific foot print. Using this metric the performance for beamformers of varying complexity can be compared, independent of the number of sensor elements used to form the array and across a range of frequencies. Furthermore the robustness of the array with respect to element displacement and failure is investigated.

The fractionated nature of such a satellite network and the low-power nature of the nodes motivates distributed processing when using such an array as a beamformer. By mirroring the fractal structure in the processing architecture, the proposed idea demonstrates that benefits such as strictly limited local processing capability independent of the array's dimension and local calibration can be bought at the expense of a slightly increased overall cost.

Acknowledgements

Firstly, I would like to thank my supervisor, Dr Stephan Weiss, for giving me the opportunity to experience life in research and supporting me over the course of this Industrial PhD. Your unwavering positivity and dedication throughout has been a constant source of inspiration. I would also like to give special thanks to Professor Bob Stewart, without whom this journey would never have happened.

The road to space is not a trivial one and is one best done in the company of others. To my industrial supervisor Jamie Bowman, thank you for offering me such an interesting opportunity, your guidance along the way was instrumental in helping me reach my goals. To my fellow MIC team mates Gregour, Neil, John and Rakesh at Steepest Ascent, the long hours and hard work were worth it in the end. You all had a profound impact on my work then and now, I am grateful for your support and influence.

I have come to realise the importance of friendship during the ups and downs that a PhD is often filled with. To Giulano Punzo, an opportunity to publish brought us together but the coffee kept us sane. Thanks for all the breaks and tangential conversations.

Acronyms

ADCS	Attitude Determination and Control Subsystem
AHB	Advanced High-performance Bus
AMBA	Advanced Microcontroller Bus Architecture
APB	Advanced Peripheral Bus
APF	Artificial Potential Function
CDH	Command and Data Handling
Cal Poly	California Polytechnic State University
COTS	Commercial Off The Shelf
DSP	Digital Signal Processing
ECC	Error Correcting Code
EDAC	Error Detection and Correction
ESA	European Space Agency
FPGA	Field Programmable Gate Array
GEO	Geostationary Earth Orbit
GENSO	Global Educational Network for Satellite Operations
HPEC	High Performance Embedded Computing
ITU	International Telecommunications Union
LEO	Low Earth Orbit

MEO	Medium Earth Orbit
MIC	Mission Interface Computer
OBC	On-Board Computer
OTP	One Time Programmable
PCB	Printed Circuit Board
P-POD	Poly PicoSatellite Orbital Deployer
PPM	Pluggable Processor Module
PPS	Pulse Per Second
PROM	Programmable Read Only Memory
RAM	Random Access Memory
ROM	Read Only Memory
RTOS	Real Time Operating System
SEE	Single Event Effect
SET	Single Event Transient
SEU	Single Event Upset
SMD	Surface-Mount Device
SoC	System on Chip
SDRAM	Synchronous Dynamic Random Access Memory
SRAM	Static Random Access Memory
SSTL	Surrey Satellite Technologies Limited
TID	Total Ionising Dose
TMR	Triple Modular Redundancy
UKSA	United Kingdom Space Agency

Table of Contents

Declaration

Abstract

Acknowledgments

List of Tables

List of Figures

Chapter 1

Introduction

CubeSats are satellites of low weight and small size, typically weighing no more than 1 kg and coming in a cube no bigger than $10 \times 10 \times 10$ cm [1, 2, 3]. This is commonly referred to as 1-Unit or 1 U and these can be built up in a modular fashion to produce larger more capable spacecraft. The idea for CubeSats was initially conceived in 1999 by professors at Cal-Poly and Stanford Universities. Their intention was to provide a cheap platform that could be used to introduce students to the practicalities of designing and developing for space. Initially made popular due to their low-cost and short development cycles, the growth of the CubeSat market has been considerable over the last few years. From their simple beginnings as an educational tool and a technology demonstration platform, CubeSats are now used increasingly for gathering Earth observation and environmental monitoring data.

1.1 Overview

CubeSats provide a low cost platform for spacecraft design and development. Much of the cost reduction achieved is a direct result of size and weight restrictions and is further aided by reduced development cycles and use of Commercial Off The Shelf (COTS) components. Unfortunately, as well as driving down the cost, such restrictions have resulted with many past missions being limited to very basic functionality. With improvements in technology and a better understanding of nano-satellite behaviour in Low Earth Orbit (LEO), the ability of CubeSats to perform evermore complex functions is increasing. One method of improving the functionality of CubeSats without impacting on their desired size or weight is to connect them together in a network and allow them to share processing and communication resources. Sharing tasks and processing power across many CubeSats, circumvents some of the negative effects imposed due to form size.

There is currently wide spread interest in the notion of fractionalised spacecraft. The term fractional spacecraft entails splitting up the functional and operational aspects of a large satellite across a network of smaller satellites flying in formation. The benefits of this approach are: lower development and replacement costs and using a modular platform (such as a CubeSats) makes expansion to accommodate extra functionality possible. Additionally, spreading sensors spatially and temporally allows a wider range of measurements to be taken and by spreading the responsibility of one system across a number of smaller satellites failure of one satellite does not necessarily jeopardise the mission objectives.

CubeSats offer an ideal platform on which to design and implement a fractionalised spacecraft. The added complexities and overheads incurred in setting up and maintaining a satellite network could be viewed as a possible drawback to this method. However, ability to improve functionality or replace old or deteriorated subsystems at a fraction of the cost of a new satellite would be the realisation of a sustainable space based system.

This thesis investigates the application of CubeSats within a fractionated fractal beamformer. Coupling reliable formation flying capabilities with the possibility of producing complex fractal patterns using spacecraft enables the potential of grouping a number of independent antenna elements into a cooperative structure. From a control and performance point of view, the self-similarity of fractal geometries coupled with the resulting large spatial apertures of relatively few elements, make them good candidates for the implementation of a distributed beamformer array.

1.2 Context of this Work

CubeSats

CubeSats are widely regarded amongst the small satellite community as a platform that has the potential for great achievements in the coming years. The pressure on these tiny spacecraft to perform as well as their larger siblings is increasing and mission developers expect CubeSats to be able to meet very demanding performance levels. This is a change in perspective from previous assessments where CubeSats were seen as having limited functionality, and this optimism comes with increased pressure on CubeSat technology developers to provide this performance whilst still hitting the low cost expectations of the CubeSat form factor. Since the introduction of the CubeSat standard the number of off the shelf subsystems available to developers has increased annually. Moreover, the performance and functionality have increased while the size and weight have decreased, meaning more capable satellites are being launched every year. Although a wide range of comparable products are available, there is a need for a high performance on-board computing subsystem able to handle the extra processing and storage needed to implement and manage a formation of CubeSats. With this in mind, a Field Programmable Gate Array (FPGA) based on-board computer has been developed by Steepest Ascent to provide next generation on-board computing capability. The features and functionality provided by this on-board computer, as well as the steps taken to ensure reliability, including design processes and mitigation techniques are presented in this work and compared to state of the art technology.

Fractal Formation Flying

The value of exploiting formation flight techniques for space science, remote sensing and telecommunications applications is gaining popularity. So far proposed formation flying concepts have been based on a relatively low number of cooperating spacecraft, as in the case of Lisa, Proba-3 or StarLight missions. The exploitation of a formation flight architecture with an increased number of elements which maintains an acceptable level of system complexity can be pursued through the control of autonomous and independent agents as a single group entity.

Fractal Geometry and Beamforming

Coupling reliable formation flying capabilities with the possibility of producing complex patterns using spacecraft will enable the potential of grouping a number of antenna elements into a cooperative structure. This has long been known and applied in antenna array theory [4, 5] and proposed at conceptual level for space applications [6, 7, 8].

The key point in the exploitation of formation flying techniques for the deployment of an antenna array is that the performance of a homogeneous pattern of array elements can be matched or surpassed by fractal geometries as per [9] and [10]. Fractal geometries as defined by [9] can be considered self-similar structures propagated from a core initiator through a number of stages of growth by an identical generator. Application of fractal geometries in antenna array design has mainly focussed on single structures, that is to say one device housing the antenna array. In this context each satellite houses an antenna which contributes to form the fractal pattern. Hence, the problem turns into producing a fractal pattern from a formation of spacecraft which provides a platform for a number of array elements able to exploit the fractal pattern characteristics.

1.3 Original Contributions

This thesis investigates the viability of flying CubeSats in a fractal formation to implement a distributed beamformer. The main contributions of this work are considered to be the following:

- The design of a high performance embedded computing platform for a CubeSat — Mission Interface Computer (MIC):
  - The size, mass and power restrictions of a CubeSat as well as the space environment present a challenge for implementing such a high performance subsystem. The design of the MIC examined each of these aspects with the view to providing an innovative solution for the CubeSat platform, including the use of a FLASH based Field Programmable Gate Array (FPGA) System on Chip (SoC) and failure mitigation techniques; the first On-Board Computer (OBC) to offer such capabilities.
  - The MIC formed part of UKube-1, the maiden space mission for the United Kingdom Space Agency (UKSA) and the first CubeSat missions to be built and operated by the UK.
- The realisation of a control method to enable complex fractal formations to be achieved, provided the impetus to investigate for the first time a distributed beamformer based on a fractal geometry.
- An assessment of the performance characteristics of the Purina fractal array as a distributed beamformer.
- A new metric *power concentration* provided the means to minimise the number of variables used when comparing different 2D and 3D beamforming arrays.
- Using the *power concentration* metric to perform a comparison of the Purina beamformer versus full-lattice arrays of equivalent complexity and spatial aperture.
- The distributed processing to match the group-based control methods revealed a promising path in future investigations of the self-similar fractal array.

1.3.1 Papers Authored

- **Philippos Karagiannakis**, Jamie Bowman, Stephan Weiss, John O'Sullivan. CubeSat Networks for Fractionalised Spacecraft- A Review. 1st International Academy of Astronautics (IAA) Conference in University Satellite Missions and CubeSat Workshop in Europe. 24 - 29 January 2011, Rome, Italy.

- **Philippos Karagiannakis**, Stephan Weiss, Jamie Bowman. Solving the digital signal processing problem for CubeSats. 4th European CubeSat Symposium. 30 January - 1 February 2012, Brussels, Belgium.
- **Philippos Karagiannakis**, Jamie Bowman, Craig Clark, Stephan Weiss. Advanced FPGA Computing for small and nano-satellites. The 2012 4S Symposium - Small Satellite Systems and Services, European Space Agency (ESA). 4 - 8 June 2012, Portoroz, Slovenia.
- Giuliano Punzo, **Philippos Karagiannakis**, Derek J. Bennet, Malcolm Macdonald, Stephan Weiss. Enabling and Exploiting Self similar formations. IEEE Transaction on Aerospace and Electronic Systems. 2014 Jan; 50(1):689-703.
- **Philippos Karagiannakis**, Stephan Weiss, Giuliano Punzo, Malcolm Macdonald, Jamie Bowman, Robert Stewart. Impact of Purina Fractal Array Geometry on Beamforming Performance and Complexity. 21 st European Signal Processing Conference. 9 - 13 September 2013, Marrakech, Morocco.
- **Philippos Karagiannakis** and Stephan Weiss. Analysis of a Purina Fractal Beamformer. 2013 Asilomar Conference on Signals, Systems and Computers. 3 - 6 November 2013, California, USA.
- **Philippos Karagiannakis**, Keith Thompson, Jamie Corr, Iain K Proudler, Stephan Weiss. Distributed Processing of a Fractal Array Beamformer. Intelligent Signal Processing Conference 2013, Institution of Engineering and Technology. 2-3 December 2013, London, UK.

1.4 Thesis Outline

This thesis presents contributions to the delivery of fractionated fractal beamformer, using CubeSats as array elements.

Chapter 1 introduces the CubeSat technological challenges as the motivation for this work and provides an overview of the contributions and organisation of the thesis.

Chapter 2 provides a history of CubeSats and their popularity. Included in this chapter are the challenges faced by satellite developers, framed in the context of the CubeSats. A discussion on the future roadmap for CubeSats is presented.

Chapter 3 aims to solve the on-board processing problem plaguing many CubeSat missions. A new FLASH FPGA-based architecture designed to cope with space is presented and compared against state of the art.

Chapter 4 opens the discussion to formation flying and introduces the control method for achieving complex formations such as fractals. The use of a Purina fractal formation and its application as an antenna array are discussed.

Chapter 5 provides further analysis of the Purina fractal beamformer and compares it with full-lattice arrays of equal spatial aperture and complexity. A real benefit of fractionated spacecraft is the loss of a single satellite or array element should not translate to a total loss of the mission. Distributing the beamformer control in a similar fashion to the control is analysed.

Chapter 6 summarises the contributions within this thesis and discusses potential future research directions.

1.5 Mathematical Notation

In this thesis vectors and matrices are denoted by lowercase and uppercase bold face variables, respectively. For two vectors $\mathbf{x}$ and $\mathbf{y}$, $\mathbf{x} \cdot \mathbf{y}$ is the scalar product. The first and second derivatives of a function x with respect to time are, respectively, denoted by $\dot{x}$ and $\ddot{x}$. Finally, a linear approximation of a function f at a given point is represented by $\tilde{f}$.

Chapter 2

Cube Satellites — State of the Art for Operation and Functionality

2.1 Introduction

This chapter provides a context for the research discussed in this thesis. The chapter begins by introducing the concept of CubeSats and the technology required to operate them. The challenges faced when designing for space are explained. An overview of some notable past missions is provided, before the future of CubeSat technologies and their applications are discussed, setting the scene for the remainder of the work presented in this thesis.

2.2 Motivation for CubeSats

Since their introduction a little over 10 years ago a form of nano-satellites known as CubeSats have proved popular in both academic and commercial fields. Although miniature satellites (< 100 kg) have existed for a number of years, the notion and realisation of a nano-satellite (< 10 kg) is relatively new with the first nano-satellite launched in 2000 and the first six CubeSat missions launched in 2003. The CubeSat format was initially developed by professors at Stanford University and California Polytechnic State University (Cal Poly) to help students gain experience in space technology and exploration [11]. Through their collaboration they defined the CubeSat Standard [12] which incorporates restrictions and guidance on key structural, mechanical and electrical requirements. The standardisation process also resulted in a common orbital deployment mechanism, which could be adapted to a number of launch vehicles, and ultimately provided an affordable means to access space.

A key factor in making the CubeSat platform viable for academic institutions is the huge

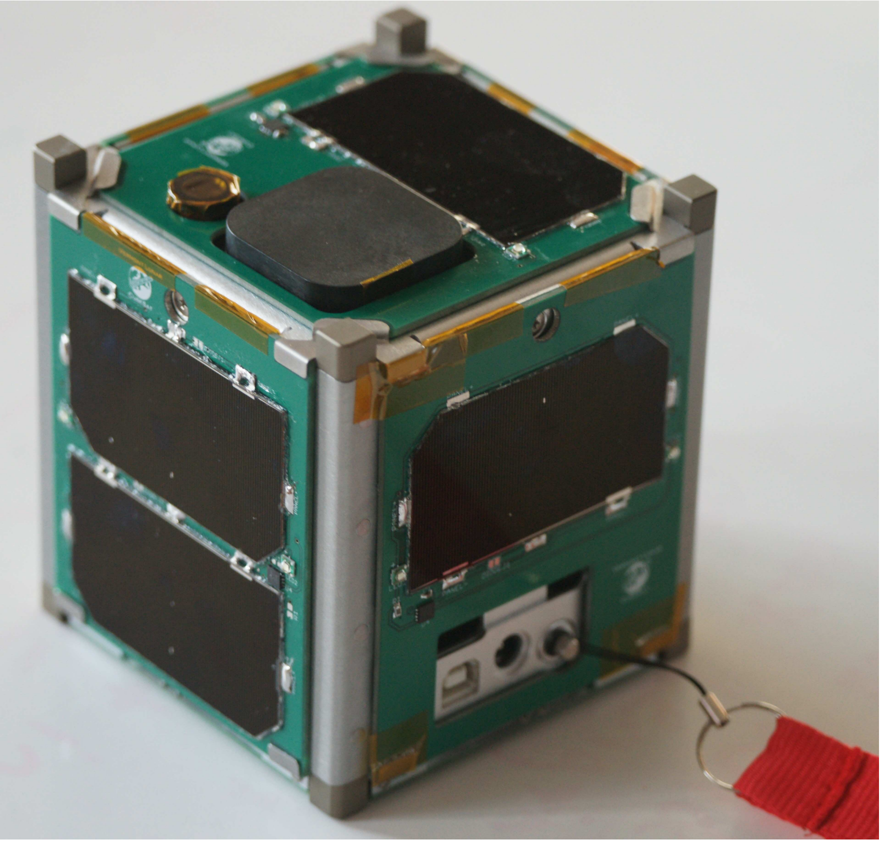

Figure 2.1: Pictured here is an assembled 1U CubeSat [13].

reduction in costs achieved as a result of size and weight restrictions. The standard CubeSat model, often referred to as a 1-Unit or 1U, measures $10 \times 10 \times 10$ cm and weighs < 1.33 kg; Fig. 2.1 shows a fully assembled 1U CubeSat complete with solar arrays and exposed patch antenna. The standard 100 cm^2 area of the satellite face allows for a common deployment system. This launch system is called the Poly PicoSatellite Orbital Deployer (P-POD) and is shown in Fig. 2.2. The common deployment mechanism is in place to protect the primary payload, on which CubeSats hitch a ride to space, ensuring that any CubeSat malfunction is not detrimental to the main payload. The rudimentary spring operated launch mechanism is visible in the image. CubeSats are simply inserted into the P-Pod launcher. The door is closed and will only open at a pre-specified altitude. Once the door opens the spring mechanism simply pushes the contained CubeSats out the door opening into their rough orbit.

Traditionally (larger) satellites are built with reliability as a top priority [11, 15]. This results in lengthy development cycles and the use of expensive space-rated components. The experimental nature of CubeSats as a low-cost means to access space means that a failed spacecraft is not necessarily a failed mission. This freedom to fail allows developers to try new techniques, ideas, processes and technology. In fact CubeSat developers embrace a Commercial Off The Shelf (COTS) approach, trading reliability for performance in many cases, lowering costs further and shortening development cycles making the launch and op-

Figure 2.2: Pictured here is the Poly-PicoSatellite Orbital Deployer (P-POD) launch mechanism for CubeSats [14].

eration even more affordable. As a result of their compactness and approach to design, the cost to develop and launch a 1U CubeSat within an academic environment is approximately $ 250,000 [16]. In comparison NigeriaSat-1, a miniature commercial satellite based on the popular Microsat-100 [17] platform bus from Surrey Satellite Technologies Limited (SSTL), costed $ 13-million to develop and launch in 2003 [18] — the same year as the first CubeSat launches.

Their low cost factor and small time frame to develop has made CubeSats increasingly attractive, as is evident from the graph of launches shown in Fig. 2.3. This popularity has resulted in a rapid growth of the CubeSat developer market. Already there are over 100 well established suppliers [19] offering a range of services to help anyone looking to access space via this low cost route — they offer bespoke components/subsystems up to full platform and launch services. Many of these companies were formed as spin-outs from universities where a successful mission was launched and operated from. Others, like Clyde Space based in Glasgow, realised early on the potential of CubeSats and positioned themselves to take advantage of the rapidly expanding market. Regardless of their origins, these pioneers have helped pave the way for more complex and robust satellites and missions. Today, the CubeSat market is estimated to be worth 50 million pounds sterling and projected to increase to over 200 million pounds sterling in the next 20 years [20, 21].

Despite their compactness, developers have demonstrated the versatility and capability of CubeSats on a large variety of missions. The initial six CubeSats launched in 2003 provided a glimpse of their potential, demonstrating their usefulness as technology demonstrators (CanX-1)[22], tether research (DTUsat)[23], Earth imaging (AAU CubeSat)[24], earthquake detection (QuakeSat)[25] and amateur radio (CUTE-I,CubeSat XI-IV)[26]. The success of these initial missions, bolstered by the steadily increasing number of suppliers reducing costs and risks, further highlighted the potential of CubeSats to commercial and national

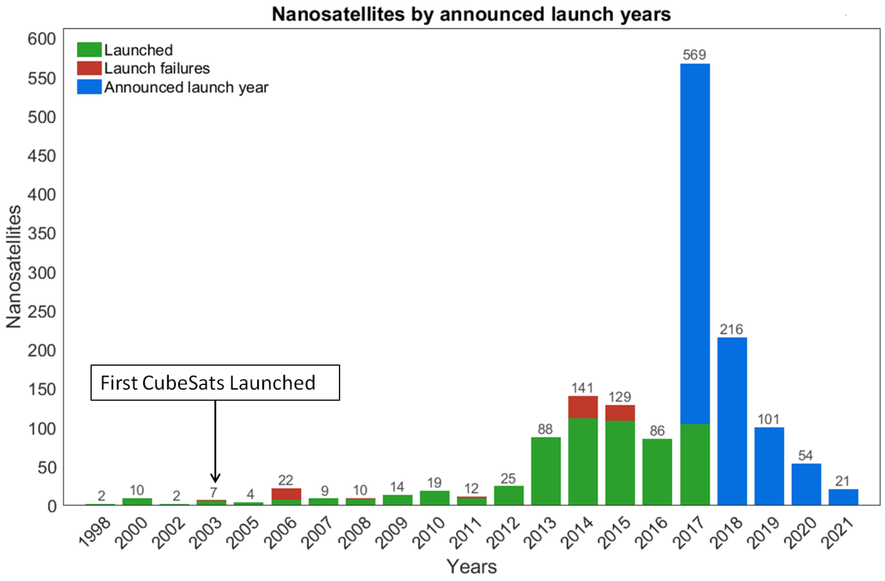

Figure 2.3: Nano-Satellite Launches [19].

organisations. By 2006 NASA in partnership with Santa Clara University had successfully launched and operated the first CubeSat-based biological research mission (GeneSat-1)[27]. Liberation from the fear of failure combined with a quick turnaround and access to new technology has inspired many innovative missions. CubeSat mission goals cover a broad range of topics:

- technology demonstrators;
- Earth remote sensing;
- ionospheric and auroral research;
- astrobiology — effects of space environment on biological systems;
- radiation effects on space technologies;
- astrophysics.

The meteoric rise of the CubeSat and the supporting commercial entities has helped these small satellites cement their place in the future of space exploration. In line with similar technologies, such as personal computers and mobile phones, CubeSats will continue to offer increasing levels of performance coupled with more reliable and robust devices. Their success has helped to launch even smaller form satellites known as PocketQube [28] and ChipSats [29]. The initial scepticism of the space community has been replaced by a genuine interest in using nano-satellites for proper space experiments. Although initial satellites were rudimentary in their design, a decade after the first launches, these nano-satellites are offering a high level of sophistication in conjunction with increased reliability and robustness. In the next section the mission and operational aspects of a CubeSat mission are presented.

2.3 CubeSat Components

Satellites are available in a large variety of types and sizes. Tab. 2.1 provides a general classification of satellites. Despite the evident variability in satellite form and function, CubeSats share many of the same features and design attributes as more traditional satellites. The multiple elements which combine to form a spacecraft can be grouped into two main categories: the platform and payload systems. The payload covers all the spacecraft hardware and software used to achieve the mission objectives. The payload may consist of one or multiple sensors required to perform mission specific goals; these could range from a simple temperature sensor to a high resolution camera.

Class	Mass	Example	Orbit	Application
large satellite	$\geq$ 1000 kg	GPS	Medium Earth Orbit	Global Positioning System
small satellite	500 - 1000 kg	Iridium	Low Earth Orbit	Communications
minisatellite	100 - 500 kg	EROS-B	Low Earth Orbit	Earth Observation
microsatellite	10 - 100 kg	AprizeSat-3	Low Earth Orbit	Automatic Identification System
nanosatellite	$\leq$ 10 kg	UKube-1	Low Earth Orbit	Technology Demonstrator

Table 2.1: Satellite classification

The platform, or spacecraft bus, covers all the spacecraft subsystems needed to support the payload. These subsystems perform the on-board data handling, power generation and management, communications, orientation and payload management. Depending on the mission-specific goals, subsystem performance can be traded off against one another, however as there are usually strict constraints these must be carefully considered.

2.3.1 Payload Systems

Primary payload is used to identify those subsystems within the payload which will provide the primary mission objectives for the spacecraft once on-orbit. The payload is of course the motivation for the mission itself. In order that this may function it requires certain resources

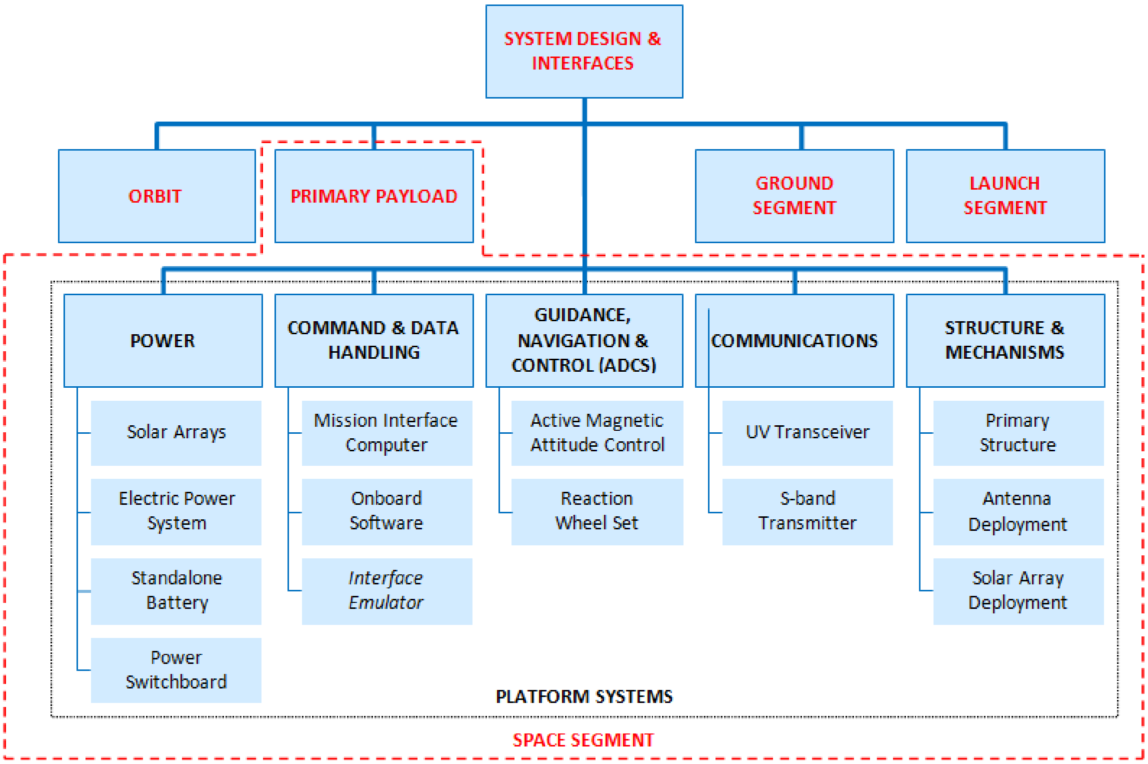

Figure 2.4: Typical satellite mission and systems diagram.

that will be provided by the platform bus. In particular, it is possible to identify the functional requirements, which include:

- the payload must be pointed in the correct direction;
- the payload must be operable;
- the data from the payload must be communicated to the ground;
- the desired orbit for the mission must be maintained;
- the payload must be held together, and onto the platform on which it is mounted;
- the payload must operate and be reliable over some specified period;
- an energy source must be provided to enable the above functions to be performed.

These requirements lead to a breakdown into subsystems, as shown in Fig. 2.4. The individual subsystems that make up the platform are discussed in the following section. An important point in designing any of these subsystems is the impact and resource implication this has on others.

2.3.2 Platform Subsystems

Power Subsystem

The power system provides all the power generation, storage, and distribution for the spacecraft. The provision of electrical power for a spacecraft is one of its most fundamental requirements. Failure of the power system necessarily results in the loss of the space mission. The power system consists of three main elements: a power distribution and control subsystem as well as primary and secondary power sources. The primary power source is concerned with generating electrical power, which usually takes the form of converting either fuel or solar radiation into electrical energy. The majority of modern satellites use solar arrays as the primary energy source, converting solar radiant energy via the photovoltaic effect to electrical energy.

The secondary energy source is required to store energy for periods when the primary energy source is unavailable — this would be during eclipses in the case of solar arrays as primary source. Requirements on power subsystems for Low Earth Orbit (LEO) and Geostationary Earth Orbit (GEO) are notably different due to the different eclipse profiles experienced in these orbits. Satellites in LEO have a maximum orbit time of 127 minutes, of this they can spend up to 35 minutes in eclipse and need oversized solar arrays to meet battery charging requirements. Satellites in GEO are almost always in sunlight, only experiencing eclipses for a short periods before/after seasonal equinoxes and due to lunar eclipses. These eclipses may last up to 70 minutes of a 24 hour day, leading to a deep battery discharge but the amount of time spent in sunlight afterwards is much higher when compared to LEO satellites, thus giving the GEO satellites a larger time period to recharge their batteries. Despite this the use of batteries as energy storage devices offers the highest efficiency for the majority of satellites.

The power distribution fulfils a number of roles. It acts as a power switchboard to allow on/off switching of payload and auxiliary secondary power lines at the same voltages as the primary power lines. It detects and handles power surges, ensuring that the correct power levels are delivered to the platform and payload systems irrespective of which power source is currently used. Finally it controls the battery charging system, which alongside monitoring the health of the battery controls the charging and discharging of the battery. This is a particularly important role as it helps to maintain battery health, thus extending its lifetime.

Command & Data Handling Subsystem

The Command and Data Handling (CDH) subsystem is the primary interface point between the platform and the payloads, providing the functionality to allow two-way flow of information between the ground station and the satellite. On the uplink, it receives commands from the ground station via the communications system and routes them to the appropriate components and payloads. On the downlink, it collects and stores telemetry from across the system, and forwards it along with any other payload or real-time data to the ground via the communications system.

Although the payload of a satellite is the principle performance driver for the spacecraft, the platform control functionality plays a significant role in the sophisticated capabilities of CubeSats. The CDH system is made up of the flight processor (running the platform- and application-software), memory (both volatile and non-volatile), interface controllers, on-board timers and reconfiguration modules. The primary flight processor on the CDH system is usually running a real-time multi-tasking operating system performing various tasks ranging from payload operations and basic housekeeping functions, up to sophisticated attitude control and orbit maintenance. There are often secondary processing capabilities used to off-load computing intensive tasks or act as a backup in case of the primary processor failing. The non-volatile memory is used to store platform and application software as well as housekeeping/telemetry and payload data for downlink to ground station. The volatile memory is used to store the flight control software once it is loaded up. Often these memories are ’protected from’/’made more robust to’ the radiation environment of space by error correction methods — these are detailed in Sec. 2.4.1. The interface between the various subsystems are usually controlled by the CDH, it arbitrates buses and ensures data is moved about safely and efficiently. The CDH usually maintains the master clock for the satellite, often providing synchronisation signals and redundancy or backup clock capabilities.

Communications Subsystem

All spacecraft include some form of communications functionality. On a CubeSat communications are primarily used for telemetry, tracking and control in support of satellite operations, and for the downlink transmission of payload generated data. The communication subsystem consists of the radio transmitter and receiver as well as any associated hardware, such as antennas, used to communicate with the ground (or other spacecraft). The transmitter and receiver portions of the communications system include the hardware for bandpass filtering, low-noise amplifier to boost weak received signals, frequency mixer and power amplifier to boost the downlink signal to ground.

CubeSat communication systems have developed significantly since their inception. Early communication was carried out using available amateur radio technology mainly in the UHF band [30], ranging from 435 - 438 MHz. The frequencies and technology called for rudimentary equipment such as whip or extending tape antennas and implemented protocols such as the AX-25 [31]. This often resulted in low data rates and reliability, but provided the early developers with ready to use off the shelf equipment and access to a worldwide network of ground stations keen and able to help track CubeSats — this was especially important during the initial phases of a launch. Today's CubeSats often have a high-speed downlink implemented utilising S- and X-band transmitters, increasing downlink rates to over 1 Mbps. Although these offer much higher data rates, the increase in performance requires: (i) more expensive equipment, (ii) higher transmit power and (iii) ground stations with larger antennas and higher pointing accuracy, meaning this technology is not always suitable for every mission.

Attitude Determination and Control Subsystem

The performance of the communication system and operation of many observational payloads are directly linked to the ability of the satellite to point at specific locations on Earth or other targets. The Attitude Determination and Control Subsystem (ADCS) encompasses all components needed for orbit and attitude determination and control, and ultimately the positioning and pointing of the spacecraft for the mission. The ADCS must be able to overcome the disturbance torques experienced during the satellite's orbit in order to control the angular momentum of the satellite.

The fundamental driving requirement for ADCS is the pointing control, typically driven by how accurately the payload must be pointed. How accurately the spacecraft must point will impact on the accuracy of the sensors and the precision of the actuators. The actuators provide the torque to re-point the spacecraft. The most stringent constraints for the ADCS are mass, power, and volume. The sensors and actuators add significant mass to the system, and the software required to control a spacecraft's attitude can consume a major portion of the processor bandwidth. Typically, more accurate sensors are heavier and more expensive, consume more power and have a lower reliability — generally more complexity is required for more accuracy.

In addition to pointing the spacecraft towards communications or payload targets the ADCS subsystem is responsible for maximising the solar energy incident on the solar arrays. The ADCS subsystem has the on-board knowledge of attitude, which when combined with the position of the Sun in relation to the Earth, generate the proper commands to the hardware to point the antenna and solar panel.

Attitude determination is provided by a three-axis magnetometer, which is used to measure the Earth's magnetic field. The control is often implemented as part of the OBC software and uses one of several different technologies to enable the ADCS to control the satellite's attitude in orbit. These range from relatively simple magnetic controls to more complex momentum wheels and pressurized gas thrusters. Magnetic control requires no moving or deployable parts, is lightweight and can be designed to use little power, making it attractive considering the design constraints of CubeSats. To control a satellite's attitude in orbit, three magnetic coils are mounted, perpendicular to each other, on three sides of the satellite. When powered, the torque produced by the electromagnets tries to align with the Earth's magnetic field. Despite the considerable power consumption of the ADCS, the overall impact on the power budget is relatively low as the ADCS is only turned on for a short time each orbit.

Structure and Mechanisms

Structure & Mechanisms encompasses both the structure of the spacecraft, and the electronic/mechanical systems needed for achieving or maintaining the mission configuration. The spacecraft structure supports all the spacecraft components and payloads throughout the launch, and it provides a stable platform for on-orbit operations. The structure of a CubeSat is to a certain degree fixed by the standard and the available launch pods. For a 1 U satellite the volume is $10 \times 10 \times 10$ cm, typically increasing across one of the dimensions for larger satellites. For example Genesat-1 [27] is 6 U with dimensions of $60 \times 10 \times 10$ cm, however other dimensions exist such as 2×3 U. The structure must be strong enough to survive the forces experienced during launch and deployment from the launch vehicle, while still being as light as possible to minimise costs. In addition the structure needs to retain its structural integrity in the harsh environment of space for the duration of the mission and serious consideration is put into material selection as not all materials can be used in vacuums or are suitable for use within the deployer. Fig. 2.5 shows some off the shelf structures available to purchase from Pumpkin and Clyde Space [32, 33].

Mounted on the outside of the structure are the solar panels used to generate energy from the Sun. To meet the increasing power requirements of complex satellites, more and more solar cells are needed. The problem is that there are strict requirements and only limited space-availability within the Poly PicoSatellite Orbital Deployer (P-POD). To overcome this, deployable solar panels are used, which open up once the CubeSat is launched from the P-POD. The mechanisms involved are often simple springs and latches; usually a burner circuit contains the mechanism until the satellite has been launched and it is ready to be expanded. The combination of the space environment and the mission critical aspect of such mechanisms means that their design is often simple but over-specified. In a similar vein, the communication antennas used on typical CubeSat RF frequencies; $\simeq$437 MHz; are not practical for launch because they would take up too much room. Instead they are stowed away and released using similar mechanisms to the solar panels. Again this is a mission critical aspect as failure to deploy could result in the inability to communicate with the satellite. Examples of deployable solar panel designs and antenna mechanisms can be found in [34, 35].

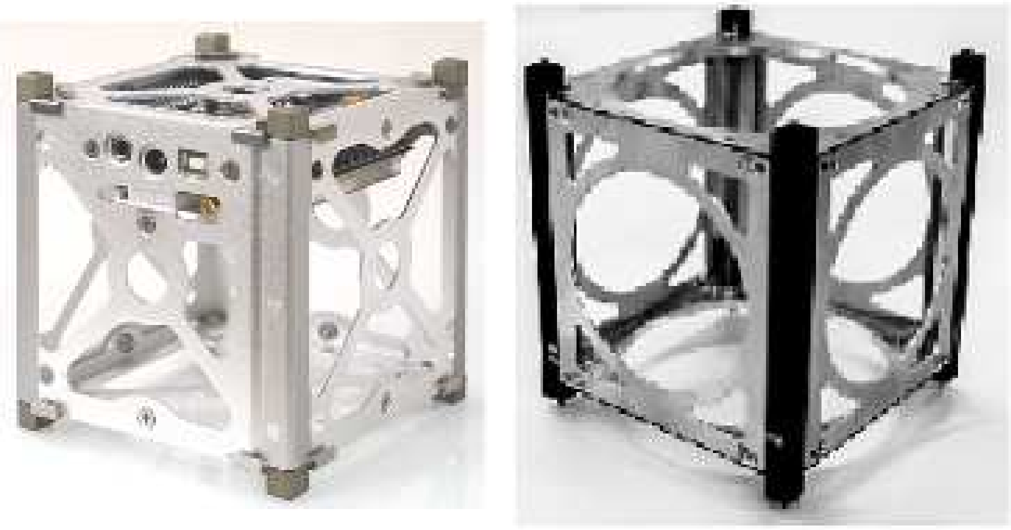

Figure 2.5: Pumpkin (left) and Clyde-Space (right) 1U Structures [32, 33]

2.4 Space-Specific Design Challenges

The design and operation of a spacecraft is tightly coupled to its orbit. The three major orbits are defined by the distance between the Earth and the spacecraft: Low Earth Orbit (LEO) covers the range from 700 - 2000 km, Medium Earth Orbit (MEO) stretches from 2000 km up to Geostationary Earth Orbit (GEO) at 35,786 km. Satellites in GEO orbits have the same rotation period as the Earth and will appear stationary over a location on the the Earth's surface. Satellites in lower or higher orbits than GEO will move in relation to the Earth. Satellites found in LEO and MEO orbits will appear to move across the sky when viewed from Earth. The immediate result of this remoteness from Earth is the loss of predictable atmospheric conditions and the movement of the satellite w.r.t the Earth in the chosen orbit. These aspects play an important role when developing a satellite, providing a number of specific challenges which must be accounted for to produce a reliable system.

The harsh environment of space provides a number of challenges to satellite designers. Of particular interest are the effects of radiation on electronic components and the techniques used to counter them. Furthermore, leaving the protection of Earth's atmosphere places strict requirements on the materials used to construct a satellite. The vacuum of space can cause materials to change physical properties. The temperature of space is no longer regulated by the Earth's atmosphere and a spacecraft is often exposed to huge temperature swings. The materials used to construct a satellite must be light to keep within the weight budget but strong and robust enough to withstand the space environment and the launch of the satellite.

In addition to all this there is the ever present danger of being struck by very fast moving, small pieces of space debris. Sec. 2.4.1 details the challenges when developing for the harsh environment of space.

Operating in space places particular constraints on the communication challenges faced by satellite developers and are affected differently depending on the spacecraft's orbit. The three major orbits are best suited to various applications and come with their own unique communication challenges. GEOs provide a fixed position in the sky and offer a huge footprint, i.e. effective coverage, making it ideal for broadcast services such as satellite television. However, the significant latency involved means they are not ideal for telecommunications. Selecting an orbit closer to the Earth, such as LEO reduces the latency and transmit power, but requires more sophisticated equipment in order to track the fast moving satellites. In addition, bringing the satellites closer to Earth and reducing their footprint; results in the need for multiple satellites in order to provide continuous service. Sec. 2.4.2 details the difficulties of designing a communication system for a satellite.

2.4.1 Environmental Effects

The Earth's atmosphere is made up of five principle layers: troposphere (0-11 km), stratosphere (12-50 km), mesosphere (50-80 km), thermosphere (80-700 km) and exosphere (700-10,000 km). The space environment, or more specifically the point at which the Earth's atmosphere begins to degrade is outside the troposphere. Once outside the relative safety of the troposphere, the atmospheric pressure rapidly begins to fall — at the top of the stratosphere the pressure is a thousandth compared to sea-level. This loss of pressure can cause materials to change physical properties, changing solids into gases. The phenomenon known as outgassing refers to the vaporisation of surface atoms of a material when it is subjected to an ambient pressure that is comparable with its own vapour pressure [15]. This process occurs at an increasing rate as temperature rises. Outgassing can be detrimental to devices such as camera lenses or solar panels which can get coated in the expelled material, affecting their operation [11, 15].

Many international organisations, e.g. ESA, NASA publish test data and information related to materials for use on spacecraft [36, 37] — they even provide the status of various Printed Circuit Board (PCB) manufacturing lines and Surface-Mount Device (SMD) components. They have gained this knowledge through use on previous missions as well as thorough testing. Although the rates at which different materials outgas for a given temperature can be determined; the exact surface conditions of orbiting vehicles are difficult to determine, this is especially true for LEO, and exact figures for mass loss are therefore not available.

During satellite development a compliance document is created which lists and describes, among other requirements, compliant materials as well as the acceptable tolerance levels especially when dealing with potential problematic ones. Designers use the test data available to them and try to avoid or minimise the use of these materials or components. However, it is sometimes impossible to avoid such materials e.g. when embedded in an electronic component. In this case it is the subsystem designer's responsibility to report this via the risk evaluation mechanism to the mission and spacecraft overseers.

The Earth's atmosphere, specifically the troposphere, has provided a stable environment where life has been able to evolve. The diurnal temperature variation is low and the fixed gravitational force of the Earth provides a familiarity within which to design. Leaving this well understood and stable zone has significant and sometimes unexpected implications. The almost complete loss or absence of any of the effects of gravity, also known as Microgravity, means objects do not fall, bubbles do not rise, particles do not settle and convection currents do not occur [11]. The lack of convection has implications for the safe operation of electronic components, as they must not be allowed to overheat. Spacecraft layout and equipment such as radiators and heat pipes are used to move heat away from sensitive components. The external temperatures at these altitudes range from as low as -85° C to over 125°C. For a satellite in LEO, experiencing up to 9 orbits per day, these fluctuations place huge stresses on the mechanical structure of the spacecraft. The orbital profiles and spacecraft attitude are all taken into account when designing a spacecraft structure.

Aside from material integrity the electronic components must be able to withstand or mitigate the effects of cosmic radiation. Outside the protective layers of the Earth's atmosphere the Sun's photons, solar wind particles and interplanetary magnetic field can adversely affect sensitive space systems. Only for LEO with its lower altitude the Earth still offers some protection from the radiation arriving from space. Particularly for MEO and GEO, the impact of cosmic radiation is often minimised through careful components selection and shielding, however this protection comes at a cost and does not necessarily fall within the CubeSat philosophy of using off the shelf components. This section introduces the challenges of designing for space using COTS components and how they can be made more resilient to these effects through appropriate design techniques.

Traditionally CubeSat missions are designed for and operated in lower LEO, usually up to 1000km. The radiation environment in low-Earth orbit includes elements of cosmic radiation which can when left unchecked cause degradation to satellite electronic components and ultimately performance. The limited lifetime and academic nature of many CubeSat missions means that the effects of cosmic radiation on electronic components is often not considered or accounted for due to associated monetary or time cost. However in order to guarantee data integrity and system performance especially in the context of more advanced missions such as formation flying and networking, these effects must be considered. Presented here is an in depth look into these effects as well as methods used to counter act them using methods still adhering to the CubeSat principle of low-cost.

Radiation can be detrimental to the operation of electronic components through a number of different mechanisms both destructive and non-destructive. These are classified either as single events effects or cumulative long term effects; possible sources of these types of radiation in space include:

- cosmic rays;
- solar particle events;
- Van Allen radiation belts.

A comprehensive review of radiation effects on integrated circuits, mitigation techniques and part selection follows in this section. Radiation effects examined include single event effects and long term effects with a particular focus on the impact on FPGAs. These findings are presented to aid part selection for low-cost satellite systems, with a requirement to use COTS components. Tab 2.2 lists the various radiation effects and provides a brief description. There are a number of well known methods used when trying to mitigate the effects of radiation on electronic components. These include: employing expensive components designed to withstand the extreme environment of space or introducing redundancy to systems thus enabling them to cope with multiple bit errors in some cases.

Conventional radiation hardened or tolerant components, available from many manufacturers and designed to withstand the harsh environment of space, are often prohibitively expensive and come with lengthy procurement times. Both these factors go against the nature of the CubeSat philosophy of low-cost off the shelf solutions. However, as described below, once these types of disturbances are understood there are a number of alternative solutions a designer may use to mitigate the possibility of radiation effects causing any damage.

The level of radiation experienced by a device within the spacecraft depends on the angle/direction of incidence of the radiation, the level of radiation and the amount of material through which the radiation passes before reaching the device [47]. Hence electronics may be shielded from incident radiation through their placement within the spacecraft and/or through the inclusion of shielding materials. Including shielding material adds extra mass to the spacecraft, increasing the launch cost [48]. By placing a device in the centre of the spacecraft it will be more shielded from radiation than if it was placed on the outside surfaces of the spacecraft. However it should be noted that placement of components also has an effect on thermal management [49], hence there may be a trade-off to be made. Shielding is not effective at reducing Single Event Effect (SEE), but it reduces the ionising radiation reaching the device, hence can protect devices with low Total Ionising Dose (TID) [50, 51].

Triple Modular Redundancy (TMR) is the most common method of implementing Single Event Upset (SEU) mitigation in a system. It can be implemented at different granularities; register level, block level or device level; and involves triplication of a design portion and

Table 2.2: Radiation effects

Name	Type	Description
Total Ionising Dose (TID)	Cumulative	TID is a cumulative, long term effect caused when radiation induced charge becomes trapped in the silicon and builds up over time. It can cause a range of parametric and functional failures. TID can cause deterioration of threshold voltages, current draw, propagation delays, transition times and drive strengths.
Single Event Upset (SEU)	Single Event Effects	Single Event Upsets (SEUs) occur when a charged particle strikes a register, latch or other storage element and causes a bit flip (i.e. a 1 to change to a 0 or a 0 to change to a 1) [38]. SEUs may also be caused by the latching of an SET into a storage element [39]. The fault will remain held in the storage element until it is cleared, reset or a new value is clocked in. The severity of this flip varies due to the relative importance of the data set it is part of.
Single Event Transient (SET)	Single Event Effects	Single event transients (SETs) occur when an energised particle strikes a sensitive node in the circuit and causes a pulse or glitch in a signal [39]. These transients can then propagate to different parts of the system where they can cause an error, e.g. if a transient propagates to the data input of a register (or registers) and meets the setup and hold requirements it may then become an SEU [40].
Single Event Functional Interrupt (SEFI)	Single Event Effects	Single event functional interrupts (SEFIs) occur in a similar manner to SEUs however the occurrence of the upset causes the normal operation of the device to be interrupted, i.e. the device stops functioning correctly [41, 42]. Where an SEU could cause an incorrect output or an FSM to enter and incorrect state a SEFI could cause the device to be reset or held in reset, IO banks to be disabled or devices to become stuck in test or low power mode [43, 44].
Single Event Latchup (SEL)	Single Event Effects	Single event latchup is a potentially destructive event [45] which occurs when a high energy particle strikes a sensitive node and creates a parasitic transistor between the power rails, causing a large current to be drawn [46]. If this current is sufficiently large and is left unchecked then the device can be permanently damaged, sometimes referred to as burnout.

adding voting logic to filter out an incorrect result in one of the three signal paths [52, 53, 54]. Duplicate with compare (DWC), in a similar manner to TMR, introduces redundancy to detect errors however as DWC only has two signals to compare, it is impossible to tell which is correct. As a result DWC on its own is only able to detect errors, but it has no error correction capability although it may be combined with other schemes such as reconfiguration or temporal redundancy [55, 56]. While not being able to correct errors DWC offers a reduction in the resources required to implement the scheme compared to TMR. As a result DWC may be suitable for use in systems where there are tight constraints on resources, hardware, mass, cost etc. where timely detection of errors with a system level is sufficient.

Error Detection and Correction (EDAC) codes and Error Correcting Codes (ECC) can be implemented in hardware and software to verify data stored in memory and protect against bit errors due to SEUs. Hamming codes are used to produce a parity check for the stored data; capable of detecting multiple bit errors and of correcting for single bit errors [57, 58].

Watchdog timers help to protect against SEFI and software crashes, resetting sections of the hardware in an attempt to recover normal operation [42]. Varying levels of watchdog can be implemented to minimise the disruption and recovery time from more minor faults or in the cases where the source of a fault cannot be determined [51, 59]. It is important to note that any reset control circuitry should be protected against SEU/SET to avoid spurious resets.

Lock step is another method used to introduce redundancy and thereby check for errors in operation. It works by running two identical systems simultaneously, each performing the exact same operation as the other. In this fashion, everything either works in harmony together to produce a valid result (combination of both systems output) or the output is invalid.

SET filtering can be used to reduce the amplitude and width of transient pulses to prevent them from being latched at the input to registers. As clock frequencies increase and once all registers are hardened, SET filtering becomes more important as a means of reducing errors.

On a larger scale to cosmic radiation, and one that requires a different approach, is the threat of space debris — left over pieces of past satellites orbiting the Earth at high speed and capable of causing considerable damage to any spacecraft. These pieces of space debris are usually travelling at relative speeds of $\simeq 8,000$ ms^{-1} or more with enormous kinetic energy capable of inflicting catastrophic damage. The possibility of a collision with space debris is becoming a real problem for satellites. Besides the presence of micrometeorites, the space around the Earth is becoming cluttered with spent rocket stages, old inactive satellites, lost tools and components, fragments from disintegration of other space structures, erosion, and collisions.

The issue is especially problematic in geostationary orbits (GEO), where the number of available orbital slots is limited with many satellites sharing the same orbital path, often clustered over the primary ground target footprints. As of 2010, the U.S. Strategic Command was tracking about 15,000 pieces of debris larger than 2 inches (5 cm)[11], with a further estimated total of over 600,000 pieces smaller than 0.4 inches (1 cm) of which 300,000 pieces were circulating below an altitude of 125 miles (200 km). These pieces may be small but are capable of causing major damage and avoiding them is the best option.

2.4.2 Communication

All satellite missions must include some communication functionality. This can be in support of satellite operations, transmission of data generated by payloads or even as the primary mission objective. The satellite mission communication architecture consists of elements found in space on the satellite coupled with those on the ground, such as ground stations or user terminals.

The orbit type has a fundamental impact on the design of the communications system for a satellite mission. A number of key factors when designing a satellite communication system are defined by type of orbit selected i.e. the distance to the satellite: the communication path length to the satellite, is the satellite moving w.r.t to the Earth, how much of the Earth is in view by the satellite at any point and whether or not more than one satellite is needed to fulfil the mission requirements.

The following list characterises the communication challenges associated with each orbit:

- LEO - close to Earth, low-latency, fast moving, short viewings, small-footprint
- MEO - medium latency, not as fast as LEO but still moving, medium visibility
- GEO - far away, stationary, large footprint, high latency, high transmit power

Geostationary orbits maintain an approximately fixed location over the Earth. As a result of this the area of Earth covered by the satellite is essentially fixed. Earth coverage refers to the portion of the Earth a satellite instrument or antenna can see. Fig. 2.6 shows the coverage, or field of view, from the three major orbits projected onto the Earth. Since the field of view of a satellite in geostationary orbit is fixed, it always views the same geographical area and can maintain continuous contact with a ground station day or night. Fig. 2.7 shows the footprint of a handful of geostationary satellites and demonstrates almost entire global coverage minus of course the polar regions. While geostationary satellite are ideal for broadcasting, i.e. to a large fixed area, and making repeated observations of a fixed geographical area, they are far enough away from the Earth to make it difficult to: obtain high quality, quantitative observations and communication parameters such as transmitter power and latency start to become and issue.

Typical range for a long distance terrestrial link may be up to 50 km, by increasing the path length to service a satellite in geostationary orbit the immediate effect is the higher transmit

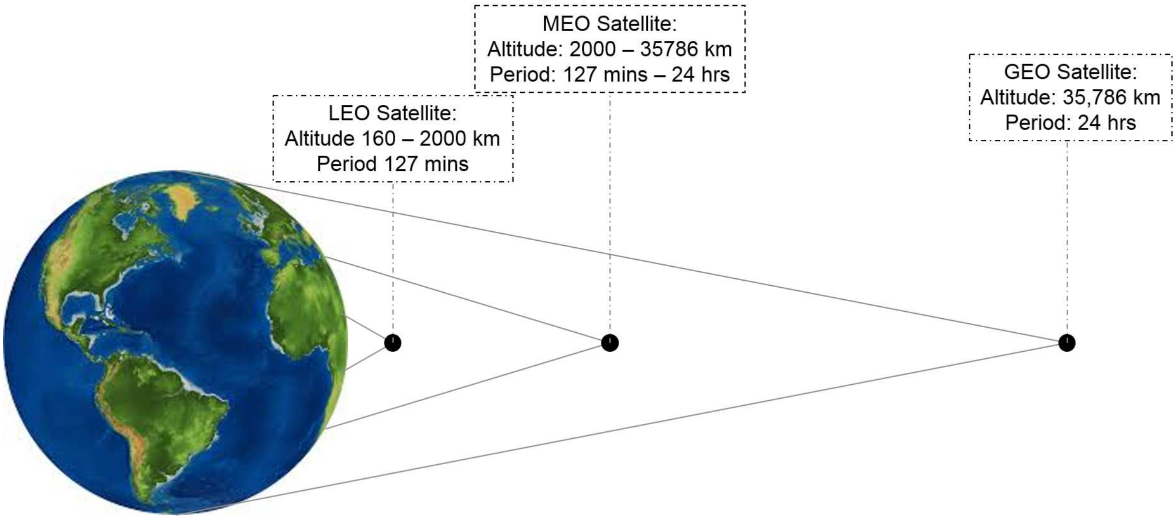

Figure 2.6: Coverage of the Earth by satellites in GEO, MEO and LEO

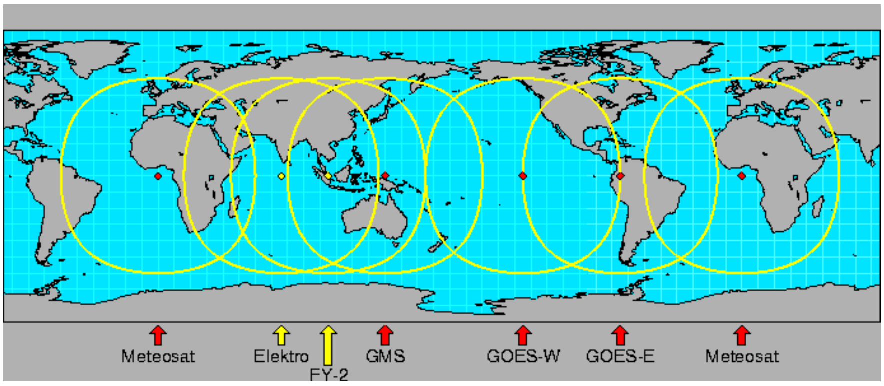

Figure 2.7: Global geostationary satellite coverage, based on a cylindrical equidistant map [60].

power required for successful communication. This is particularly true on downlink where the transmitter power is one of the major demands on the primary satellite power. In addition to the extra power required to overcome the huge distances involved, latency becomes noticeable. Radio waves travel through free space at a velocity of $3 \times 10^8 ms^{-1}$. At this speed the time it takes for a round trip communication to a satellite in GEO is $\sim 0.24\ s$. When other potential communication network delays are included this can easily rise to unacceptable levels. As the speed of light is constant, designers must find other ways to work around these issues, this is usually achieved by modifying protocols or reducing the number of round trips required to the satellite.

In contrast to GEO, the much lower altitudes of low and medium Earth orbits mean latency and transmit power issues are not as severe. A satellite in lower Earth orbits is better positioned to obtain high quality remote-sensing data and is closer to the Earth making it possible for high capacity communication systems to be implemented. For LEO satellites the propagation delays are relatively low, between 4 and 10 milliseconds for a single hop depending

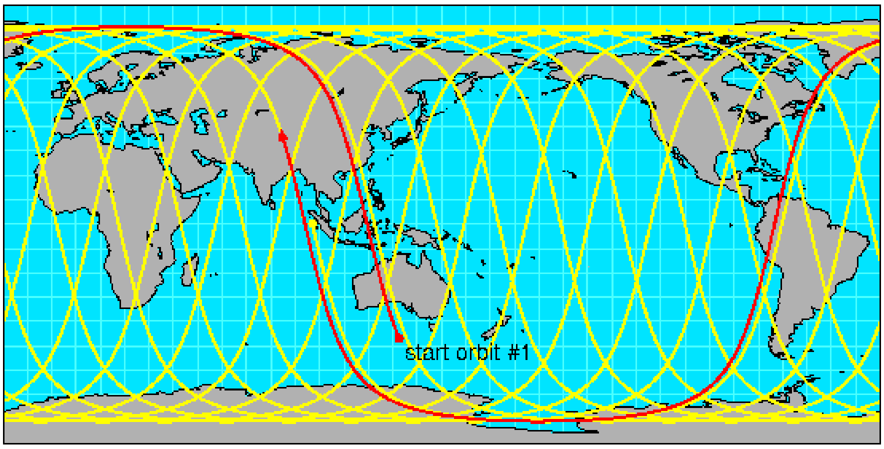

Figure 2.8: Ground track followed by a satellite in Low Earth Orbit [61].

on the position of the satellite relative to the target. However, satellites at these orbits have a much smaller Earth coverage potential, as shown in Fig 2.6, and are no longer considered stationary. With an orbital period of about 127 minutes, these satellites will complete slightly more than 14 orbits in a single day. In comparison to the fixed coverage offered by GEO satellites Fig 2.8 shows the ground track of a LEO satellite over multiple orbits. In fact if a satellite is placed in polar orbit a single satellite can provide global coverage. However this movement makes communication with satellite in these orbits more complicated as they must be tracked in order facilitate communication. In addition designers must account for non-continuous service or deploy multiple satellites in a coordinated manner to provide continuous contact with the satellites for a fixed position on Earth. In a similar way to satellite material and component make up, operating outside of the atmosphere plays a role in the communications system. Radio waves travel more or less unabated through the medium of space, affected only by free space path loss. However travelling through the Earth's atmosphere and weather conditions, radio waves are susceptible to various phenomena that can significantly affect the system performance. The atmospheric impedances can be divided into those that occur in the ionosphere and those in the troposphere.

The ionospheric effects on the radio wave decrease with increasing frequency, $1/f^2$. Above about 10 GHz, the ionosphere is essentially transparent to space communications. However the Ionospheric effects are particularly important for low to medium frequencies. At frequencies below about 30 MHz, the layers of the ionosphere act as reflectors or absorbers, and space communications is not possible [62].

The tropospheric effects can be more significant and are categorised as follows: refraction, attenuation and scintillation. Atmospheric refraction causes a slight shift in the apparent elevation of the satellite. The magnitude of the shift depends on the elevation as well as on the atmospheric pressure and water vapour content. This shift can be determined and accommodated for by using ground station antenna to track the satellite.

Attenuation in the troposphere has two causes: molecular absorption by gases and the effects of precipitation in the form of rain or snow on RF signals. The atmospheric attenuation of radio waves varies significantly with frequency. Its variability has been well characterized by the International Telecommunications Union (ITU) [63] and is shown in Fig. 2.9. At the microwave frequency bands of up to 38 GHz, the attenuation due to the atmosphere at sea level is low at 0.3 dB/km or less. A small peak is seen at 23 GHz, followed by a large peak at 60 GHz, corresponding to absorption by water vapor and oxygen molecules respectively. This effect at 60 GHz in particular, where absorption increases to 15 dB/km, significantly limits radio transmission distance at this frequency. Above 100 GHz, numerous other molecular absorption effects occur, limiting the effectiveness of radio transmissions. A clear atmospheric window can be seen in the spectrum from around 70 GHz to 100 GHz. In this area, low atmospheric attenuation around 0.5 dB/km occurs, close to that of the popular microwave frequencies, and very favourable for radio transmission. Precipitation in the form of rain and wet snow attenuate RF signals through absorption and scattering. This effect is strongest when the water drop sizes are of the order of a wavelength. Thus in the microwave range, for which the wavelength is larger than a raindrop, the attenuation increases

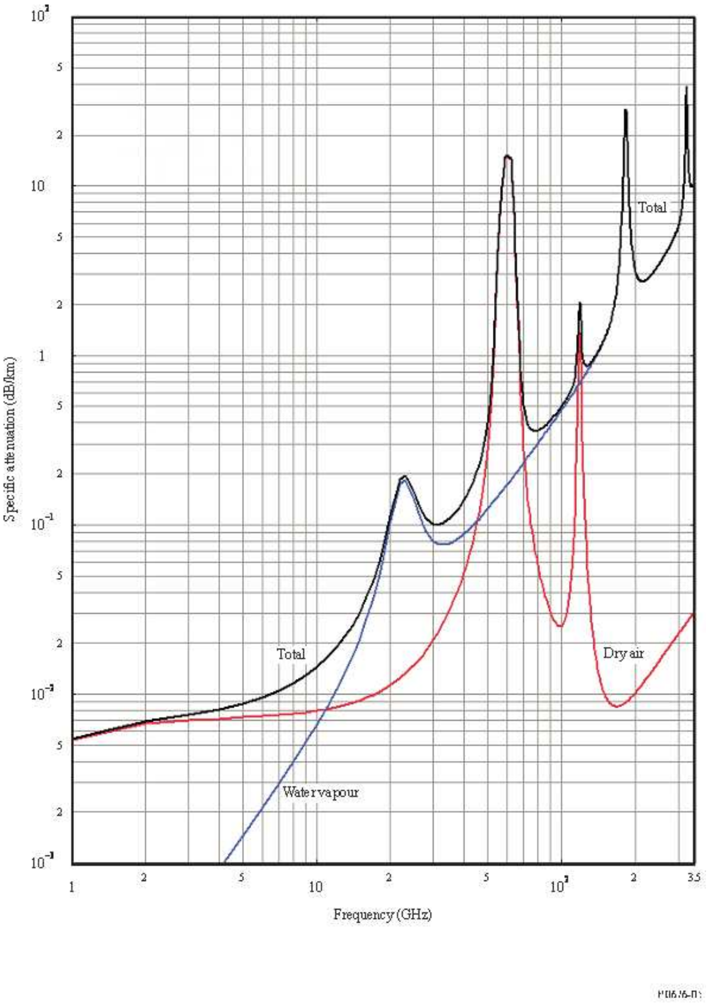

Figure 2.9: Total dry air and water vapour attenuation at zenith from sea level

with frequency. Semi-empirical curves may be obtained showing attenuation as a function of frequency for various rainfall rates assuming reasonable models of drop-size distribution and of rain-cell size. Global rain patterns have been studied and characterized over many years. The ITU and other bodies publish models derived from decades of rain data from around the world [64]. Models are available to predict rain intensities and annual rainfall at those intensities, to enable link designers to engineer radio links to overcome even the worst weather, or to yield acceptable levels of rain outage on longer links. For temperate climates, typical fade margins are in the region of 2 dB at 11 GHz and 3.5 dB at 14.5 GHz, for a link reliability of about 99.99%.

Scintillation refers to the variations in signal amplitude, phase and angle of arrival result from refractive index variations within the troposphere and the ionosphere, and occur over short time frames; typically less than a second. Within the troposphere, refractive index changes are driven by weather and are frequency dependent, and result from localised variations in charged particle densities, which can vary rapidly in the various layers of plasma that comprise the ionosphere. The effects of scintillation are mostly ignored for links operating above 1GHz. However at frequencies lower than 1 GHz variation of several Decibels have been noted. A further note for designers of satellite communication links is that at low elevation angles the effects of scintillation are amplified due to the increase in path length. For this reason many satellite communication links are not operated at elevations of less than $10°$. The importance of scintillation is that, along with clear air attenuation, it causes a slight reduction in capacity.

2.5 Future Applications

CubeSats have matured from their humble beginnings as a test bed for new technology [65, 66] or platform design experience for academic projects [25, 22, 67, 68]. They are increasingly being used to gather Earth observation and environmental monitoring data [69, 25, 70]. The spectrum of developers ranges from high schools to professional engineers and space agencies. The change in attitude towards these small satellites is evident through the CubeSat developments by the US Air Force, NASA [27], Boeing [65] as well as UKSA's UKube-1 [71] and STRaND-1 [72] from SSTL. This in turn has nurtured a growing number of suppliers such as ISIS, Clyde Space and Pumpkin. They have emerged to service the complete spectrum of developers, they supply very capable subsystems, are able to assist in organising launch services and are even geared up to offer complete platform solutions.

The philosophy behind the CubeSat standard is to reduce the cost of accessing space by providing a low cost platform for spacecraft design and development. This has remained the case even though successive generations of CubeSats have offered higher performance levels, helping to lower the risk profile of nano-satellites and make them more appealing to a wider audience. With improvements in technology and a better understanding of nano-satellite behaviour in Low Earth Orbit (LEO), the ability of CubeSats to perform evermore complex functions is increasing. However due their size and limited resources there is a limitation to the range of potential CubeSats applications as they need to fit within the form factor. Despite the potential drawbacks imposed by their form factor, their size and low cost open up new strategies for scientific investigations. Instead of building a large and expensive satellite a number of satellites can be flown together in a constellation. CubeSats can thus significantly reduce a scientific mission's budget and allow scientists to measure multiple data points that would be unobtainable otherwise. In conventional missions, every component must function exactly as designed, but, depending on the mission, a single CubeSat is expendable.

An ambitious project to study the temporal and spatial variations in the lower thermosphere is due to launch in 2017. The project called QB50 [70] has been undertaken by the European Union with the aim to launch 50, 2 U CubeSats simultaneously. They will form a network of satellites, orbiting the Earth in a string of pearl formation. The mission lifetime is as short as 3-months, but will be an impressive demonstration of the potential of employing multiple low-cost satellites together to achieve an ambitious goal. The satellites are built by various organisations across the globe, making this a truly international endeavour.

In a similar vein the HumSat project [69] aims to launch a constellation of satellites to provide communication capabilities to areas without infrastructure — such as disaster areas. The overall objective of the HumSat constellation is to provide messaging services through small user terminals on the basis of a store-and-forward concept. The project is open for international collaboration with organizations from around the world developing nano-satellites. For retrieving data from the HumSat constellation of satellites, the Global Educational Network for Satellite Operations (GENSO) network of ground stations will be one of the core components of the data distribution system. GENSO is a world-wide network of education and radio amateur ground stations linked together via the internet and using standard software developed under an ESA funded project. Through this network, GENSO provides operators of educational spacecrafts with extended satellite access capabilities. The HumSat project is endorsed by the UN Program on Space Applications called BSTI (Basic Space Technology Initiative) which was started in 2009 and the first satellite was successfully launched in 2013.

A major achievement in the progress of CubeSat technology was the launch of the first CubeSat constellation, Flock-1, in the first quarter of 2014. The constellation consists of 28 satellites which were launched on a single launch on an Antares-120 booster. Each satellite in the constellation is capable of providing imaging of 3-5 m resolution. Typical of Cube-

Sat missions, their mission lifetime will be short as they occupy the relatively low orbit of 400 km. On the back of this success Planet Labs, who operate the constellation, have announced they plan to launch 100 further satellite within the year.

Although the HumSat, QB50 and Flock-1 projects revolve around the launch and operation of satellite constellations, they are very much independent spacecraft. By inter-connecting the CubeSats in a network they can share tasks and processing power across many CubeSats, further contradicting some of the negative effects imposed due to form size. The term fractional spacecraft entails splitting up the functional and operational aspects of a large satellite across a network of smaller satellites. The benefits of this approach are: lower development and replacement costs and using a modular form (such as CubeSat) makes expansion to accommodate extra functionality possible. Additionally, spreading sensors spatially and temporally allows a wider range of measurements to be taken, and by spreading the responsibility of one system across a number of smaller satellites, failure of one satellite does not necessarily jeopardise the mission objectives.

2.6 Summary

CubeSats offer a promising and low-cost means to access space. Since their introduction the number of off the shelf components/products available to developers has increased annually. However, the challenges of designing for space must be thoroughly accounted for if the technology required to drive future missions is to be realised. Future missions involving cooperative spacecraft requires a different approach to current CubeSat mentality. Robustness and reliability need to be worked into the design from the beginning. This can be done without foregoing the COTS component and reduced development cycle that has seen some great innovation emerge. Instead a new approach allowing for a reliable high performance embedded computing system utilising clever design methods is needed. In the next chapter such a design, based on a FLASH based Field Programmable Gate Array (FPGA) is introduced. It has the ability to offload processor heavy system aspects to hardware while still maintaining reliability under extreme environment of space, thus enabling more complex on-board autonomy to be achieved.

Chapter 3

Mission Interface Computer

3.1 Introduction

This chapter provides an overview of the current state of the art for CubeSat on-board processing. This is followed up by a more in-depth look at the Steepest Ascent Mission Interface Computer and how it compares to the state of the art. Further details of the MIC provide a comprehensive overview of the design techniques and technology required to offer a new level of processing capability on CubeSat and nano-satellite platforms.

3.2 Motivation

CubeSats are widely regarded amongst the small satellite community as a platform that has the potential to achieve great things in the coming years. The pressure on these tiny spacecraft to perform as well as their larger siblings is increasing and mission developers expect CubeSats to be able to meet very demanding performance levels. This is a change in perspective from previous assessments where CubeSats were seen as having limited functionality, and this optimism comes with increased pressure on CubeSat technology developers to provide this performance whilst still hitting the low cost expectations of the CubeSat form factor. From their humble beginnings as a test bed for new technology [65, 66] or platform design experience for academic projects [25, 22, 67, 68], CubeSats are increasingly being used to gather Earth observation and environmental monitoring data [25, 69, 70]. However, the use of high resolution sensors is severely constrained due to the limited processing capability, downlink bandwidth and power available, resulting in a trade-off between resolution and field of view. Providing a high performance embedded computer for a CubeSat platform which would allow high-resolution data to be pre-processed, thus reducing the downlink bandwidth requirements, would not only help to reduce the requirements placed on the space-to-ground station communication links, but would also allow higher complexity, novel mission goals to be considered [73].

The development of the CubeSat standard was all about ensuring a safe low-cost satellite suitable to be launched along with a primary satellite. The intention was and still is to keep costs to a minimum. The size and weight aspect at first seemed challenging but with clever selection and placement some really advanced satellites were produced. The low-cost philosophy extends beyond the physical metrics of the satellite, components are chosen from standard off the shelf product ranges, not particularly well suited to the harsh environments of space. Another side-effect of the academic origins is the time scale for projects needed to be just long enough to last students doing masters and doctorate projects. This works out to be about 2-years. This rapid development is well suited to the low-tech approach adopted by many missions. They had a constrained budget, limited time and were keen to see the project to the end. One can see that many positive aspects of CubeSats are weighted/contrasted by their negatives.

Steepest Ascent is a Digital Signal Processing (DSP) company with extensive knowledge of digital communications and embedded processing systems. Through their involvement in the space industry Steepest Ascent became aware of the potential of the CubeSat platform: providing a capable low-cost means to access space. However, the limited downlink bandwidth available for CubeSats, as well as the lack of serious on-board processing was a major factor in stopping CubeSats from achieving their full potential. They saw an opportunity in providing a high performance on-board computer, one that would play a significant role in allowing the CubeSat platform to realize its full market potential, and at the same time would provide a platform to showcase Steepest Ascent's design capabilities.

The Steepest Ascent Mission Interface Computer (MIC) in development for UKube-1 [71] represents a significant technological evolution for the CubeSat market; enabling large-satellite processing performance on this small, power-constrained platform. The MIC is still low-cost, but provides a highly-reliable, low-power, yet capable on-board computer. The design has been specifically developed for telemetry and telecommand operations, as well as providing a platform to perform advanced on-board preprocessing of data, allowing for more sophisticated analysis to be carried out and more efficient use of available downlink bandwidths. Other key features of the MIC include a scalable mass data storage capability, allowing data from multiple payload units to be stored centrally. Additionally, there is the ability to reprogram the on-board processing units, allowing in-flight updates of application algorithms to be performed, as well as supporting novel concepts such as re-purposing the entire platform to a new mission.

3.3 Prior Art

With CubeSats becoming so popular in both academic and commercial fields, it is interesting to examine current on-board computer technology. A selection is presented in the following sections.

3.3.1 CubeSat Technology Providers

Pumpkin

Pumpkin Inc. [32] are a well established company, having served the CubeSat community since 2000. Although their expertise lies in a Real Time Operating System (RTOS) they developed called Salvo which is implemented as part of the embedded software of nano-satellite missions, they specialise in providing full satellite kits. Their complete CubeSat design kit, consists of: development and flight models for all subsystems (ADCS/OBC/EPS), a choice of structure/frame as well as a number of software libraries including Salvo RTOS. Pumpkin's continued success has afforded them the opportunity to develop a number of On-Board Computers (OBCs) designed to meet a range of different mission requirements. In order to make such a diverse range of products economical to produce, Pumpkin have coupled a motherboard with a selection of low-power Pluggable Processor Modules (PPMs). The motherboard, shown in Fig. 3.1a,is a low-power interface module providing a PC/104 compliant open architecture suitable for a number of pluggable processor modules. It also features power management to the board, providing protection from over and under voltages as well as a backup battery in case of sudden power failure. Mass storage in the Pumpkin range of on-board computers is facilitated by an MMC/SD card socket. This base board provides a neat way for developers to customise their on-board processing needs.

The PPM is used for operational duties such as communications and Command and Data Handling (CDH). Pumpkin offers a number of PPMs for use with their motherboard. These include a selection utilising the same MSP430 family of Texas Instruments' devices found on the MIC. The A3 module shown in Fig. 3.1b is their most capable MSP430 driven PPM and is further specified below in Tab. 3.1.

GomSpace

GomSpace [74] were founded by the team behind Europe's first CubeSat, called AAU-CubeSat. They operate out of Denmark and have established themselves with reliable technological solutions for the nano-satellite market. They offer a full range of CubeSat subsystems designed and manufactured in house.

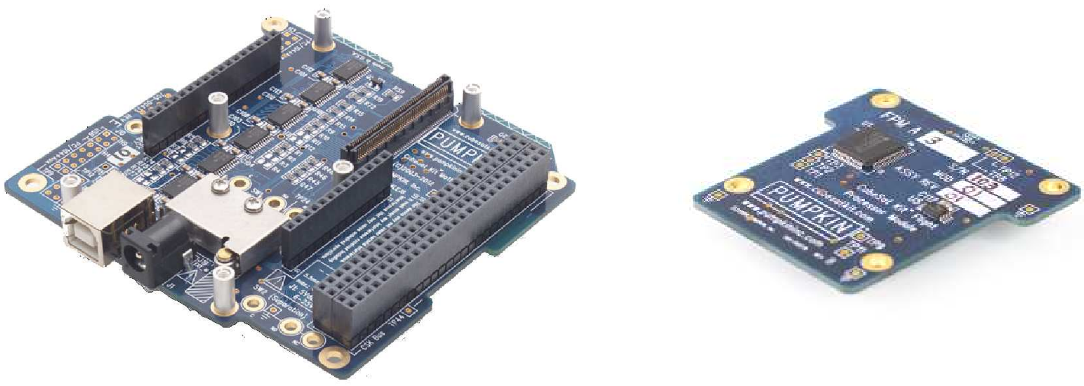

(a) Motherboard.

(b) PPM A3.

Figure 3.1: Pumpkin Motherboard and Pluggable Processor Module A3

Figure 3.2: Nanomind On-Board Computer (OBC) from GomSpace.

Shown in Fig. 3.2 is GomSpace's on-board computer called the NanoMind. It is a standalone board unlike the Pumpkin PPMs and features an ARM7 processor capable of running an open source RTOS called FreeRTOS, making it a very capable system for space applications with limited resources. Additionally the Nanomind features a 3-Axis magnetometer as well as coildrivers which can be used to implement attitude control based on magnetic sensing and actuation.

Andrews Space

Andrews Space is involved in the commercialisation, exploration and development of space. They market themselves as an affordable integrator of aerospace systems and developer of advanced space technologies. Unlike Pumpkin and GomSpace their primary product range and customer base is interested in high-performance and reliability. They see an opportunity

Figure 3.3: Andrews Model 160 On-Board Computer.

to apply their advanced technology to this small form factor satellite market.

Shown in Fig. 3.3 is the Andrews Model 160 flight computer. It occupies the top-range of the market, offering high-performance and reliability but at a substantial increase in cost. It comes in a similar package to the MIC, incorporating an FPGA alongside dual embedded PPC405(400 MHz) processors.

3.3.2 Technology Overview

The following table provides a side-by-side comparison of the afore mentioned companies OBC offerings.

Manufacturer Model	Pumpkin PPM A3	GomSpace NanoMind A712C	Andrews Space Model 160
Processor			
Role Location Manufacturer	Primary Processor TI	Primary Processor Module Atmel	Primary FPGA V4FX Xilinx
Model Bit Width (bits) Clock (MHz)	MSP430F1611 16 16	AT91SAM7A1 32 40	Dual PPC 32 400

UART	2	3	User Defined
SPI	4	2	User Defined
I2C	2	-	User Defined
ADC	1(12 bits 8 Ch)	1(10 bits 8 Ch)	-
DAC	2 (12 bits)	-	-
CAN	-	1	-
RS422	-	-	User Defined
RS485	-	-	User Defined
Ethernet	-	-	User Defined
1553	-	-	-
GPIO	48	49	User Defined
Timers (16-bit)	2	2	User Defined
FLASH (KB)	55	-	-
SRAM (KB)	5	4	64
Storage			
SDRAM (MB)	-	2	64
EEPROM (KB)	-	-	-
PROM (KB)	-	-	-
NOR FLASH (MB)	-	8($4 + 4$ MB)	-
NAND FLASH (GB)	-	-	2
SD Card (GB)	≤ 2	≤ 2	-
Phase Change (MB)	-	-	-
Software			
Operating System	Salvo OS	FreeRTOS	VxWorks/Linux RTOS
Drivers	Yes	Yes	Yes
Power			
Nominal (W)	TBC	TBC	<1
Maximum (W)	TBC	TBC	4
Physical			
Mass (g)	88	55	90
Form Factor	PC104 CSK	PC104 CSK	PC104 Express
Other			

	- - - -	Magnetometer 3 Magnetorquer Drivers 6 Sun Sensor Input 3 Rate Gyro Inputs	2 Parallel digital camera interfaces Supports GPS daughter card Custom IP Cores
Cost			
Hardware EM	£ 1221.00	£ 4018.00	£ 29756.00
Hardware FM	£ 1221.00	£ 4018.00	£ 47046.00
Software EM	£ 3948.00	-	£ 1608.00
Software FM	£ 3948.00	-	-
SD Card Library	£ 539.00	-	-

Table 3.1: Technology overview of state of the art on-board computers from Pumpkin, GomSpace and Andrews Space

3.4 Steepest Ascent Mission Interface Computer

3.4.1 Specification

The Mission Interface Computer (MIC) is a next generation high performance on-board computer sub-system developed by Steepest Ascent. The MIC is capable of delivering large satellite processing capability to the CubeSat platform. It is able to provide significant on-board processing capabilities via the inclusion of an on-board reprogrammable FPGA, as well as large amounts of high-availability on-board storage using banks of redundant solid state memories, while still enabling low-power modes of operation through the use of a secondary low-power processor.

The flexibility afforded to the design because it contains both a Field Programmable Gate Array (FPGA) and a low-power processing unit, means that this high performance embedded computing platform can be configured as an on-board computer including a mass storage subsystem or as a data processing subsystem within a payload. The high speed FPGA fabric can be utilised to implement processor-intensive error detection and correction algorithms, resulting in both a decrease in memory errors and power consumption, as the processing of these algorithms can be carried out using parallel processing architectures directly within hardware and not serially in software.

When configured as an OBC the MIC provides a number of options that allow different system architectures to be accommodated. By implementing the primary processor within the FPGA fabric, the low-power processor can be used as a secondary processor allowing

Figure 3.4: Steepest Ascent Mission Interface Computer.

background tasks to be performed, as well as an in-flight reconfiguration of the FPGA fabric. Under certain fail conditions, the secondary processor can act as a redundant processor allowing main platform operations to continue.

When configured as a data processing and storage subsystem the MIC provides a number of options that allow different system architectures to be accommodated. The FPGA fabric can be used to implement data processing algorithms, allowing data to be pre-processed before being transmitted to the ground. The attached Read Only Memory (ROM), Random Access Memory (RAM) and mass storage can be used to accommodate more complex algorithms that require buffering of data as well as filter weights or lookup table values to be stored.

The delivery of this on-board computer is within a system that has gone through a programme of due-diligence and review, including critical design analysis, processes typical to much larger spacecraft platforms. The subsystem is housed on a single board which is CSK-PC104 compliant. Tab. 3.2 provides an overview of the technology and components which form the MIC and Fig. 3.4 shows an image of the MIC.

3.4.2 Technology Overview

Manufacturer Model	Steepest AscentSA-MIC	
Processor		
Role	Primary	Low-Power
Location	FPGA M1A3PL	Processor
Manufacturer	Microsemi	MSP430F5438A

Model	Cortex-M1	MSP430F5438A
Bit Width (bits)	32	16
Clock (MHz)	20/40	20
UART	User Defined	4
SPI	User Defined	8
I2C	User Defined	4
ADC	-	1(12 bits 14 Ch)
DAC	-	-
CAN	User Defined	-
RS422	User Defined	-
RS485	User Defined	-
Ethernet	User Defined	-
1553	-	-
GPIO	User Defined	87
Timers (16-bit)	User Defined	3
FLASH (KB)	0	256
SRAM (KB)	32	16
Storage		
SDRAM (MB)	8	-
EEPROM (KB)	8	-
PROM (KB)	128	-
NOR FLASH (MB)	8	-
NAND FLASH (GB)	2/4/8/16	-
SD Card (GB)	-	-
Phase Change (MB)	-	
Software		
Operating System	-	-
Drivers	Yes	Drivers
Power		
Nominal (W)	< 0.3	-
Maximum (W)	< 1	-
Physical		
Mass (g)	76	-
Form Factor	PC104CSK	-
Other		

	EDAC SDRAM ECC NAND FLASH Dual Clocks Custom IP Cores	- - - - -
Cost		
Hardware EM	£ 10000.00	-
Hardware FM	£ 15000.00	-
Software EM	-	-
Software FM	-	-
SD Card Library	-	-

Table 3.2: Technology overview of the Mission Interface Computer by Steepest Ascent

The combination of the low-power processor unit and FPGA means the MIC can be configured to suit a wide range of mission performance requirements with no change to the hardware design:

- MSP430 – low-power processor OBC offering a similar level of performance to the Pumpkin systems
- FPGA + Embedded ARM CPU – a more capable OBC with a scalable processing system coupled with the possibility to use the FPGA for processor heavy tasks, similar performance to GomSpace offerings
- MSP430 + FPGA(fabric only, no CPU) – low-power processor OBC with the possibility to offload/implement data processing algorithms to the FPGA fabric and access to mass storage
- MSP430 + FPGA(with CPU) – high-performance dual processor design providing access to mass storage, FPGA fabric and the use of a secondary processor allowing background tasks to be performed, as well as opening up the possibility for an in-flight reconfiguration of the FPGA fabric

3.5 Technical Innovation

The CubeSat platform has proven to be an innovative but challenging platform to provide low-cost access to space. Its potential has recently experienced a change in perspective from previous assessments where CubeSats were seen as having limited functionality. However, the increasing desire to support multiple high resolution payloads with a single satellite motivates the design of a high performance on-board computing subsystem. One that is not only able of carrying out the on-board control and monitoring aspects for the spacecraft, but also to act as a central data handling hub capable of pre-processing and storing data between transmissions to the ground.

The size, mass and power restrictions of a CubeSat as well as the space environment present a significant challenge for implementing such a sub-system. Current CubeSat on-board subsystems are often basic at best, with limited on-board processing and storage capability. Many of the current offerings are result of the output of research projects from institutions such as universities and lack the level of maturity of an industry driven design.

The Mission Interface Computer (MIC) sub-system by Steepest Ascent aims to deliver large satellite processing capability to the CubeSat platform by including a degree of pre-processing capability; allowing greater fields of view to potentially be examined and making more efficient use of the available downlink bandwidth. This in conjunction with the ability to store both post and pre-processed data in a central location allows the complexity of the individual payloads to be reduced significantly and consequently the risks associated with such developments reduced.

The design specifications for the MIC design can be summarised as follows:

- Provide a low-power mode of operation that maintains a level of continuous control.
- Provide a high-speed processing platform that allows the addition of custom processing algorithms.
- Provide support for multiple payloads.
- Provide the capability to reprogram the processing platform in-flight to allow the platform to be updated and/ or re-purposed.
- Provide significant on-board mass storage including a variable degree of redundancy depending on the criticality of the data stored.
- Provide fail-safe modes of operation allowing either on-board processor to fail and maintain a level of continuous control.
- Provide quantifiable levels of reliability and availability.

In order to meet the robust, high-performance specifications described above the development of the MIC followed a stringent design policy matching those of larger satellites. Due diligence was exercised right through from component selection to reliability measures, everything was scrutinised using space industry techniques and standards. This section highlights the details of the hardware design and contributions made to the design.

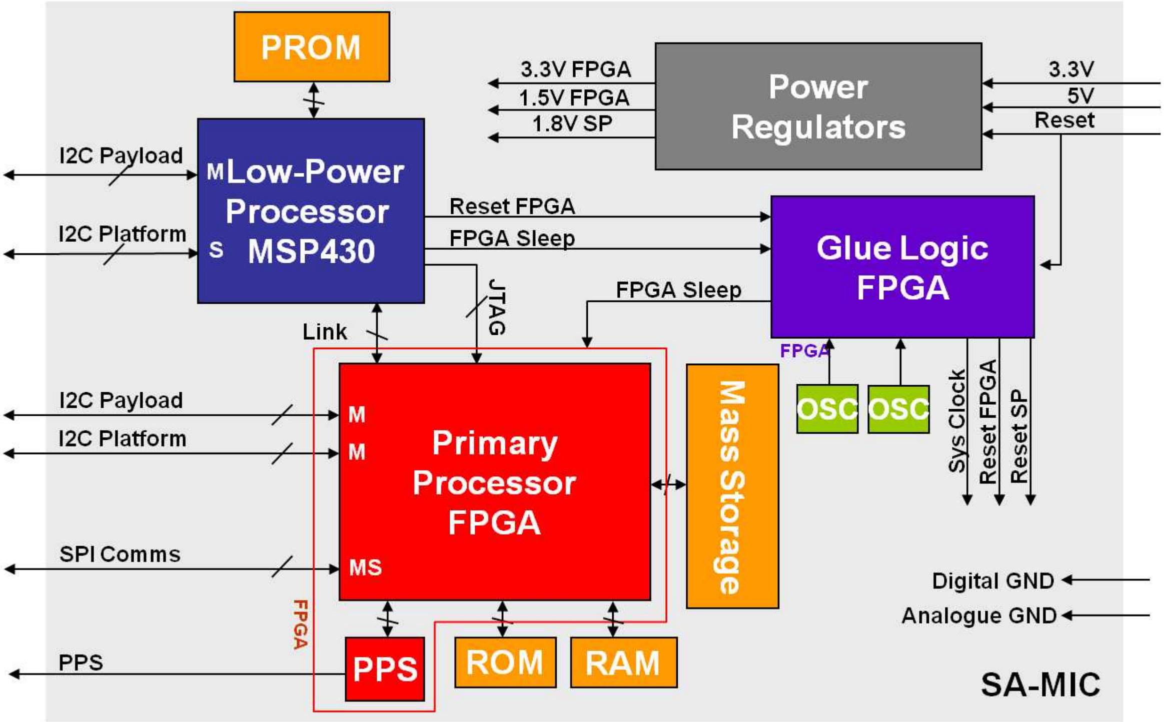

Figure 3.5: Architecture of Steepest Ascent Mission Interface Computer.

3.5.1 Design

The Mission Interface Computer (MIC) is first and foremost a high performance on-board computer. It will act as a common computing interface between the payloads and the CubeSat platform, performing shared scheduling and operation functions. To do this the MIC must possess sufficient computing power for command and data handling as well as managing access to the mass storage and communication subsystems. The MIC is able to treat the payloads and to some extent the rest of the spacecraft platform as black boxes. This is important if the platform is to meet its multi-mission capability goal; therefore the MIC design will define the interface control between platform and payload.

The MIC design needs to be low-power and able to deliver scalable high-performance processing. A system consisting of a primary processor embedded in an FPGA and a secondary safe processor was defined. The key sub-systems of the MIC are shown in Fig. 3.5. The configuration implements an ARM Cortex-M1 soft core processor within the Microsemi ProASIC3L FPGA Fabric. The ARM Coretx-M1 acts as the primary processor while a Texas Instruments MSP430 low-power processor is used as a safe processor, providing low-power modes of operation and a backup capability for the primary processor. Memory is provided by SDRAM, storage comes from dual redundant NAND FLASH. Other key subsystems of the MIC are the power regulation, communications header i.e. the CSK-PC104 connector, glue logic and system health monitoring. The architecture of the design needs to be flexible enough to implement: a distributed payload architecture where the MIC will act as a pay-

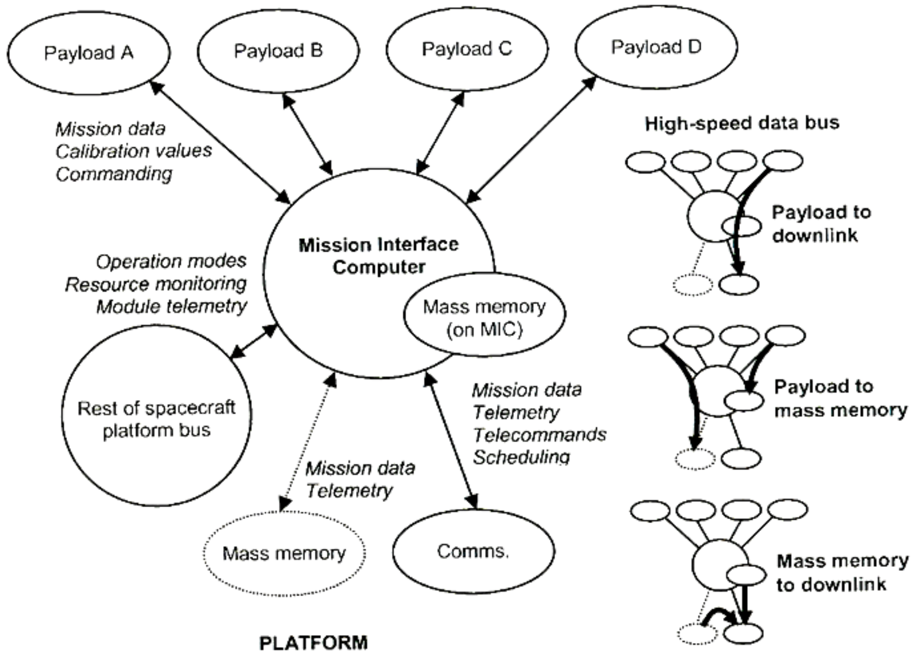

Figure 3.6: Key systems interfaced to or through the Mission Interface Computer (MIC).

load manager, switching between payloads and allocating data to mass storage, or, a highly integrated architecture where the MIC might be expected to perform a substantial part of the mission processing, such as data compression or analysis. The outline for these payload interface concepts is given in Fig. 3.6. The MIC moderates the links through the high-speed platform data bus; for example from payload via/through the MIC to downlink, from payload to mass memory via/through the MIC or from mass memory to downlink.

A core function of the MIC is to store data from the payload in mass memory and then pass the data for downlink to the communications module. Memory shall, in the first instance, be implemented as FLASH memory within the MIC; however further mass memory is available and access to this memory will need to be managed by the MIC. It is assumed payloads will carry sufficient cache memory for high density data operations (they may also carry dedicated memory). The MIC may need to prioritise payload data as the data rate to ground is likely to be the bottle neck for the platform. For the highly integrated architecture raw data from a payload may be passed directly to the MIC for processing. This processing could involve data compression, allowing more efficient use of on-board mass storage. Furthermore data could be analysed on-board and only the results stored or transmitted; once again reducing the storage and transmission requirements. Low-power signal processing techniques can be used to minimise power consumption.

The MIC shall be fault tolerant and as far as possible resilient to SEU. The computer shall consider multiple cores within a single FPGA, this will allow radiation mitigation techniques to be applied to the processing unit; these methods include: TMR or setting the processing unit in a dual command monitor type configuration (lock step). This is a similar concern for memory storage; again TMR could be considered as a solution. To minimise the probability of Single Event Transient (SET) (which occur as a function of operating frequency) the maximum clock speed should be minimised. Ideally, the clock speed should be driven by the maximum data processing requirement. Radiation mitigation techniques and component suitability were investigated and discussed in further detail in Sec. 2.4.

Due to the low-cost nature of the CubeSat platform an additional technical innovation has been the use of Commercial Off The Shelf (COTS) components. Although not unique within the CubeSat market place, the evolution in capability that has been delivered with the MIC requires an enhanced process of COTS component selection. The components used to make up the MIC have been selected specifically to fulfil the CubeSat design philosophy of low-power and cost while still offering a better level of performance over current on board computers. The central component in the MIC is the ACTEL ARM Cortex-M1 enabled ProASIC3L FPGA (M1A3P1000L) device. Using a reconfigurable FPGA with a soft core processor as the on board processing unit allows for a range of designs to be implemented, including those utilising the full capabilities of the high performance FPGA without the soft processor core. One of the primary reasons for selecting this device is because it is fabricated from FLASH rather than Static Random Access Memory (SRAM). Due to their semiconductor arrangement FLASH-based devices are much more resilient to the effects of cosmic radiation; these are termed SEE and can arise from a number of sources. These effects can be mitigated through design but this costs logic and adds complexity, thus a hardware based solution to this possibility was deemed to be superior. Another benefit of FLASH-based FPGAs is their low-cost operation when compared to SRAM devices. The FLASH-based FPGA's have a reduced system footprint and their power consumption is lower since an external configuration memory is not needed. Another benefit of FLASH-based devices is start-up time — as they do not need to be configured they are live at power-up unlike the SRAM devices which lose their configuration each time they are powered down.

At present the ProASIC3L are only available equipped with an ARM Cortex-M1 soft processor. The Cortex-M1 is a 32-bit processor able to operate at up to 60 MHz and the soft IP core nature of this device means it can be customised to suit the level of performance as well as the number and types of peripherals required. Although current configurations allowed for this device do not include use of a Real Time Operating System, Steepest Ascent have developed many RTOS free embedded systems capable of offering a more predictable and resource efficient design and feel that this is not a negating factor.

In the event the primary processor failed to function correctly the entire mission success could be jeopardized. To account for this and mitigate its effect a safe low-power processor was introduced on the MIC. This safe processor is designed to act as a low-power safe mode processor, capable of monitoring the operation of the main FPGA and system functionality. It has the power to take control of the system in low-power sub-nominal operations not using the primary processor or the FPGA, essentially managing the satellite with minimal memory and performance benefits enabled. In addition the low-power processor is able to re-purpose the main FPGA — this is novel concept as having the ability to re-purpose the main FPGA could allow for a new mission objective to be achieved. Reviewing current CubeSat on-board computers a popular and reasonable device to use is the Texas Instrument's MSP430 family of devices. The decision to use this device was based on its current use within the CubeSat community and its potential to offer a reasonable level of performance.

The FPGA is connected to the main communication buses, primary control lines, the glue logic interface as well as a number of memory devices, as is shown in Fig. 3.5. The various attached memory devices include:

- PROM: Used to contain the primary processor bootloader [able to load and run software images stored within the NAND FLASH devices] and a redundant copy of the primary system software. The component has been rated by the Radiation Effects Data Workshop (http://www.nsrec.com/redw/) indicating its suitability for use in space.
- NAND FLASH: dual redundant 1 GB mass storage devices used to store secondary system software images, platform and payload telemetry and data from the various payload subsystems. Under normal operation only a single device will be active. The redundant device will only be used if the primary device is deemed to be in fault. The use of ECC and intermittent scrubbing will ensure the integrity of the data stored on the device.
- SDRAM: provides main software instruction, data and buffering storage and access. This memory is Error Detection and Correction (EDAC) protected using a 7-bit parity sequence to allow for 1-bit detection and correction or 2-bit+ error detection on a 32-bit word length. These errors are monitored by the flight software, which will produce an exception handle in case of non-correctable errors or simple count of corrected errors. The design of this is covered in the contributions section to follow.

The glue logic interface device provides failsafe signal conditioning for all internal control signals and implements the clock failure mitigation capability, it must therefore possess strong radiation tolerance. Antifuse FPGAs are One Time Programmable (OTP) devices; once the devices have been programmed, physical metal connections are made on the chip and the design is fixed. The FPGAs are programmed on the ground before being soldered to the board; at this point their functionality is fixed. As a result Antifuse FPGAs do not offer on-orbit reconfiguration as is possible with SRAM or FLASH based FPGAs, however this also means that the configuration of the design is immune to the effects of radiation (SEUs in the registers, SET, SEL and TID still apply). Using Antifuse FPGAs eliminates many of the high costs associated with ASICs however does not provide the flexibility for in flight modification provided by reconfigurable FPGAs. OTP devices are live at power up and do not require any additional circuitry or memory to program the device. Typically, Antifuse FPGAs have a relatively low gate count and simple architecture; their properties make them ideal for applications such as glue logic functions and microprocessor interfaces. The RTAX and RTSX FPGAs from Actel/Microsemi are rad-hard Antifuse devices and like their FLASH FPGAs these are inherently radiation tolerant to configuration errors.

3.5.2 Contribution

The development of the MIC involved a number of Steepest Ascent engineers, each working on key areas. The author was tasked with implementing and maintaining the Actel FPGA i.e. the System-on-Chip and the various design aspects associated with it. In addition I took responsibility for the glue logic, which is in place to monitor and verify the critical signalling between the FPGA/Primary Processor and the secondary low-power, safe processor. This section provides an overview of these contributions to the MIC.

FPGA System-on-Chip

The FPGA fabric contains the primary processor which in normal operating conditions will supply the primary command and data handling capability to the spacecraft. The primary processor is implemented as a soft embedded processor system within the FPGA fabric and is shown in Fig. 3.7. The internal bus system consists of two main buses. Peripherals requiring larger bandwidths and faster rates of data transfer are connected to the Advanced Microcontroller Bus Architecture (AMBA) Advanced High-performance Bus (AHB); these include the on-chip memory and memory controllers. A second, lower bandwidth bus is also present, this is the AMBA Advanced Peripheral Bus (APB) and provides access to other peripherals such as the communication cores and timers. Using an FPGA combined with soft IP cores allows customisation of the processor system, thus features may be added or removed at later stages with minimal impact on the actual physical design.

Due to the nature of the operating environment and the various bespoke modes of operation desired a number of key cores were developed by Steepest Ascent. These included the interface to the Synchronous Dynamic Random Access Memory (SDRAM) and associated error detection and correction functionality, as well as the interface to the external NAND FLASH, Programmable Read Only Memory (PROM) storage devices and the self synchronising Pulse-Per-Second feature.

SA_SDRAM_EDAC

The main on-board runtime memory available to the primary processor comes in the form of SDRAM. This type of random access memory is susceptible to single effect upsets, which

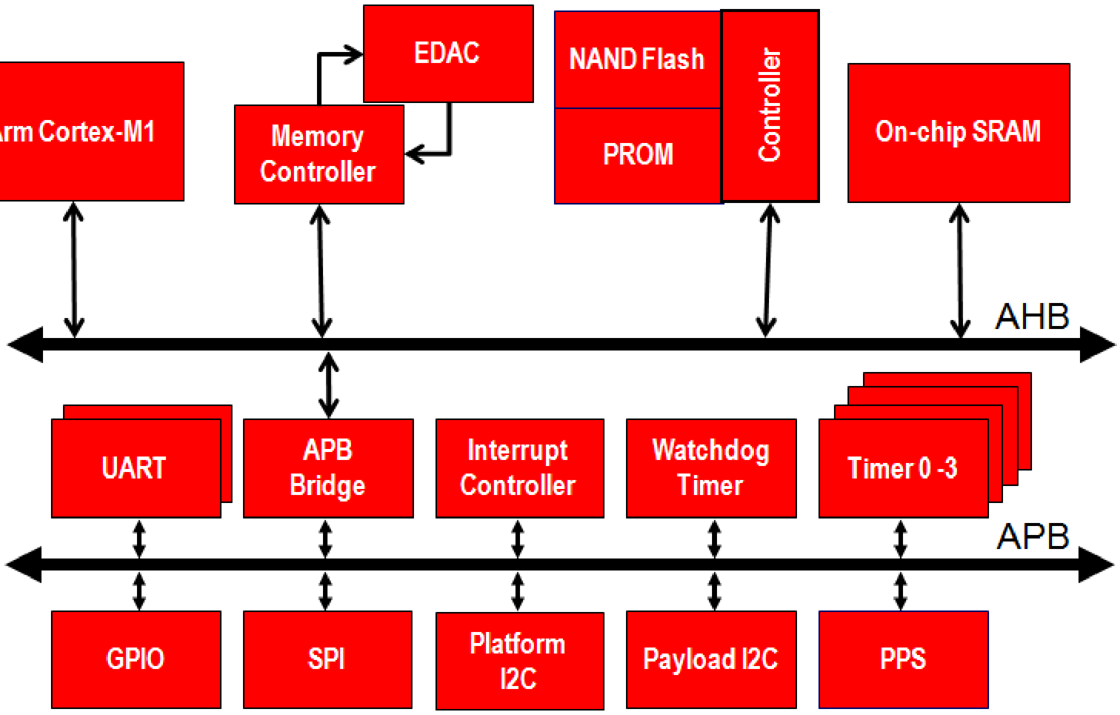

Figure 3.7: Soft core processor system architecture for the Steepest Ascent Mission Interface Computer.

are a result of charged particles striking the silicon of the memory devices. Due to the pivotal role this memory plays within the MIC any errors with the data stored must be detected and dealt with. This is achieved by using an error detecting and correcting code, which adds redundant information to the stored data and is able to use this to detect and correct single bit errors or detect and report two or more bit errors — the location of the affected bits is not returned.

The interface between the memory controller and the primary processor is achieved through a connection on the AMBA AHB bus. SA_SDRAM_EDAC is in essence a combination of two existing Microsemi IP Cores, namely: CoreSDR_AHB and CoreEDAC. The following diagram illustrates the interface between the SA_SDRAM_EDAC Core and the AHB interface.

Operation of the core is as follows:

- READ: Control signals including the address and data are sent over the AHB bus to the SDRAM controller. The SDRAM controller interprets these and engages the necessary control lines to access the required memory locations. As data is read into the core it passes through the EDAC which analyses the data and parity. If no bit errors are detected the data is output. If a single bit error is detected, it is corrected and the data is output as well as the bit error flag is triggered (EDAC_COR). If two or more bit errors are detected, the corrupted data is output from the core and the uncorrected

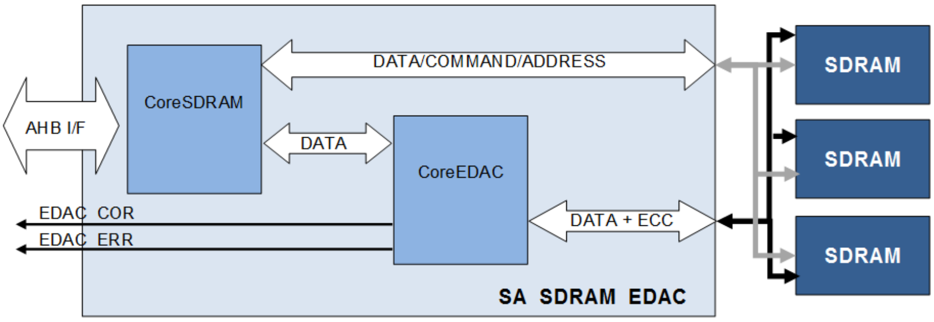

Figure 3.8: Steepest Ascent SDRAM Control with EDAC.

error flag is set (EDAC_ERR). The EDAC is calculated on 32-bits, thus in every type of memory READ access (byte, half-word or word) the full 32-bits are read out of memory, checked and written back into memory, before the data is made available on the bus. The EDAC calculation does not incur any processing losses i.e. zero latency.

- WRITE: Control signals including the address and data are sent over the AHB bus to the SDRAM controller. The SDRAM controller interprets these and engages the necessary control lines to access the required memory locations. The 32-bit memory data plus 7-bits Error Correcting Code (ECC) are first read into the core and checked for any errors; as before up to one bit error can be detected and corrected, after which EDAC_COR is triggered to alert the primary processor to a single bit error; if more than two bits are in error the uncorrected EDAC error flag (EDAC_ERR) is triggered. The next step is to write the new data back into memory. During the exchange between the controller and the memory, the data passes through the EDAC core which calculates the error correction code. The ECC parity bits are appended to at end of the data bit stream as they are output to the memory. The modified READ-CHECK-WRITE process allows access on a byte, half-word or word basis while still providing the possibility to correct for errors using the ECC.

Note:

1. This process is completely transparent to the mission software; apart from counting the single bit errors no further steps need to be taken.
   (a) In the event of a single bit error, the EDAC_COR flag will trigger an interrupt, this can be used to monitor the number of single bit errors corrected.
   (b) In the case of uncorrected data the EDAC_ERR flag will be set, which will trigger an interrupt on the primary processor, the mission software must decide what to do with the corrupted data.

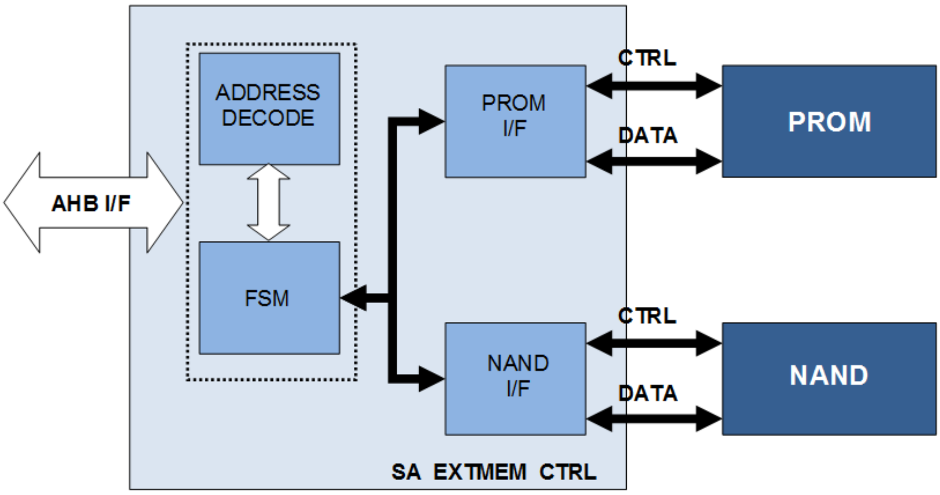

Figure 3.9: Steepest Ascent External Memory Controller.

2. It seems counter intuitive to output the corrupt data, until one realises that the ECC applies to the full 32-bits of data. If the access to memory is only a byte or half-word then depending on the error it is still possible that this data is not corrupted. Due to this possibility the decision of what to do with the corrupted data is up to the mission software.

SA_EXTMEM_CTRL

Steepest Ascent has developed a memory controller core that is able to interface to both the mass storage and program memory device for the FPGA. The interface between this core and the primary processor is handled by an AHB interface. Fig.3.9 shows the connection between the core and the memory devices.

Although the controller interfaces to two separate devices it appears as a single AHB bus slave to the bus master i.e. the primary processor. The address space afforded to the slave is divided with the following offsets:

- PROM — 0x00000000 to 0x0001FFFF
- NAND — 0x00020000 to 0x0002000F

The fashion in which the memory map appears to the primary processor, provides an insight into its operation. The memory address is decoded and identifies exactly which device the current transfer is for.

The memory locations within the PROM are viewed by the primary processor as a reserved block of addresses; writing to an address translates to a physical memory location. Access to the NAND Flash is facilitated through a set of registers; these control the necessary command

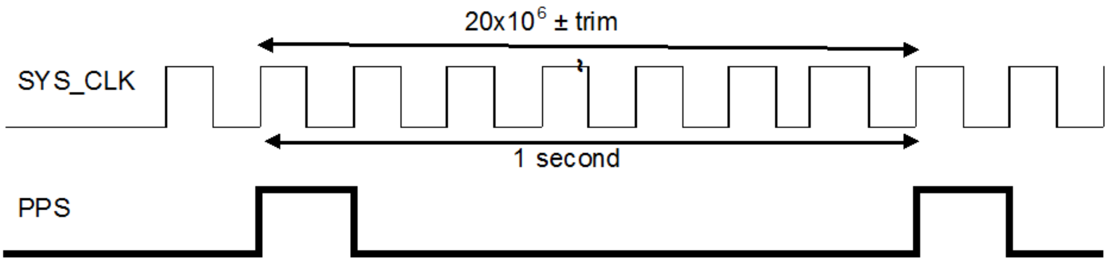

Figure 3.10: Steepest Ascent Pulse Per Second Timing Diagram.

signals, memory transaction type and data to be written. These registers are controlled by the primary processor through the mission control software.

SA_PPS_GPSSYNC

The Pulse Per Second (PPS) core provides a 1 Hz synchronization pulse for the various subsystems with the additional capability to adjust for clock drift using an on-board GPS PPS if available or a value uploaded from the ground station. Fig 3.10 illustrates the underlying operating principle and the various modes are described further below.

In its most basic operation mode the PPS will use the 20 MHz system clock to create a pulse every 20×10^6 clock pulses. Mission time is advanced using the generated pulse per second and stored in the PROM so it can be used when the MIC is coming out of sleep mode. Additionally, the core can use the 1 Hz pulse generated by an on-board GPS to determine an offset and use this to adjust for oscillator drift. Alternatively, this offset can be provided through telecommand from the ground station. The offset is stored and used to provide more accurate mission event timing.

To ensure accurate timing and to account for drift of the on board oscillator which is used to generate the system clock, it is possible to trim the number of system clock cycles used to generate the pulse per second (MIC_PPS). The trim is determined from one of two methods:

- Using an on board GPS_PPS
- Using information uploaded from the ground station

Monitoring the pulse per second generated by an on board GPS module (GPS_PPS) it is possible to trim the MIC PPS thus providing an accurate 1 Hz pulse. The SA_PPS _GPSSYNC core will register when the GPS_PPS is active and use it to determine how many clock pulses occur between pulses. Using this information the SA_PPS_GPSSYNC core is able to determine the necessary amount needed to trim its pulse per second count register. Once the trim has been determined the primary processor is notified and is able to action when to implement the trim.

Note: The edge of the PPS signal generated by the SA_PPS_GPSSYNC will not be aligned to the GPS_PPS signal; the GPS_PPS signal will only be used to trim the MIC PPS.

In the event the GPS_PPS is not available, the ground station is able to upload an estimate for the trim used to adjust the on board PPS generation. This method is not as accurate or immediate as the GPS method and acts as more of a fallback; it is not able to provide what is essentially a real time adjustment of the pulse per second.

Glue Logic

The glue logic device provides fail safe critical signal conditioning for all internal control signals and a clock failure mitigation capability. The glue logic interface interprets the various control signals generated by the primary and safe processor. This includes operations such as reset and entering and exiting low-power modes. All critical control signals are paired and consist of an ARM line and a SIGNAL line. Only the correct combination of the two will result in the desired control signal being accepted; see Tab. 3.3. In addition to this safeguard, all registers in the design have been implemented using triple modular redundancy. This design has been implemented to prevent latch-up events from causing undesired behaviour.

The operation of the logic FPGA and its functions are exemplified by a number of states — covered in the following discussion — which facilitate the activation, deactivation and reset of the two on-board processors as well as controlling entry in and out of low-power modes. A state flow diagram illustrating the operational aspects of the glue logic including permissible/required signals for transitions between states, can be found in Fig. 3.11.

Power on/Power on reset

A power on reset is activated when the POWER_ON_RST_N is held LOW for a short period before being released. Once released the enables for the communication lines (UART, SPI I2C_PLAT and I2C_PAY) are set to their default values:

- UART_SEL primary processor is selected
- SPI is enabled
- I2C_PLAT: primary processor is enabled, safe processor disabled
- I2C_PAY: primary processor is enabled, safe processor disabled

MSP430_RST_N, FPGA_RST_N, POWER_FPGACORE_SW_EN, POWER FPGAIO SW EN are all LOW, while FPGA_FF_N and FPGA_LP_N are both HIGH. On the next rising edge of the clock MSP430_RST_N is released allowing the safe processor to start up and begin its self check. After POWER_FPGACORE_DELAY power to the FPGA core is enabled. After POWER_FPGAIO_DELAY power to the FPGA IOs is enabled. Finally after X_CLK_CYCLES_DELAY the FPGA_RST_N is released and the MIC-FPGA/primary

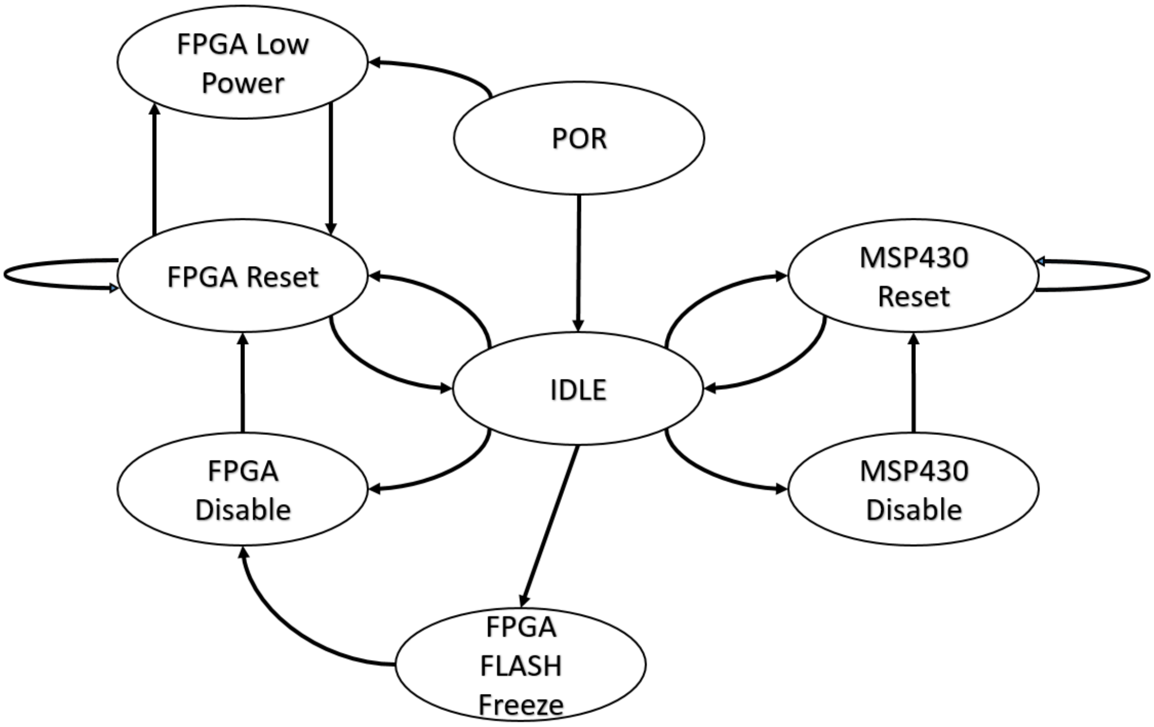

Figure 3.11: Glue logic state flow diagram

Input		Output
_ARM	_SIG	
0	0	Error
0	1	Deactivated State
1	0	Activated State
1	1	Error

Table 3.3: Critical signal ARM and SIGNAL truth table

processor is allowed to start up. This start-up process is exemplified in the Fig. 3.12

Disable

It is possible for the safe processor to disable the primary processor, thus taking control of the communication lines and stopping the LOGIC FPGA from reacting to commands sent by the primary processor. For this to happen the safe processor must be deemed to be operating correctly and must be actively driving the disable lines for the primary processor and the primary processor should not be actively trying to disable the safe processor. Similarly the primary processor is able to disable the safe processor, when this happens the control signals from the safe processor to the LOGIC FPGA are ignored and the primary processor retains control of the communication lines. For this to happen the primary processor must operate correctly and must be actively driving the disable lines for the safe processor. The safe processor should not be actively trying to disable the primary processor in this scenario.

Reset

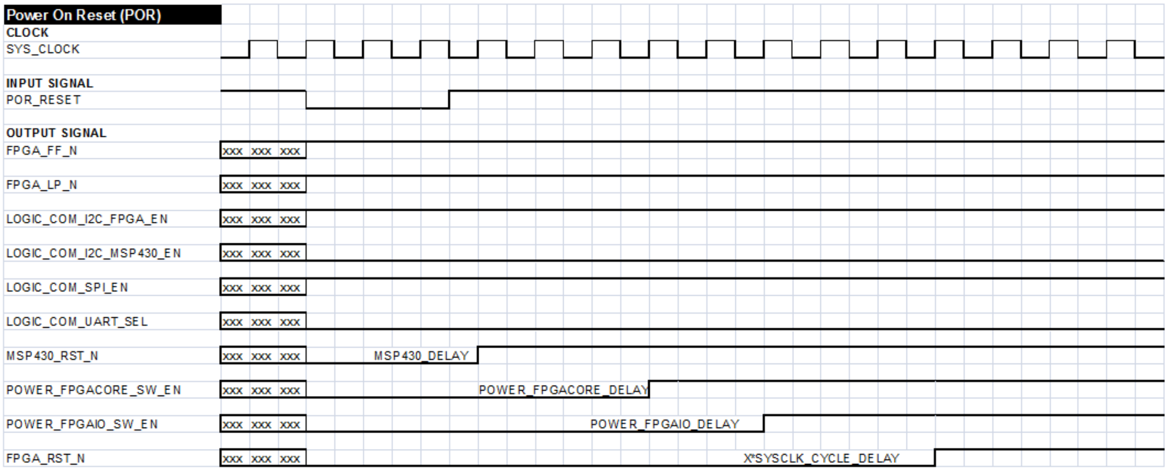

Figure 3.12: Power on reset timing diagram

Depending on the operating conditions, each processor is able to reset themselves, each other or initiate an entire MIC board reset.

Safe Processor

If the safe processor is operating correctly it is able to issue a self-reset command signal to the LOGIC FPGA which pulses the MSP430_RST_N line, restarting the safe processor. The primary processor is unaffected by this. If the safe processor is not disabled and the MSP430_WATCHDOG triggers a full MIC board power on reset is initiated as described above. If the safe processor is disabled by the primary processor and the MSP430 _WATCHDOG triggers the LOGIC FPGA pulses the MSP430_RST_N line, which restarts the safe processor. The primary processor is unaffected by this. If the primary processor is operating correctly, it can hold the safe processor in a reset state by driving the appropriate command signals.

Primary processor

If the primary processor is operating correctly then it can send a command to the LOGIC FPGA to reset itself. The safe processor is unaffected by this. If the primary processor is not disabled and the ARM_WATCHDOG triggers, then a full MIC board power on reset is initiated, this results in the FPGA_RST_N line being held low for a set delay as defined above in the Power_On_Reset section. If the primary processor is disabled and the ARM_WATCHDOG triggers then the LOGIC FPGA pulses the FPGA_RST_N line, this restarts the primary processor. The safe processor is unaffected. If the safe processor is operating correctly, it can hold the MIC-FPGA/primary processor in a reset state by driving the appropriate command signals.

Low Power

Assuming the safe processor is operating correctly it is possible for it to initiate a low-power mode of the primary processor by actively driving the command signals to the LOGIC FPGA for low-power mode enable. During low-power mode the safe processor holds the primary processor in a reset state, then disables power to the IOs and then disables power to the core. To come out of low-power mode the process is reversed: first the MIC-FPGA core is powered up, this is followed by powering up the IOs and finally the reset state is released and the primary processor is allowed to start up again.

In order to compensate for a potential failure of a clock source the MIC board has been equipped with two 20 MHz clock sources (nominal and redundant). A circuit implemented in the glue logic FPGA selects which of the clocks should be used to drive the rest of the board. The clock failure mitigation circuit is proprietary Steepest Ascent IP and provides automatic clock switch over under clock fail conditions. The circuit can be thought of as two competing counter devices, each individually clocked by a single clock source. Under normal operation the primary clock is always output. If either the primary or redundant clock fails, the remaining operational clock causes its counter to time-out, indicating that it is the source to be selected to be output within the system.

3.6 Solving the DSP problem for CubeSats

CubeSats are increasingly being used to gather Earth observation and environmental monitoring data. However, the use of high resolution sensors is severely constrained due to the limited downlink bandwidth available, resulting in a trade-off between resolution and field of view. Providing the ability, through digital signal processing techniques, to pre-process or analyse data could ease the requirements of the on-board computer. Additionally, minimising the amount of data to transfer reduces the bandwidth or time needed to transmit, easing the requirements placed on the communication subsystem. However, these techniques are often complex to implement and processor heavy resulting in higher power consumption and resource utilisation. Offloading the complexity and processing requirements to an FPGA would not only free the OBC for housekeeping duties but also allows flexibility during the design of the system as it can be configured to accommodate mission specific features without major hardware redesigns.

The freedom to trade power, throughput and resources against one another on a CubeSat can be facilitated through the use of FPGAs. The benefits when incorporating an FPGA are demonstrated here by the Mission Interface Computer, which implements a combination of microprocessor and FPGA with error correcting mass storage and memory. The potential of this design structure and how it can be used to implement a high performance embedded computer capable of offering a wide range of signal processing benefits to future missions is discussed here. The final section of this chapter demonstrates how algorithm selection can be used to alter the balance of the relationship between power, throughput and resource utilisation when implementing Digital Signal Processing (DSP) on FPGAs.

The MIC has been designed as a flexible High Performance Embedded Computing (HPEC) platform that can be configured as an On-Board Computer (OBC) or as a data processing and storage subsystem. The architecture therefore supports the addition of custom processing algorithms that make use of the flexible FPGA fabric. Thus, the feasibility of an innovative HPEC sub-system that goes beyond the capabilities of the MIC, but still uses the same design to offer dedicated data processing, can be considered and used as a base to evaluate efficient use of DSP for FPGAs on CubeSats.

The four key challenges to consider when addressing signal processing on-board a CubeSat are data: capture, process, store and transfer. The Mission Interface Computer provides a solution to the first three, while adhering to the CubeSat mantra of low-cost and commercial-off-the-shelf components. Alongside these four challenges are the usual CubeSat limits of size, mass, low-power and the space environment; further elevating the difficulty of implementing a high performance embedded computing subsystem capable of advanced signal processing.

In parallel with the investigation into commercial-off-the-shelf components a review of low-power and efficient signal processing techniques that can be used within the FPGA based system was conducted. As an example signal processing technique applicable to a potential CubeSat mission the classical Fast Fourier Transform (FFT) introduces DSP for FPGAs and demonstrates the integral role algorithm selection plays on the various trade-offs that can be achieved. The FFT in this example could be used in a spectrum analysis mission based on the MIC, sweeping a wide band of frequencies, detecting and reporting which bands are being utilised.

Implementing high performance DSP on the HPEC, the design will need to use intelligent DSP design techniques such as those detailed below in order to minimise power consumption while maintaining the necessary performance. The following are a couple of example implementations of the FFT for signal processing:

- Pipelined ("Streaming") FFT — offers continuous data processing at the expense of a high resource cost.
- Fully Serial ("Burst") FFT — has a lower resource usage than the Streaming I/O implementation at the cost of longer transform time as it loads/unloads data separately from calculating the transform.

On the HPEC, the implemented algorithms will have specific performance requirements sitting alongside very stringent power limits. To illustrate how intelligent DSP implementations can be used to trade-off power, resource usage and performance on an FPGA, the FFT algorithm is implemented on a Xilinx Spartan-6 FPGA — this development board was chosen due to knowledge of the device and development environment. Two methods commonly used to tailor these algorithms for particular needs were investigated and implemented on the Xilinx Spartan-6 development board. These were compared on a power consumption and throughput comparison and the results are presented in Tabs. 3.4 & 3.5 and discussed below.

The following details the clock speed, logic utilisation and device power consumption for two FFT implementations. In the first analysis, the two implementations are compared at the same clock speeds of 20MHz, 50MHz and 100MHz. In the second analysis, both FFT implementations are compared at the same throughput; that is each implementation is clocked so as to produce FFT outputs at the same rate.

The power results displayed were calculated using Xilinx XPower Analyzer, which gives detailed power analysis of post-place and routed designs. Real-time power consumption measurement was attempted; however, on the development board the power consumption of the peripherals was large enough that it masked the changes in power consumption of the FPGA.

3.6.1 FFT Power Consumption Comparison

The power consumption and resource utilisation results for a 1024 and 2048 point FFT implemented in the different configurations and run at three different clock speeds are given in Tab. 3.4. It can be seen that, as expected, the streaming I/O FFT consumes the most power as it uses the most resources. In the table, the power measurement is split into quiescent power (Q) and dynamic power (D). The Burst I/O FFT hardware itself uses no more resources for a 2048 point FFT than that for a 1024 point FFT. The extra resources seen in the logic utilisation figures are used for the memory blocks required to store the input and output samples for the test design.

3.6.2 FFT Throughput Comparison

In this test, the burst I/O and streaming I/O FFTs are compared at different clock rates calculated to give an estimated equivalent throughput. In the results above, the comparison between the burst I/O and streaming I/O gives an idea of the power consumption for both implementations when they are both run at full speed. However, the actual throughput of each implementation is very different.

In the FFT core datasheet [75], Table 9 gives performance and resource usage parameters for the FFT core on the Spartan-6 FPGA. The latency of the burst I/O FFT is roughly 7000 samples, in which time 7 full FFTs could have been calculated using the streaming I/O FFT. For example, using a 100 MHz clock and with the streaming I/O architecture pipeline fully filled,

Spartan-6 xc6slx45	1024 FFT, 16 bits, Unscaled, Truncation, Bit Reverse	
	Burst I/O	Streaming I/O
Power(W)@20MHz CLK	0.076 (D:0.026; Q:0.049)	0.083 (D:0.033; Q:0.05)
Power(W)@50MHz CLK	0.099 (D:0.051; Q:0.048)	0.115 (D:0.067; Q:0.048)
Power(W)@100MHz CLK	0.141 (D:0.093; Q:0.049)	0.173 (D:0.124; Q:0.049)
Slices (total 6822)	306	1,009
LUT-FF pairs	1,006	3,302
LUTs (total 27288)	848	2,989
FFs	1,160	4,124
DSP48A1s (total 58)	6	22
Spartan-6 xc6slx45	2048 FFT, 16 bits, Unscaled, Truncation, Bit Reverse	
	Burst I/O	Streaming I/O
Power(W)@20 MHz CLK	0.071 (D:0.021; Q:0.049)	0.086 (D:0.037; Q:0.05)
Power(W)@50 MHz CLK	0.087 (D:0.039; Q:0.048)	0.123 (D:0.074; Q:0.048)
Power(W)@100 MHz CLK	0.116 (D:0.068; Q:0.048)	0.189 (D:0.139; Q:0.05)
Slices (total 6822)	334	1138
LUT-FF pairs	1041	3877
LUTs (total 27288)	871	3455
FFs	1238	4816
DSP48A1s (total 58)	6	28

Table 3.4: FFT power consumption and resource utilisation by clock speed.

a full FFT (consisting of a new block of 1024 samples) can be calculated every 1024 samples, giving an FFT throughput of $100M/1024 = 98,000$ FFTs per second. The burst I/O FFT runs around 7 times slower, i.e. at around 14,000 FFTs per second.

To compare the two implementations at roughly the same FFT throughput, the burst I/O FFT must be run with a clock rate 7 times that of the streaming I/O FFT. Tab.3.5 shows these results, with the burst I/O FFT running at 100 MHz and the streaming I/O FFT running at 14 MHz.

From the figures the trade-off between power consumption, performance and resource usage can be clearly seen. For the same throughput, the streaming I/O implementation uses more resources but only about 65% of the power due to the slower clocking speed. If resource usage is more important (perhaps in the case when the design has to be tripled) the burst I/O implementation can be used, however it must be noted that this implementation must be clocked faster for the same throughput and thus will cost more power. For very high performance cases there will be a certain speed when only the streaming I/O FFT will reach the required clock rate.

Spartan-6 xc6slx45	1024 FFT, 16 bits, Unscaled, Truncation, Bit Reverse	
	Burst I/O@100 MHz	Streaming I/O@14 MHz
Power(W)	0.141 (D:0.093; Q:0.049)	0.074 (D:0.025; Q:0.049)
Slices (total 6822)	306	1,009
LUT-FF pairs	1,006	3,302
LUTs (total 27288)	848	2,989
FFs	1,160	4,124
DSP48A1s (total 58)	6	22
Spartan-6 xc6slx45	2048 FFT, 16 bits, Unscaled, Truncation, Bit Reverse	
	Burst I/O@100MHz CLK	Streaming I/O@14MHz CLK
Power(W)	0.116 (D:0.068; Q:0.048)	0.077 (D:0.028; Q:0.049)
Slices (total 6822)	334	1138
LUT-FF pairs	1041	3877
LUTs (total 27288)	871	3455
FFs	1238	4816
DSP48A1s (total 58)	6	28

Table 3.5: FFT power consumption and resource utilisation by throughput.

3.7 Summary

In this section state of the art on-board computer technology was presented. It was compared against the newly developed Steepest Ascent Mission Interface Computer (MIC). The MIC is designed to offer next generation performance capabilities while staying true to the CubeSat philosophy of low-cost and low-power. With these new advanced processing capabilities the opportunity to process data on-board a satellite opens up a number of possibilities for advanced missions facilitated through the application of advanced digital signal processing techniques.

The potential benefits offered by signal processing would increase the scope of CubeSat missions and help to alleviate many issues encountered by design teams regarding limited power and processing capabilities. As mission goals become more sophisticated the need is evident for a highly reliable and low-power on-board computer; capable of operating on platforms carrying multiple payloads and offering a variable degree of signal processing power. This can be achieved using a system incorporating an FPGA as was shown in the case of the MIC and the high performance embedded computer.

Clever use of digital signal processing techniques allows throughput to be traded-off against power and resource utilisation. Making better use of available resources is especially relevant in the heavily constrained CubeSat form, thus any method that offers the chance to save resources or power is sure to appeal to any hardened nano-satellite developer. The next chapter investigates the use of CubeSats within formation flying and array processing, lying very much in the realm of the MIC's specifications.

Chapter 4

Fractal Formation Flying and Beamforming

4.1 Introduction

Chap. 2 introduced the concept of CubeSats and the challenges faced when designing for space. In Chap. 3 an overview of the current state of the art for CubeSat on-board processing was provided. This was presented in contrast to the Steepest Ascent Mission Interface Computer, which aims to provide a new level of processing capability to nano-satellite platforms while staying true to the CubeSat philosophy of low-cost and low-power.

In this chapter a formation flying based architecture is presented within the context of a distributed antenna array. The control algorithm presented makes use of artificial potential functions to form and maintain a network of self-similar groups. This produces a fractal shape which is considered for the first time as a distributed antenna array exploiting the recursive arrangement of its elements to augment performance. A 5-element Purina fractal is used as the base formation which is then replicated a number of times increasing the antenna-array aperture and resulting in a highly directional beam from a relatively low number of elements. Justifications are provided in support of the claimed benefits for distributed antenna arrays exploiting fractal geometries. The formation deployment is simulated in Earth orbit together with analytical proofs completing the arguments aimed to demonstrate feasibility of the concept and the advantages provided by grouping antenna elements into coherent structures.

4.2 Motivation

The value of exploiting formation flight techniques for space science, remote sensing and telecommunications applications is gaining popularity [76, 77, 78, 79, 80]. So far proposed formation flying concepts have been based on a relatively low number of cooperating spacecraft, as in the case of Lisa, Proba-3 or StarLight missions [81, 82, 83]. The exploitation of a formation flight architecture with an increased number of elements which maintains an acceptable level of system complexity can be pursued through the control of autonomous and independent agents as a single group entity [77, 84].

Coupling reliable formation flying capabilities with the possibility of producing complex patterns using spacecraft will enable the potential of grouping a number of antenna elements into a cooperative structure. This has long been known and applied in antenna array theory [4, 5] and proposed at conceptual level for space applications [6, 7, 8].

The key point in the exploitation of formation flying techniques for the deployment of an antenna array is that the performance of a homogeneous pattern of array elements can be matched or surpassed by fractal geometries as per [9] and [10]. Fractal geometries as defined by [9] can be considered self-similar structures propagated from a core *initiator* through a number of stages of growth by an identical *generator*. Application of fractal geometries in antenna array design has mainly focussed on single structures, that is to say one device housing the antenna array. In this context each satellite houses an antenna which contributes to form the fractal pattern. Hence, the problem turns into producing a fractal pattern from a formation of spacecraft which provides a platform for a number of array elements able to exploit the fractal pattern characteristics.

From a control point of view one can consider to control at the same time the distance between pairs of spacecraft by projecting the error on two axes in the plane and applying a control law such as sliding mode, H-infinite or a PID. However, as evident in [85] potential based control methods are suitable choice and can be realised through Artificial Potential Functions (APFs) which represent a popular control method particularly suited to large structures of autonomous agents, such as discussed in e.g. [86, 87, 88]. The way to obtain complex formations through APFs, while maintaining a high degree of reliability and analytically provable characteristics, can be revealed through the design of a limited connection network. Network characteristics reflect on the final pattern deployed through an APF acting along its edges. In particular when the connection network presents self-similarity characteristics, i.e. the same network structure repeats for nodes and groups of nodes, this impacts not only on the final formation but also on the stability and robustness properties which are the same when considering the control of single spacecraft or groups of those. As consequence the overall control architecture result is scalable and possesses a certain degree of fault tolerance.

From the array point of view, self-similarity and sparseness lead to a number of benefits — deterministic performance in operation due to the repetitive nature of the array pattern, array performance degrades gracefully with element failure and finally equivalent performance can be achieved for a fraction of the number of elements used in square lattice arranged arrays [89].

This chapter proposes the deployment of a distributed fractal antenna array across a large group of satellites. Previous works [8, 7] have discussed the benefits of flying an arbitrary formation of distributed antenna elements to take advantage of the lower risks and costs associated with a network compared to a single large element. On the other hand there are examples in literature that investigate the benefits of a fractal shaped monolithic antenna [9]. The present work merges for the first time the concepts of distributed antenna arrays, fractal geometries and formation flying. The inherent control complexity is reduced through joint control techniques making use of APF and a self-similar communication network. In a similar fashion the overall antenna gain and performance is increased, even though when compared to a similar performing planar structure a reduced set of radiating elements is used. A description of the theoretical background is provided in Sec. 4.3 and is followed by a more detailed mathematical analysis related to the specific problem in Sec. 4.4. The topics covered include: the control method in terms of the APF characteristics and communication network; as well as an overview of fractal antenna theory, its application to a specific geometry and the resulting performance. In Sec. 4.5 numerical simulations are performed for the case of an architecture in geostationary orbit although the set of equations used is valid in general for circular orbits and nothing prevents the concept from being applied to any other orbit. Discussion and Conclusions follow in Sec. 4.6 and Sec. 4.7 respectively. This chapter demonstrates the potential of implementing an innovative architecture based on multiple autonomous spacecraft forming a fractal array.

4.3 Methodology

A group of N spacecraft is considered, divided into subgroups of n agents such that $N = n^k$ with $k \in \mathbb{N}^+$. It is assumed that each spacecraft carries an element of the array where the pair *spacecraft-array element* will be named from here on as agent. *Spacecraft* and *array element* will instead be used when referring to these components of the complete system. The agents are connected according to a non directional graph described by an adjacency matrix $\mathbf{A} \in \mathbb{N}^{N\times N}$ containing binary elements a_{ij}, with $i, j \in [1, N]$. The spacecraft are controlled through pairwise APFs which act only along the edges of the graph. There is no global position or orientation of the agent formation, but within the formation, relative positions are considered for agents and groups of agents while relative orientation is considered for groups of agents only. This implies that the single array elements are pointed correctly or, as assumed here, are isotropic sources.

This section shows how a self-similar formation can be obtained from mutually interacting agents, and how the array performance can be analysed for such a system. For this purpose artificial potential function characteristics and communication graph topology are described. The fundamental concept of applying fractal geometries to the design of antenna arrays using a self-scaling method is described for the case of planar configurations only, although similar arguments can be applied to linear and 3D formations.

4.3.1 Artificial Potential Functions

The spacecraft are controlled through Artificial Potential Functions (APFs) operating along the edges of a communication network. The APFs operate on a pairwise basis, that is they do not depend on position or velocity of the agents but only on their state relative to the other spacecraft with which they are connected; in particular the Morse potential is used. This is composed of an attractive component

$$U_{ij}^a = -C_{ij}^a \exp\left(-\frac{|\mathbf{x}_{ij}|}{L_{ij}^a}\right) \tag{4.1}$$

and a repulsive component

$$U_{ij}^r = C_{ij}^r \exp\left(-\frac{|\mathbf{x}_{ij}|}{L_{ij}^r}\right) \quad , \tag{4.2}$$

where C_{ij}^a and C_{ij}^r are constants regulating the magnitude of the potential, while L_{ij}^a and L_{ij}^r are constants related to the attractive and repulsive scale lengths. The subscripts i, j refer to the potential sensed by agent i because of interaction with agent j. The relative position vector of agent i with respect to agent j is denoted by $\mathbf{x_{ij}}$. The control law is completed by a virtual viscous-like damping in the form $\sigma\mathbf{v}_i$, with σ being a damping positive constant to be defined later and $\mathbf{v}_i$ representing agent velocity. This control law together with the hypothesis of no external disturbances and idealised sensing and actuation capabilities results in the motion equations

$$\dot{\mathbf{x}}_i = \mathbf{v}_i \tag{4.3}$$

$$m\dot{\mathbf{v}}_i = -\nabla U_i^a - \nabla U_i^r - \sigma\mathbf{v}_i \quad , \tag{4.4}$$

where m defines the agent mass and is assumed the same for all agents, and

$$\nabla(\cdot) = \frac{\partial(\cdot)}{\partial\mathbf{x}_i} \tag{4.5}$$

$$U_i^a = \sum_j (a_{ij} U_{ij}^a) \qquad \text{and} \qquad U_i^r = \sum_j (a_{ij} U_{ij}^r) \quad , \tag{4.6}$$

with a_{ij} being the entry of the adjacency matrix to be defined next.

4.3.2 Adjacency Matrix

As reported in Sec. 4.3.1, agents communicate through a network of links. In general in a network system studied through graph theory an adjacency matrix contains non-zero entries in the (i, j) location whenever there is a directed edge from node i to node j, indicating a communication link between the two agents represented by these nodes. Moreover the matrix is not weighted, i.e. the elements $a_{ij} \in \{0, 1\}$ are binary. The strength of the interactions is provided by the APF via (4.6). While the proposed adjacency matrix is symmetric, i.e. the graph is not directed, this does not imply that the virtual interactions amongst the agents are symmetric.

Within the adjacency matrix $\mathbf{A}$ for a system with $N = n^k$ agents, the edges belonging to fully connected n-agent subgroups form $n \times n$ submatrices along the block-diagonal. The remainder of the matrix contains links between agents in the n^{k-1} different subgroups.

Example 1. For the case $n = 5$ and $k = 2$, there are 5 subgroups creating 5×5 submatrices along the diagonal of the adjacency matrix, as indicated in Fig. 4.1. The communication between any pair of subgroups is maintained through one linking agent per subgroup (the central one), accounting for $n - 1$ connections each. Beside that relative orientation of peripheral subgroups with respect to the central one is ensured by 1 linking agents per peripheral subgroup connecting to the adjacent one in the central core.

Example 2. For the case $n = 5$ and $k = 3$, there are 25 subgroups creating 5×5 submatrices along the diagonal of the adjacency matrix. These ones are connected in groups of 5 as described in Example 1, and are represented by the 25×25 squares along the diagonal of Fig. 4.2. The communication between any pair of 25-agent subgroups is this time ensured by groups of 5 agents that replace the single agents of Example 1.

The network is designed such that the peripheral nodes are weaker than the central ones. This means that loss of control of one node due to loss of link is more likely for nodes that belong to peripheral region of the formation, hence they do not act as a bridge between large portions of the ensemble. This implies that the loss of some links is more likely to produce the disconnection of a smaller and peripheral portions of the network than of a large portion. Each node is in any case at least connected to $n - 1$ other nodes. When the number of generators increases, those groups which were end-points for the previous generator become embedded and more firmly bonded into the larger pattern. This ensures that in the most critical scenario the loss of at least $n - 1$ links is needed for fragmentation to occur. In

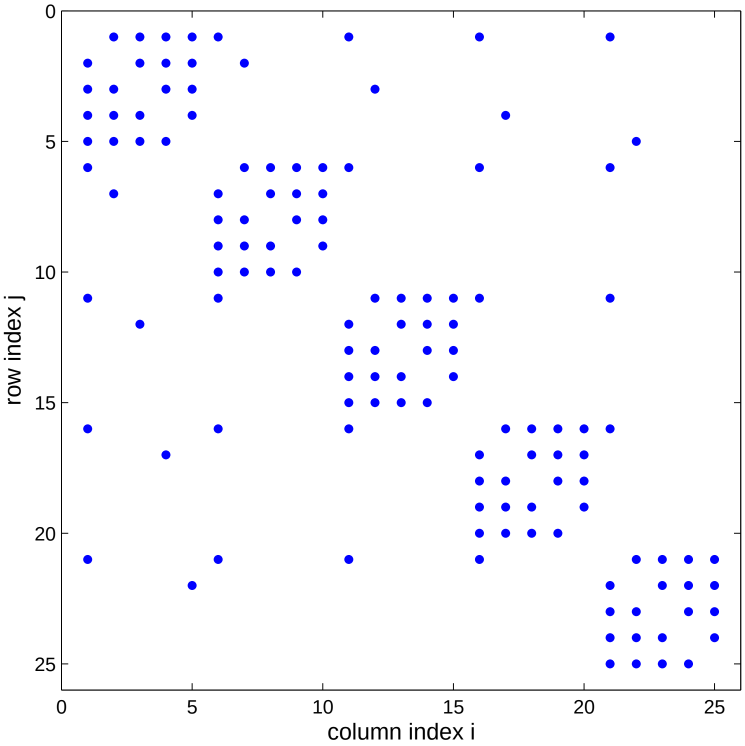

Figure 4.1: Adjacency matrix for the case $n = 5$ and $k = 2$, creating a group of $N = 25$ agents. Non-zero entries are represented by dots.

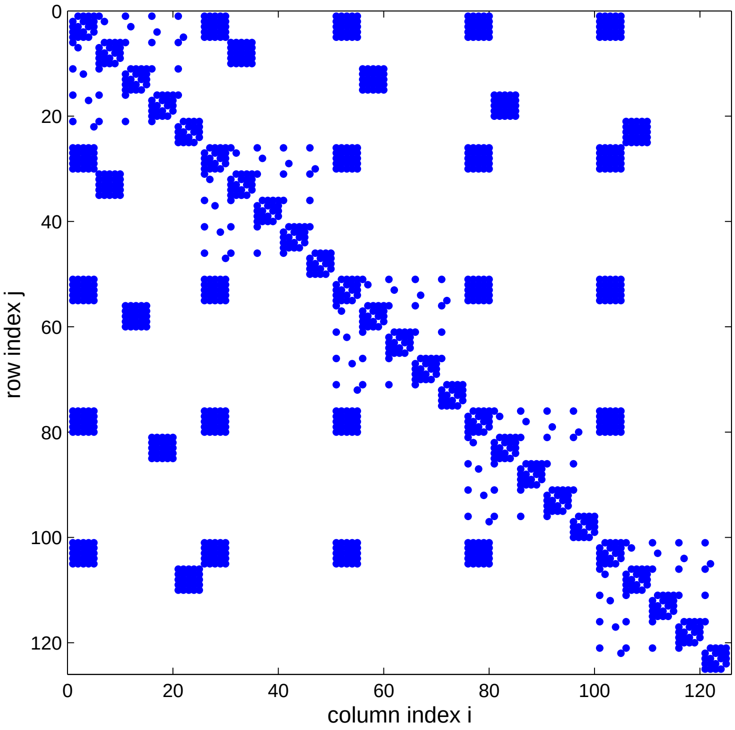

Figure 4.2: Adjacency matrix for the case $n = 5$ and $k = 3$, creating a group of $N = 125$ agents. The self-similarity of the matrix can be observed. The 25-agent matrix of Fig. 4.1 is replicated now 5 times along the diagonal and the other entry of the matrix, grouped ion 5×5 squares are in the same position as the links in the 25-agent matrix.

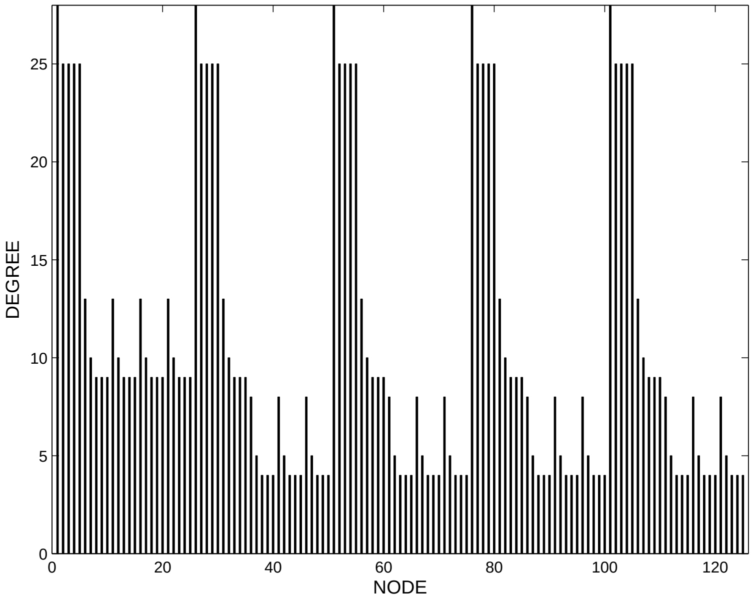

Figure 4.3: Node degrees as number of links belonging to each node. A self-similar scheme can be observed with nodes in central position being the most connected ones. In this scheme the maximum number of connections per node is 28.

Fig. 4.3 the node degree is reported for the adjacency matrix of dimension 125, that is the number of links each node is connected to. Nodes are sorted from the central to the peripheral ones.

4.3.3 Gain Response

This section provides the methods used to analyse the beamforming performance of a group of agents arranged into formation, utilising the above control methods. The analysis techniques presented apply in general to any planar array formation and determine the gain response or beam pattern of the array w.r.t. frequency and angle of arrival. First a review of the spatial and temporal sampling of a narrowband signal is provided, before the steering vectors that characterise the incident wave on the array are defined. This leads to the formulation of the general beam pattern which is often used to determine the performance of a beamformer; the response for a square full lattice array is presented.

The analysis below is performed for an array acting as a receiver, motivated by traditional notation of sources and corresponding steering vectors. The design of a beamformer for transmission is analogous, and we will return to this in Sec. 5.2.2. Since the focus of this work lies in the control of two-dimensional planar structures, only the design and analysis of planar fractal antenna arrays is described. As the proposed fractal antenna array is part of a satellite constellation whose aperture is small when compared to its orbit, Cartesian coordinates are used to describe it. The gain response, is generally derived from the product of the

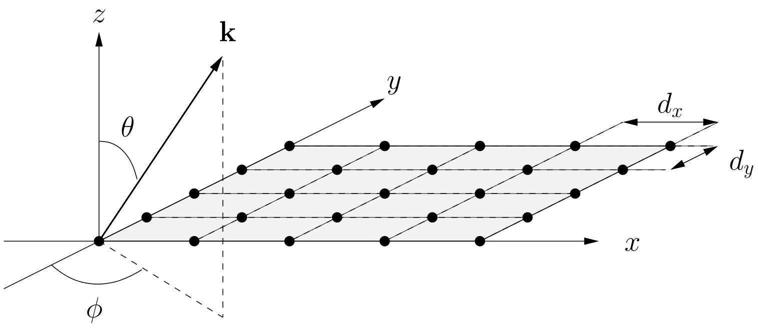

Figure 4.4: Symmetric planar array in the $x - y$ plane with inter-element spacings of d_x and d_y, and definition of spherical angles θ and ϕ for the wavenumber vector $\mathbf{k}$ of a farfield source.

steering vector and the radiation characteristics of the individual antenna array elements, is here only dependent on the angle of arrival since isotropic antenna elements are assumed.

Spatial and Temporal Sampling

To spatially sample a far-field signal $x(t)$ with power spectral density $S_{xx}(j\omega) = 0 \quad \forall|\omega| \geq \omega_{\max}$ by an array with M elements defined by element positions $\mathbf{r}_m$, $m = 1 \ldots M$, at least two array elements have to fulfil the minimum requirement

$$\min_{m,\mu} \|\mathbf{r}_m - \mathbf{r}_\mu\|_2 \leq \frac{\lambda_{\min}}{2} \tag{4.7}$$

in order to obtain an unambiguous representation free of spatial aliasing. The minimum wavelength

$$\lambda_{\min} = \frac{2\pi c}{\omega_{\max}} \tag{4.8}$$

relates to the maximum angular frequency $\omega_{\max}$ via the propagation speed c in the medium.

If the array acquires the continuous time signal $x(t)$, it will, due to its emanating from the far-field, arrive at the array in a planar wavefront characterised by a normal vector $\mathbf{k}$,

$$\mathbf{k} = \begin{bmatrix} \sin\vartheta\cos\varphi \\ \sin\vartheta\sin\varphi \\ \cos\vartheta \end{bmatrix} \quad , \tag{4.9}$$

with azimuth φ and elevation ϑ as defined in Fig. 4.4. Therefore the delay experienced by the mth array element relative to the origin is

$$x_m(t) = x(t - \Delta T_m) = x(t - \frac{\mathbf{k}^{\mathrm{T}}\mathbf{r}_m}{c}) \quad , \tag{4.10}$$

where $\mathbf{k}/c$ is also known as the slowness vector.

Temporal sampling of $x_m(t)$ with a sampling period T_s leads to

$$\begin{aligned} x_m[n] &= x_m(nT_\mathrm{s} - \Delta T_m) = x_m((n - \frac{\mathbf{k}^\mathrm{T}\mathbf{r}_m}{cT_\mathrm{s}})T_\mathrm{s}) \\ &= x_m[n - \tau_m] \end{aligned} \tag{4.11}$$

where $\tau_m = \frac{\mathbf{k}^\mathrm{T}\mathbf{r}_m}{cT_\mathrm{s}}$. Specifically considering a complex exponential $x(t) = e^{j\omega t}$,

$$x_m[n] = e^{j\omega(n-\tau_m)T_\mathrm{s}} = e^{j\Omega n} e^{-j\Omega\tau_m} \quad , \tag{4.12}$$

for this narrowband excitation the time delay ΔT_m turns into a phase shift $\Omega\tau_m$.

Steering Vector and Quiescent Beamformer

For the narrowband excitation in (4.12), concatenating all sensor signals $x_m[n]$ into a vector $\mathbf{x}[n]$,

$$\mathbf{x}[n] = \begin{bmatrix} x_1[n] \\ x_2[n] \\ \vdots \\ x_M[n] \end{bmatrix} = e^{j\Omega n} \begin{bmatrix} e^{-j\Omega\tau_1} \\ e^{-j\Omega\tau_2} \\ \vdots \\ e^{-j\Omega\tau_M} \end{bmatrix} = \sqrt{M} e^{j\Omega n} \mathbf{s}_{\varphi,\vartheta,\Omega} \tag{4.13}$$

yields the unit norm steering vector $\mathbf{s}_{\varphi,\vartheta,\Omega}$, which uniquely characterises a source of normalised angular frequency Ω coming from a direction defined by azimuth φ and elevation ϑ through the dependency on $\mathbf{k}$.

To calculate beamforming coefficients $\mathbf{w}$ that fulfil the constraint $\mathbf{w}^\mathrm{T}\mathbf{s}_{\Omega_0,\varphi_0,\vartheta_0} = 1$ while minimising the impact of isotropic noise, the quiescent solution is the matched filter, $\mathbf{w} = \mathbf{s}_{\Omega_0,\varphi_0,\vartheta_0}$.

Beam Pattern

To characterise a beamformer with coefficient vector $\mathbf{w}$ adjusted for a source with parameter set $\{\Omega_0, \varphi_0, \vartheta_0\}$, the beam or directivity pattern

$$G(\Omega, \varphi, \vartheta) = \mathbf{w}^\mathrm{H}\mathbf{s}_{\Omega,\varphi,\vartheta} \tag{4.14}$$

measures the gain with respect to potential sources over a grid of frequencies and angles of arrival by scanning the coefficient vector with the resulting set of steering vectors. This power variation as a function of the arrival angle is observed in the far field and provides a metric to analyse the performance of the beamformer.

4.3.4 Fractal Array

Fractals and fractal geometry [90] were introduced to describe naturally occurring irregular but self-similar structures, and have since found bearing in a wide range of scientific and engineering fields. For the particular application of a distributed antenna array in the context of satellite formation flying and fractionated space craft, [91, 92] fractals have been found to be advantageous due to their rapid growth and relatively low number of elements. The self-replicating nature of fractal patterns extends to their performance characteristics too; this means that rapid analysis of a wide range of antenna characteristics is possible for different growth scales for a particular fractal and is true for other fractal patterns too [9].

Deterministic fractal arrays are constructed in a self-similar manner and consist of many smaller parts whose shape resembles that of the overall object. They are formed by the repetition of a generating sub-array [9] at growth scale, $P = 1$; to construct higher scales of growth, repetitions of this small sub-array are used. The pattern of the generating sub-array is achieved by switching elements of a fully populated symmetric array on or off according to:

$$S_{mn} = \begin{cases} 1, & \text{if element } (m,n) \text{ is turned on} \\ 0, & \text{if element } (m,n) \text{ is turned off} \end{cases} \quad , \tag{4.15}$$

until the desired fractal pattern emerges. The thinned generating sub-array is then copied, scaled and translated to produce the final array. The array fractal pattern S_P at an arbitrary growth scale $P \in \mathbb{N}$, $P \geq 2$ is given by

$$\mathrm{S}_P = \mathrm{S}_1 \otimes \mathrm{S}_{P-1} \quad , \tag{4.16}$$

with $\otimes$ denoting the Kronecker product. Due to the recursive nature of the development procedure, deterministic fractal arrays created in this manner can conveniently be thought of as arrays of arrays. Fig. 4.5 shows some popular fractal arrays, demonstrating their initiator at stage 1 and the subsequent stages of growth.

Utilising the control methods defined above it is possible to group a number of smaller distributed antenna elements into a fractal array. The resulting array may then be analysed as a beam former using the gain response techniques detailed. The design and analysis of a fractal beamforming array provides a number of potential benefits in the context of space communications, including increase aperture at a reduced cost, improved performance and risk mitigation due to reduced number of antenna array elements.

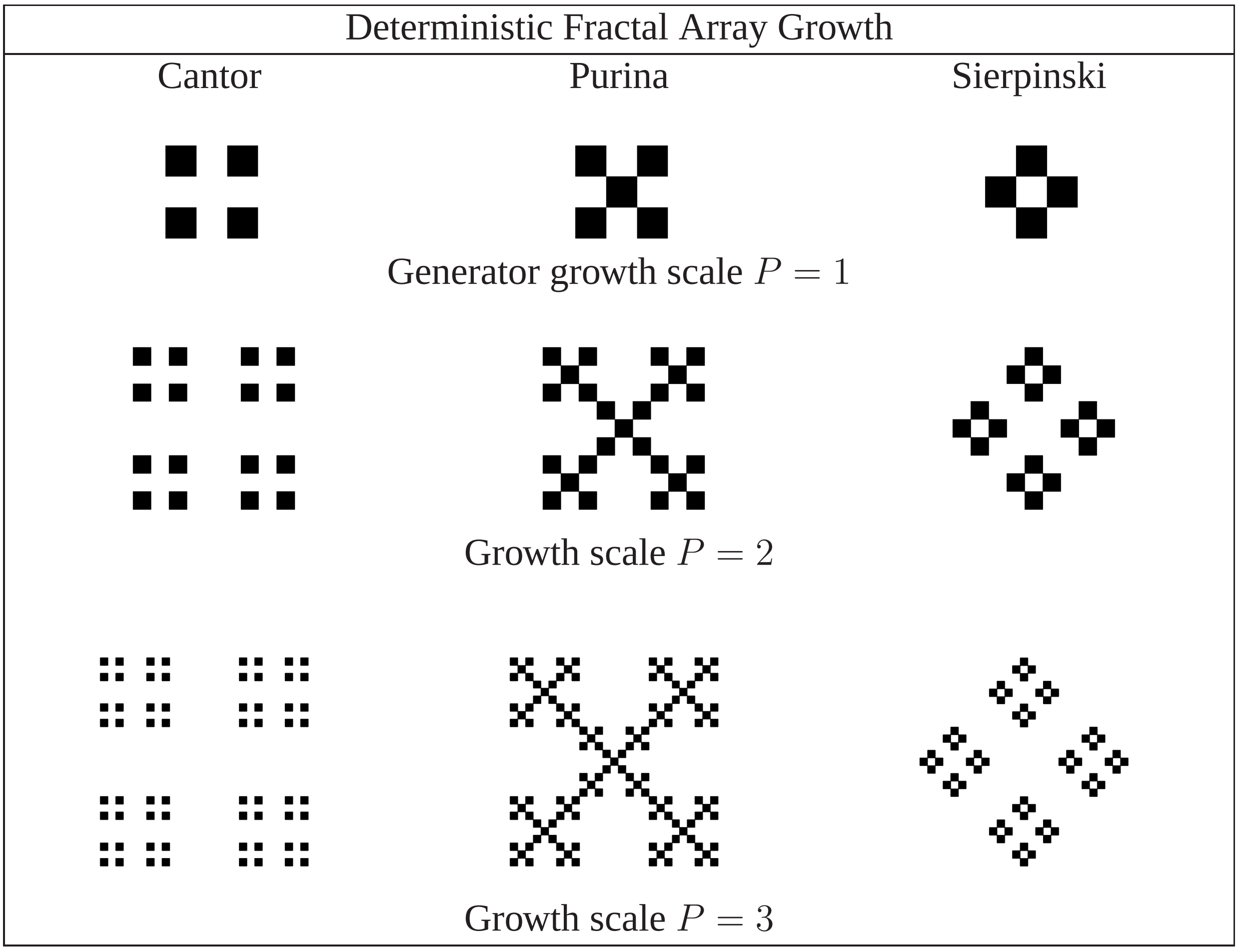

Figure 4.5: Initiator and first few stages of deterministic fractal array growth for: Cantor, Purina and Siepinski fractals.

4.4 Control Law and Fractal Beamformer Analysis

In this section the characteristics of the control technique used to drive an ensemble of agents towards the formation of a fractal pattern and the issues related to the design of a fractal shaped beamformer array are considered. It is first shown how asymmetry in attraction-repulsion potential leads necessarily to a central symmetry configuration. It is then shown how the APF coefficients are calculated in order to get the desired distance between agents. Analysis of the control law is completed by considering the non-linear stability characteristics. Beamformer design methodology is finally illustrated in detail for the case of a *Purina* fractal array — from a control perspective any fractal geometry that is two fold symmetric may be chosen. From those shown in Fig. 4.5 the Purina is a suitable choice. As a beamformer the Purina offers an almost 50% reduction in the number of array elements needed. The shape of this fractal as shown in Fig. 4.5 also means the spacing between sub-arrays maintains the critical sampling space such that (4.7) holds; the same cannot be said for the Cantor and Sierpinski geometries. With reference to Sec. 4.3, from now on only the case of

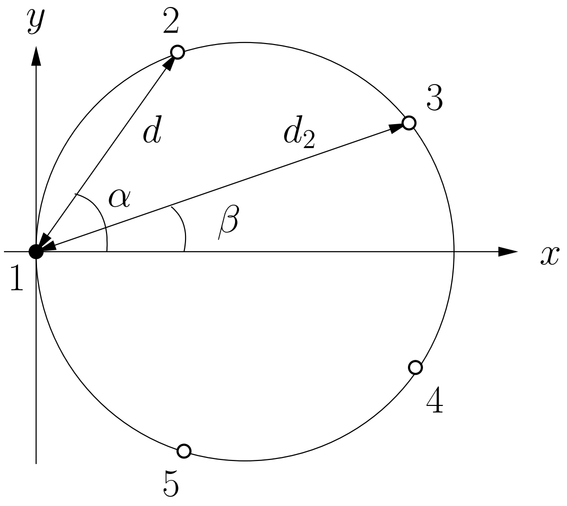

Figure 4.6: Configuration with 5 agents — all having APFs with identical coefficients — arranged in a homogeneous formation.

an initiator of $n = 5$ elements is considered.

4.4.1 Central Symmetry Emergence

Central symmetry emerges at initiator level by means of asymmetry between the interactions of one single agent with the group. This is obtained through a different value of the L^r_{ij} parameter along the directed edges connecting the agent to the other 4 in the initiator structure. This is here explained by finding the conditions that make the artificial potential derivatives null along two orthogonal axes which are centred on the agent considered and define the plane where the control is exerted. The out of plane motion is undertaken through other means and is explained in Sec. 4.5. Considering the 5-agent scheme, given in Fig. 4.6, the first derivative of the artificial potential sensed by agent 1 can be calculated for the regular pentagon formation pictured. Then the conditions that apply to the APF coefficients in order to reach a stable equilibrium are deduced. APF derivatives can be calculated as

$$\frac{\partial U_i}{\partial x_i} = \sum_{j=1}^{n}\left(\frac{C^a_{ij}}{L^a_{ij}}\exp\left(-\frac{|\mathbf{x}_i-\mathbf{x}_j|}{L^a_{ij}}\right)-\frac{C^r_{ij}}{L^r_{ij}}\exp\left(-\frac{|\mathbf{x}_i-\mathbf{x}_j|}{L^r_{ij}}\right)\right)\frac{x_i-x_j}{|\mathbf{x}_i-\mathbf{x}_j|} \tag{4.17}$$

$$\frac{\partial U_i}{\partial y_i} = \sum_{j=1}^{n}\left(\frac{C^a_{ij}}{L^a_{ij}}\exp\left(-\frac{|\mathbf{x}_i-\mathbf{x}_j|}{L^a_{ij}}\right)-\frac{C^r_{ij}}{L^r_{ij}}\exp\left(-\frac{|\mathbf{x}_i-\mathbf{x}_j|}{L^r_{ij}}\right)\right)\frac{y_i-y_j}{|\mathbf{x}_i-\mathbf{x}_j|} \tag{4.18}$$

with $U_i = U^a_i + U^r_i$. Excluding the trivial case for $L^r{}_{ij} = L^a_{ij}$ and $C^r_{ij} = C^a_{ij}$, (4.17) and (4.18) can be driven to zero while satisfying the stability conditions $L^r{}_{ij} < L^a_{ij}$ [87]. From here on, just changes in $L^r{}_{ij}$ are considered, where i, j refers to the indexing within the 5 agent group. In contrast, L^a_{ij}, C^a_{ij} and C^r_{ij} are considered independent from the pair of agents i.e. they take the same value for every index i, j and will hence be omitted below.

Taking the planar formation in Fig. 4.6, the equilibrium along y is trivially satisfied for all possible distances d either in case ${L^r}_{ij} = L^r$ for all (i, j), that is it takes the same values along all the edges, or in the case one agent has a different repulsive scale distance. This can be understood by simply considering the symmetry of the formation about x-axis. Equilibrium along the x-axis does not lead to an explicit expression for the equilibrium distance, nonetheless the derivative of the potential w.r.t. x referring to any agent can be calculated. Due to the homogeneity of the configuration any agent can be taken to analyse the artificial potential field. In particular for agent 1,

$$\begin{aligned}\left.\frac{\partial U_1}{\partial x_1}\right|_{\text{pentagon}} &= 2\frac{C^a}{L^a}\left(\exp\left(-\frac{d}{L^a}\right)\cos\alpha + \exp\left(-\frac{d_2}{L^a}\right)\cos\beta\right) \\ &\quad -2\frac{C^r}{L^{r\prime}}\left(\exp\left(-\frac{d}{L^{r\prime}}\right)\cos\alpha + \exp\left(-\frac{d_2}{L^{r\prime}}\right)\cos\beta\right) \quad ,\end{aligned} \tag{4.19}$$

where

$$d_2 = \frac{d}{2}\sqrt{\left(\tan\alpha + \frac{1}{\cos\alpha}\right)^2 + 1} = kd \tag{4.20}$$

can be determined, with $k > 1$. This is considered as an initial equilibrium scenario for some equilibrium distance d and for $L^r = L^{r\prime}$ that is the same repulsive scale distance sensed by all the agents. In this scenario (4.19) must equal zero, but if $L^r \neq L^{r\prime}$ and in particular $L^r < L^{r\prime}$ the separation distance must shrink. Thus the equilibrium distance reduces as the scale separation distance shrinks. This can be verified by differentiating (4.19) w.r.t. $L^{r\prime}$, leading to

$$\begin{aligned}\frac{\partial\left(\left.\frac{\partial U_1}{\partial x_1}\right|_{\text{pentagon}}\right)}{\partial L^{r\prime}} &= 2\frac{C^r}{L^{r\prime 2}}\left(\exp\left(-\frac{d}{L^{r\prime}}\right)\cos\alpha + \exp\left(-\frac{kd}{L^{r\prime}}\right)\cos\beta\right. \\ &\quad \left. -\frac{d}{L^{r\prime}}\exp\left(-\frac{d}{L^{r\prime}}\right)\cos\alpha - \frac{kd}{L^{r\prime}}\exp\left(-\frac{kd}{L^{r\prime}}\right)\cos\beta\right)\end{aligned} \tag{4.21}$$

The expression in (4.21) is negative definite, since a reduction of $L^{r\prime}$ produces an acceleration on agent 1 in the direction of the positive x-axis and therefore leads to a reduction of its equilibrium distance,

$$\frac{\partial\left(\left.\frac{\partial U_1}{\partial x_1}\right|_{\text{pentagon}}\right)}{\partial L^{r\prime}} < 0 \tag{4.22}$$

$$\therefore \quad \left(1 - \frac{d}{L^{r\prime}}\right)\left(\exp\left(-\frac{d}{L^{r\prime}}\right)\cos\alpha\right) + \left(1 - \frac{kd}{L^{r\prime}}\right)\left(\exp\left(-\frac{kd}{L^{r\prime}}\right)\cos\beta\right) < 0 \tag{4.23}$$

This is always satisfied for $d > L^{r\prime}$. The *sufficient condition* $d > L^{r\prime}$ can be obtained by a

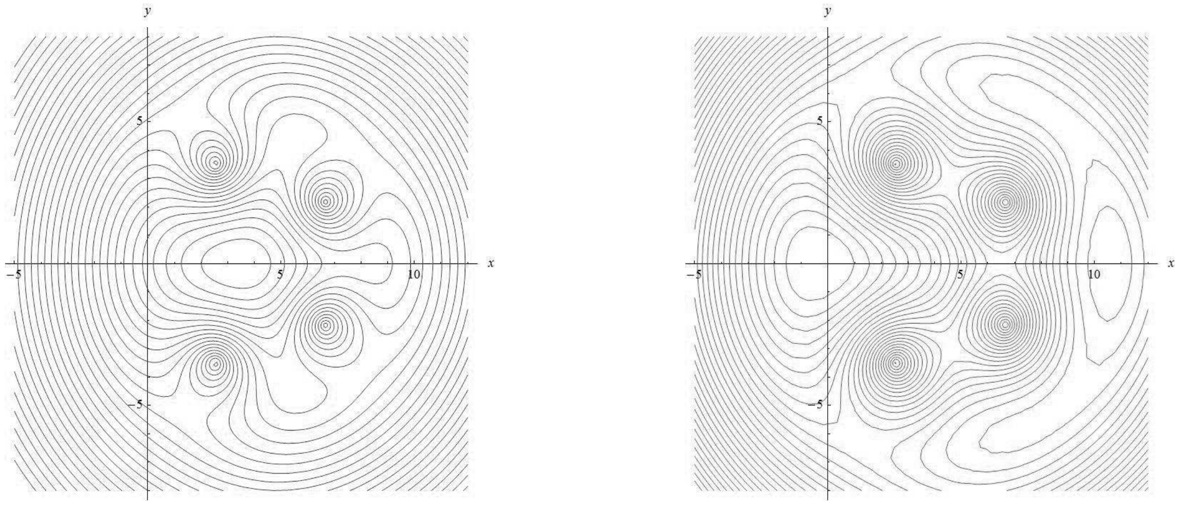

(a) (b)

Figure 4.7: Contours for the potential sensed by an agent at the origin (a) in case all other agents have the same value of the repulsive potential scale length L^r and (b) in case one of the other agents has a repulsive scale distance $L^{r\prime} < L^r$.

wide choice of system parameters, which can be easily seen by inspecting the equilibrium distance for the simple case of two agents. This case is obtained by summing up and setting equal to zero the derivatives in (4.1) and (4.2) for $|\mathbf{x}_{ij}|_2 = d$, and then solving for d,

$$d = \frac{L^a L^r}{L^r - L^a} \ln \frac{C^a L^r}{C^r L^a} > L^r \quad . \tag{4.24}$$

In particular for $C^a = C^r$ the relationship shown in (4.24) is true as long as $L^a \neq L^r$. However, as stability imposes $L^a > L^r$, to make the potential function convex in the vicinity of the equilibrium, it can be concluded that Eq. (4.24) is always verified for stable potentials and possible to achieve for other choices of the parameters C^a and C^r.

The other agents in the group considered in Fig. 4.6 tend to keep the same relative distance w.r.t. agent 1. This produces the new equilibrium configuration that sees the agent with reduced separation distance finding its equilibrium position in the centre of the 5-agent group while also fulfilling equilibrium conditions for the other agents. A contour plot of the potential which agent 1 senses is reported in Fig. 4.7 for both equilibrium and non-equilibrium parameter choices. By similarly working the C^r parameter, the same effect can be obtained as (4.19) is linear in C^r. Here, parameter $L^{r\prime}$ is used to force the central symmetry configuration over the pentagon one, while parameter C^r is used to produce the desired inter-agent distance only. The cross configuration generated by the asymmetry in the potential repulsive scale length is sketched in Fig. 4.8.

Considering that interactions amongst agents are only along the edges of the adjacency matrix, a representation of the repulsive and attractive scale parameter as well as of the other

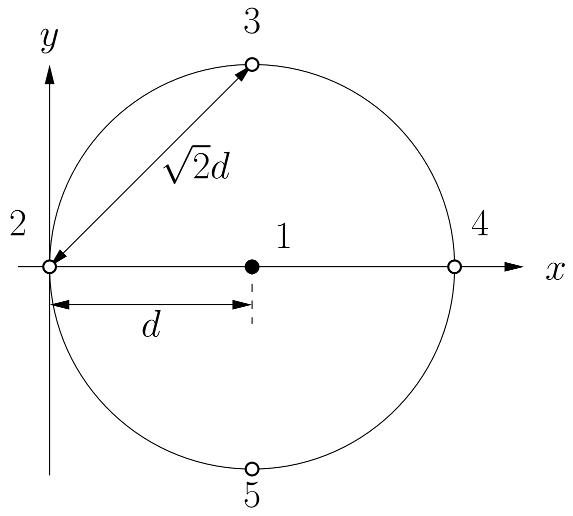

Figure 4.8: Cross pattern emerging by shrinking the repulsive potential scale length broadcasted for the agent in the centre.

coefficients influencing (4.1) and (4.2) can be given in terms of matrix which have the same structure of the adjacency matrix described in Sec. 4.3. An extract from the top left-hand corner of the repulsive distance matrix is given by

$$\begin{bmatrix} 0 & L^r & L^r & L^r & L^r & L^r_2 & 0 & 0 & \\ L^{r\prime} & 0 & L^r & L^r & L^r & 0 & L^r_3 & 0 & \\ L^{r\prime} & L^r & 0 & L^r & L^r & 0 & 0 & 0 & \\ L^{r\prime} & L^r & L^r & 0 & L^r & 0 & 0 & 0 & \cdots \\ L^{r\prime} & L^r & L^r & L^r & 0 & 0 & 0 & 0 & \\ L^{r\prime}_2 & 0 & 0 & 0 & 0 & 0 & L^r & L^r & \\ 0 & L^r{}_3 & 0 & 0 & 0 & L^{r\prime} & 0 & L^r & \\ 0 & 0 & 0 & 0 & 0 & L^{r\prime} & L^r & 0 & \\ & & & \vdots & & & & & \ddots \end{bmatrix}, \qquad (4.25)$$

where zeros are in the same positions in the adjacency matrix in Figs. 4.1 and 4.2, and where the coefficients regulating the interactions among nodes which are centres of two different 5-agent groups are denoted by $L^r{}_2$. Finally $L^r{}_3$ is used to indicate the value along the edges connecting peripheral agents across different 5-agent groups. Hence coefficients L^r, L^a , C^r and C^a can be arranged in square matrices of dimension N; as these coefficients refer to the edges of the graph, they take a different value depending on which agent the edge is connected to.

One consideration which is worth noting is that arrangement in pentagon configuration is not guaranteed by the condition $L^{r\prime} = L^r$. While having $L^{r\prime} \neq L^r$ will for sure exclude an equilibrium configuration in the shape of a pentagon, the contrary cannot be stated. The cross configuration in Fig. 4.8 can be obtained for both the choices of $L^{r\prime}$ considered. From this point of view, excluding one of the two configurations can be seen as a method for escaping one local minimum configuration.

When considering a cross configuration as in Fig. 4.8, differently from the pentagon case, the potential field for the agent in the centre cannot be considered as for the others. Anyway it is in equilibrium whatever choice of L^r parameter is made. This is due to the symmetry of potential acting on this agent which translates into two pairs of equal and opposite terms for the sums in (4.17) and (4.18) making both equations trivially null. For this reason the agent with $L^r = L^{r\prime}$ will find its equilibrium position at the centre enabling the cross formation. This also justifies the consideration about the two possible arrangements for agents with the same repulsive scale distance parameter: being the central position an equilibrium one, also a group of agents with the same repulsive potential can spontaneously arrange in a cross configuration. Equilibrium for the surrounding agents according to the scheme of Fig. 4.8 is only determined by (4.17), as the y-component is null by symmetry. The equilibrium distance d as shown in Fig. 4.8 is found by solving for the value d that satisfies

$$\frac{C^r}{L^r}\left(\exp\left(\frac{-d}{L^r}\right)+\exp\left(\frac{-2d}{L^r}\right)+\sqrt{2}\exp\left(\frac{\sqrt{2}d}{L^r}\right)\right)= \\ \frac{C^a}{L^a}\left(\exp\left(\frac{-d}{L^a}\right)+\exp\left(\frac{-2d}{L^a}\right)+\sqrt{2}\exp\left(\frac{-\sqrt{2}d}{L^a}\right)\right) \quad , \tag{4.26}$$

which is obtained by expanding (4.17). As it can be seen there is no closed-form analytical solution. On the other hand, a stable equilibrium distance exists for a choice of the free parameters C^a, C^r, L^a and L^r satisfying the conditions stated in [88]. In particular for given L^r and L^a, with $L^a > L^r$, a stable equilibrium can be found by tuning the parameters C^a and C^r. This is further elaborated in Sec. 4.6.

4.4.2 APF Coefficient Definition

The coefficients of the APF acting along the edges of the graph are calculated such to set the desired distance amongst the spacecraft. Just the C^r coefficient is calculated as function of the others which are set. The change of C^r parameter only or, more precisely, the change in the ratio C^r/C^a is sufficient to modify the position of the minimum, hence the design distance, for the APF used. In particular, an interaction between two spacecraft belonging to two different n-agent groups is considered, with a design distance d_d; C^r coefficient can be hence calculated by manipulating (4.24) as

$$\frac{C^r}{C^a}=\frac{L^r}{L^a}\exp\left(d_d\frac{L^a-L^r}{L^aL^r}\right) \quad . \tag{4.27}$$

Once the coefficients are set, (4.27) can be reversed to calculate the equilibrium distance. When more than 2 agents are involved, an analytic expression for the equilibrium distance cannot be defined, but given a desired distance, one can always get an expression for the value of the ratio C^r/C^a that produces that separation. In particular for a fully connected group of 5 agents C^r/C^a ratio can be calculated equating to zero the gradient of the potential for the formation according to the scheme in Fig. 4.8. As the y-component is trivially null, C^r/C^a can be calculated considering just x-component of the gradient in (4.17). This corresponds to (4.26), which can be manipulated algebraically to obtain

$$\frac{C^r}{C^a} = \frac{L^r}{L^a} \frac{\exp\left(-\frac{d_d}{L^a}\right) + \exp\left(-\frac{2d_d}{L^a}\right) + \sqrt{2}\exp\left(-\frac{\sqrt{2}d_d}{L^a}\right)}{\exp\left(-\frac{d_d}{L^r}\right) + \exp\left(-\frac{2d_d}{L^r}\right) + \sqrt{2}\exp\left(-\frac{\sqrt{2}d_d}{L^r}\right)} \quad . \tag{4.28}$$

This tuning method can be extended to the other links of the adjacency matrix; by defining the coefficients in this way the desired self-similar pattern is produced.

4.4.3 Stability of Control Law

The stability can simply be proved following a procedure similar to the one in [87]. Consider the time derivative of the energy as sum of artificial potential and real kinetic energy,

$$\frac{dE_t}{dt} = \frac{dK_t}{dt} + \frac{dU_t}{dt} \quad , \tag{4.29}$$

where

$$U_t = \frac{1}{2}\sum_i \sum_j a_{ij} U_{ij} \tag{4.30}$$

is the total potential energy time derivative per unit mass with

$$U_{ij} = U_{ij}^a + U_{ij}^r \quad , \tag{4.31}$$

and

$$K_t = \frac{1}{2}\sum_i K_i = \frac{1}{2}\sum_i (\mathbf{v}_i \cdot \mathbf{v}_i) \tag{4.32}$$

the total kinetic energy time derivative per unit mass. Expanding (4.29),

$$\frac{dE_t}{dt} = \sum_i \left(\nabla U_t \cdot \mathbf{v}_i + \frac{\partial K_t}{\partial \mathbf{v}_i} \cdot \dot{\mathbf{v}}_i \right) \tag{4.33}$$

where the gradient operator $\nabla(\cdot)$ is defined in (4.5). Substituting (4.4) and (4.31) into (4.33) yields

$$\frac{dE_t}{dt} = \sum_i \left[\nabla U_t \cdot \mathbf{v}_i + \frac{\partial K_t}{\partial \mathbf{v}_i} \cdot (-\nabla U_i - \sigma \mathbf{v}_i)\right] \tag{4.34}$$

$$\therefore \frac{dE_t}{dt} = \sum_i \left[(\nabla U_t \cdot \mathbf{v}_i - \nabla U_i \cdot \mathbf{v}_i) - \sigma |\mathbf{v}_i|^2\right] \quad . \tag{4.35}$$

As the potential depends upon pairwise interactions, the derivative w.r.t. $\mathbf{x}_i$ is not null for both the U_{ij} and U_{ji} potentials that constitute the total potential U_t. If the agents interacted in a symmetric way, this would cancel out with the gradient ∇U_i, but as the sum of the potential derivatives upon any agent includes asymmetric terms, this does not occur. Nevertheless the difference between the gradients can be always damped by the artificial viscous damping. Hence, it can be concluded that

$$\exists\, \sigma > 0 : \sum_i \left[(\nabla U_t \cdot \mathbf{v}_i - \nabla U_i \cdot \mathbf{v}_i) - \sigma |\mathbf{v}_i|^2\right] \leq 0 \quad . \tag{4.36}$$

This is enabled by the fact that artificial potential and its derivative are bounded functions.

As total energy time derivative can be made a negative semi-definite function, this can be compared to a Lyapunov-like function whose derivative is always proved to be negative and zero at equilibrium, corresponding to null speed. Thus the system will leak energy and stabilise eventually into a static formation which corresponds to the minimum of total energy.

The stability characteristic outlined above does not imply that the system will relax into the desired formation as the energy might be minimized, even just in local sense, with a configuration that is not the one the system was meant to take.

4.4.4 Fractal Array Design and Beamformer Analysis

Distributing the array sensors of a beamformer across a satellite formation offers the potential of improved directivity and gain for increasing number of elements. However, controlling a large number of satellites flying in relatively close proximity to one another does not provide a convenient solution. A more practical design would involve a formation with a reduced number of elements offering similar performance. Basing array formations on the fractal geometries described in Sec. 4.3 has the potential to reduce the number of elements without affecting the performance.

The method described in Sec. 4.3.4 and Sec. 4.3.3 are followed here to design and analyse a planar array based on the Vicsek or Purina fractal. A 3×3 symmetric planar array is thinned down to form the Purina fractal pattern which has the simple sub-array S_1 at growth scale $P = 1$,

$$\mathrm{S}_1 = \begin{bmatrix} 1 & 0 & 1 \\ 0 & 1 & 0 \\ 1 & 0 & 1 \end{bmatrix} \quad . \tag{4.37}$$

where a unit entry means that an array element is present, while a zero indicates the absence of an element. Using Eq. 4.16 the array fractal pattern at an arbitrary growth scale P is easily determined. Fig. 4.9 shows the Purina fractal array at growth scale $P = 3$. Highlighted in the figure are the generating sub-array, $P = 1$ and sub-sequent growth stage at $P = 2$.
To demonstrate the performance of the Purina beamformer the design parameters $\Omega_0, \varphi_0, \vartheta_0$, as defined in Sec. 4.3.3, are set up to look towards broadside, with $\varphi_0 = \vartheta_0 = 0°$. $\Omega_0 = \pi$ in this case represents the maximum normalised angular frequency, assuming critical sampling in space, such that (4.7) holds with equality, and in time with $f_\mathrm{s} = 2f_\mathrm{max}$.
For the Purina array as described above, Fig. 4.10 shows a cross-sectional view ($\vartheta = 0°, \varphi = 0°$) of the resulting beam pattern for the first three stages of growth for the Purina beamformer. The main beam is more focused at higher scales of growth due to the increased effective aperture of the array. The self-similarity of the fractal geometry is evident in the gain response, lower stages of growth forming an envelope for the following stages. This artefact allows designers to quickly assess performance w.r.t increased scale and complexity.

For the same beamformer, Fig 4.11 shows a 3-dimensional polar plot of the gain response of the array at growth scale $p = 3$. This is a 3-dimensional polar plot, shown from different perspectives: a top down view and angled side-view. From the top the elevation angles(range 0:90) are measured radially, starting at the centre and moving outwards. The azimuth angle(range0:360) are measured along the circumference of the plot. The strength of the beamformer's response, G, in the correlating elevation-azimuth direction is indicated in the z-axis direction. In both Figs. 4.10 and 4.11 the response is normalised to the number

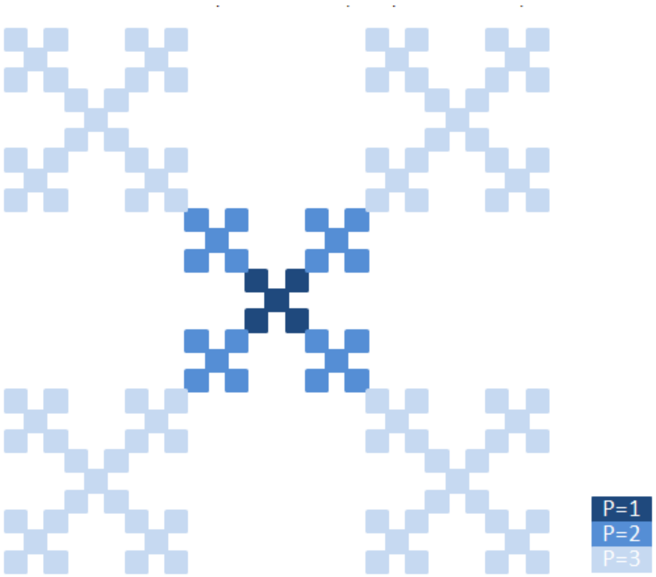

Figure 4.9: First 3-stages of growth of the Purina fractal array

of elements in the arrays, in order to offer a fair comparison of different array sizes.

The above steps have detailed the step-by-step procedure used in the design and analysis of a fractal array beamformer. Combining the antenna elements has the potential to alter the radiation characteristics of an ensemble of antennas and can result in a steerable and highly directive beam.

4.5 Simulation Results

The control method illustrated in this chapter is used to simulate a possible operative scenario in which a spacecraft formation is used to form a distributed array in Earth orbit. A geostationary orbit is chosen to simulate the dynamics although the application is not specifically aimed at telecommunications. Deployment of a fractal antenna array is simulated where the system is composed of 125 radiating elements.
The system requirements suggest suitable actuators and to a certain degree limit the choices regarding agent selection and separation. The method of control and the possibilities offered by reducing the size of individual radiating elements while maintaining an overall large aperture drive towards the selection of a satellite in the size range of pico- or nano-satellite suitable for a separation in the order of 1 m. This is the separation chosen as the inter-spacecraft distance is still small enough to control motion through mutually exchanged electromagnetic forces and far apart enough to allow for relatively coarse accuracy, in particular at the release from a carrier spacecraft or launcher.

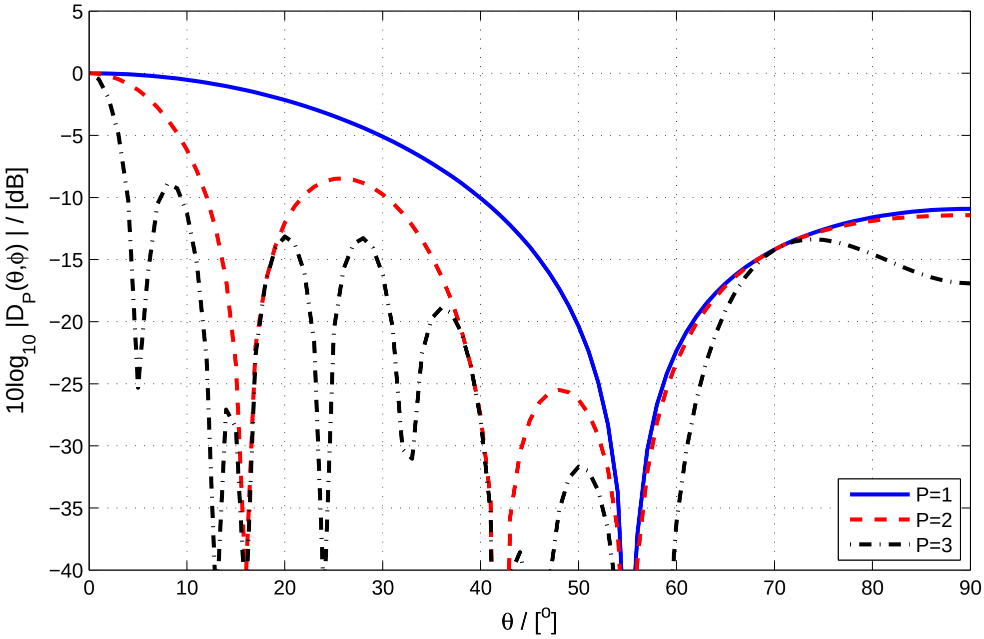

Figure 4.10: Gain response for first three growth stages of Purina fractal array; lower stages of growth form an envelope for the following stages.

In the control and operation of the beamformer some assumptions have been made, all elements are considered to be synchronised. Communication between elements has not been considered but is implicitly available. Elements are considered isotropic sources and no inter-element interference is considered. The separation of 1 m was chosen to satisfy the exercise of verifying the control method, but smaller separation distances are possible. However when designing such a beamformer for real world application a smaller separation distance is more desirable as using a distance of 1 m translates to a maximum operating frequency in the region of 150 MHz.

The 125 unitary mass agents reproduce the shape of a *Purina* fractal at a growth stage of $P = 3$; they are deployed in 25 groups of 5-agent subgroups which is the elementary unit of the formation ($N = 125$, $n = 5$). The dynamics of the spacecraft formation is based on Clohessi-Wilthshire (CW, [93]) linearised equations in an orbiting reference frame.

The reference frame forms a Cartesian coordinate system, and is arranged such that

- the x-axis is tangent to the orbit and parallel to the orbital velocity vector,
- the y-axis is parallel to angular momentum vector, and
- the z-axis is orthogonal to the first two and pointing towards the Earth's centre of gravity.

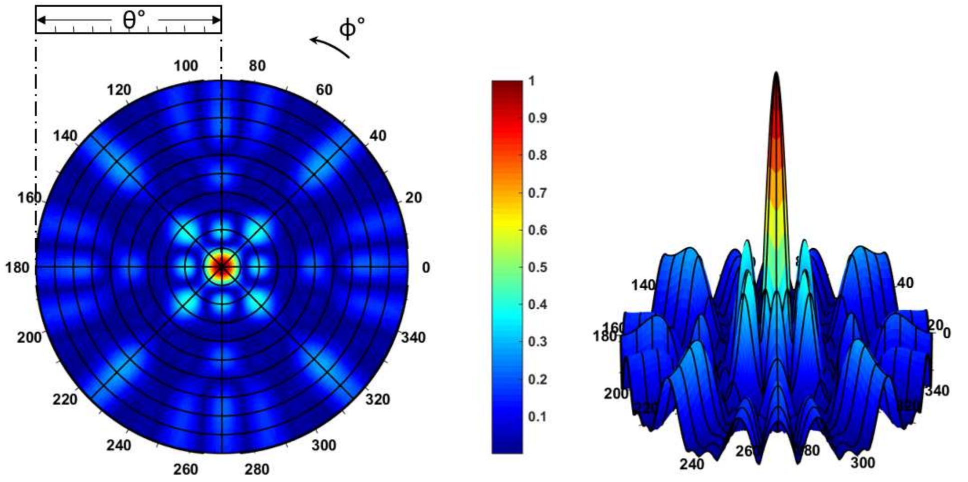

(a) Top-down profile

(b) Side profile

Figure 4.11: 3-Dimensional polar plot of beam pattern for Purina fractal at growth stage $P = 3, \Omega_0 = \pi, \varphi_0 = 0°, \vartheta_0 = 0°$.

The CW equations in this reference frame are

$$\begin{aligned} \ddot{x} &= -2\nu\dot{z} \\ \ddot{y} &= -\nu^2 y \\ \ddot{z} &= -2\nu\dot{x} - 3\nu^2 z \quad , \end{aligned} \tag{4.38}$$

where ν is the orbital frequency.

Initial conditions were set such as each spacecraft had an initial position randomly picked within a sphere centred on its final position and radius equal to 1.5 times the distance to its nearest neighbour to account for possible initial swapped positions between near agents; initial relative velocities are null. This corresponds to assuming that a carrier spacecraft or launcher releases the agents with coarse accuracy i.e. not completely randomly. Attitude for the single spacecraft is not considered while overall attitude control for rotation around the x and y axes is guaranteed by positioning control through a parabolic potential that flattens the formation onto the x–y plane. Sensors are idealised, that is, the exact position of any one agent is known without delay by all the agents to which it is linked.

Although actuators are not modelled here, some characteristics relating to the possible use of electromagnetic forces are considered. In particular, actuators of the kind proposed in [94] and [95] are considered. As these actuators, particularly those based on Coulomb forces, cannot be used concurrently due to interference issues, a duty cycle is set up and the ensemble is split into a number of groups so that any two groups which are active at the same time are relatively far apart. This allows interferences to be neglected. Each group is controlled across a time period of the duty cycle. Over the whole duty cycle each group of agents is controlled for the same amount of time. As consequence, agents belonging to more than one group — e.g. linking agents between groups — are controlled for longer. The frequency of the duty cycle needs to be high enough not to allow spacecraft to drift away between control periods. This can be bounded from below by considering a linearised version of the control law and computing the frequency of the associated harmonic oscillator. Considering the APF only, the control can be linearised about the equilibrium as

$$\begin{aligned} m\tilde{\ddot{x}}_i = \sum_j \Bigg\{ & \frac{{C^a}_{ij}}{{L^a}_{ij}} \exp\left(\frac{-d_{ij}}{{L^a}_{ij}}\right) - \frac{{C^r}_{ij}}{{L^r}_{ij}} \exp\left(\frac{-d_{ij}}{{L^r}_{ij}}\right) - \\ & \left[\frac{{C^a}_{ij}}{{{L^a}_{ij}}^2} \exp\left(\frac{-d_{ij}}{{L^a}_{ij}}\right) - \frac{{C^r}_{ij}}{{{L^r}_{ij}}^2} \exp\left(\frac{-d_{ij}}{{L^r}_{ij}}\right)\right] (x_i - d_{ij}) \Bigg\}, \end{aligned} \tag{4.39}$$

where it is assumed that the equilibrium position is at a distance d from the neighbouring agents and that these agents are fixed in their positions. The sum is extended to all the neighbouring agents acting along one axis. As an example, considering the central agent of Fig. 4.8, this means that only 2 agents contribute to its oscillatory motion along the orthogonal axes.

Since (4.39) is in the form of a linearised harmonic oscillator perturbed by a constant acceleration, the frequency associated with this system is

$$\omega_i = \sqrt{\sum_j \frac{{C^a}_{ij}}{{{L^a}_{ij}}^2} \exp\left(\frac{-d_{ij}}{{L^a}_{ij}}\right) - \frac{{C^r}_{ij}}{{{L^r}_{ij}}^2} \exp\left(\frac{-d_{ij}}{{L^r}_{ij}}\right)}. \tag{4.40}$$

Therefore, the frequency at which control is performed should not be smaller than $\sup_i \omega_i$, which is obtained by considering all the sets of values defining the control of the groups. For the case reported here, the whole duty cycle lasts 2 seconds and the 125 spacecraft are considered as belonging to 9 groups, which are

- the 5 5-agent groups at the centre of 25-agent groups,
- the 5 5-agent groups at the top of 25-agent groups,
- the 5 5-agent groups at the bottom of 25-agent groups,
- the 5 5-agent groups at the left of 25-agent groups,
- the 5 5-agent groups at the right of 25-agent groups,
- the agents linking the centres of the 5-agent groups in 25 agent group,
- the agents bonding the 5-agent side by side in the 25-agent groups,

- the agents bonding the centres of the 25-agent, and
- the agents bonding the sides of the 25-agent.

The connections between each group (consisting of 25 agents) are ensured by pairs of agents instead of groups of agents. This allows a reduction of the computational efforts for each agent and a reduction of the computational resources needed for the simulation. On the other hand this reduces the control power and slows down the deployment of the formation. Tab. 4.1 shows the values of the coefficients used.

The agent at the centre of the formation (say agent 1) is the only one linked to the centre of the reference frame by a quadratic potential in the form $U_c = \zeta|\mathbf{x_1}|^2$, with $\zeta = 0.1$ as a weighting parameter. This is to provide a kind of orbit tracking capability or, in practical terms, the possibility to stay anchored to the centre of the reference frame. This also suggests the task of tracking the orbit can potentially be carried out by a single agent only, while the others just track their relative position with respect to the central agent. Without loss of generality, for simplicity here the central agent is assumed to track the orbit. The control law is applied for just x and y axis of the orbital reference frame with control on z-axis performed through a simple parabolic potential $U_{zi} = \zeta|\mathbf{z_i}|^2$, for $i = 1 \ldots N$, that flattens the formation on the plane $z = 0$, where again $\zeta = 0.1$ is a weighting parameter. The actions of both the quadratic potentials are damped by virtual dissipative terms $\sigma\dot{\mathbf{x}}_\mathbf{i}$.

Snapshots from the deployment are shown in Fig. 4.12. It can be noted that after one day the deployment exhibits slight distortions in particular within peripheral groups.

Finally in Fig. 4.13 errors on the designed relative position after one day are plotted. The error measure is the difference between the actual distance of each spacecraft from the centre of the formation and the ideal design distance; this is then plotted as a percentage of the desired spacing. It can be seen that the maximum error is lower than 5%. The evaluations of both the snapshots in Fig. 4.12 and the error in Fig. 4.13 are considered after a maximum of 24 hours; this is sufficient to prove the self arranging capabilities of the control technique. After a further 24 hours the magnitude of the maximum error is halved as compared to the 24h values in Fig. 4.13. Theoretically a complete relaxation with no positioning errors is possible but only after an infinite period of time due to the viscous-like damping.

4.6 Discussion

The idea of meeting needs for highly directional antenna arrays through a space based fractionated architecture is constructed around the possibility of locating a number of spacecraft, each carrying an antenna element, according to a precise fractal scheme. This improves overall antenna performance and capabilities while using a contained number of elements. In turn

Table 4.1: Numerical values of coefficients used in numerical simulations.

	C^a	C^r	L^a	L^r	$L^{r\prime}$
fully connected groups (FGCs)	4	3.94722	2	1	0.5
centres of FGCs	1	0.99596	4.5	4	2
peripheral betw. adjacent FGCs	0.8925	1	2	0.5	
centres of 25-agent groups	2500	2505.3	10	9.9	4.5
peripheral of 25-agent groups	69.96	70.0	3	2.9	
$\sigma = 0.1$ for all the agents					

the possibility of using small spacecraft enables the formation of a fractionated antenna, but requires accurate spacing between the elements. Orientation is not considered here for single agents as they are assumed to be isotropic sources. Thus, in the case of an antenna array as described above, the relative agent positions within the whole array is the key requirement as this influences the performance of the array. Hence considering just coarse attitude control for single agents, a description of the system characteristics in a global sense is possible as long as relative positions are precisely known. Utilising this knowledge, directivity through array phasing is achievable at group level for compensation of global attitude errors and at agent level to accommodate misalignment of the single elements.

From a control point of view the need for precise close formation flying can be tackled through using reliable techniques and implementing these on relatively small agents. In this respect, artificial potential functions are particularly suited for the task as their stability characteristics are analytically provable, hence they do not need extensive Montecarlo test campaigns to validate their behaviour. Moreover, APFs allow for highly non-linear control through quite straightforward computation due to their smoothness. As the amount of information needed is just the relative position of a number of neighbours, the connection network presented here has the double advantage of shaping the formation on one side and reducing the number of connections on the other. These combined characteristics make small spacecraft, even with reduced computation capabilities, able to carry out the task of arranging into a formation through exclusively inter agent interaction in a decentralised way.

The artificial potential functions account for collision avoidance of the spacecraft as long as they are connected in the network, which holds for any two spacecrafts whose nominal positions are in close proximity. Two agents may then collide if they are in close proximity while they are not meant to be, hence there is not a connection between them. This is anyway avoided by choosing the initial conditions adequately, that is collocating each spacecraft within its basin of attraction with an initial velocity within the control capability of the actuators. This also accounts for the problem of local minima which are typical of APF control methods. It would be possible to account for collision of non-communicating spacecrafts by

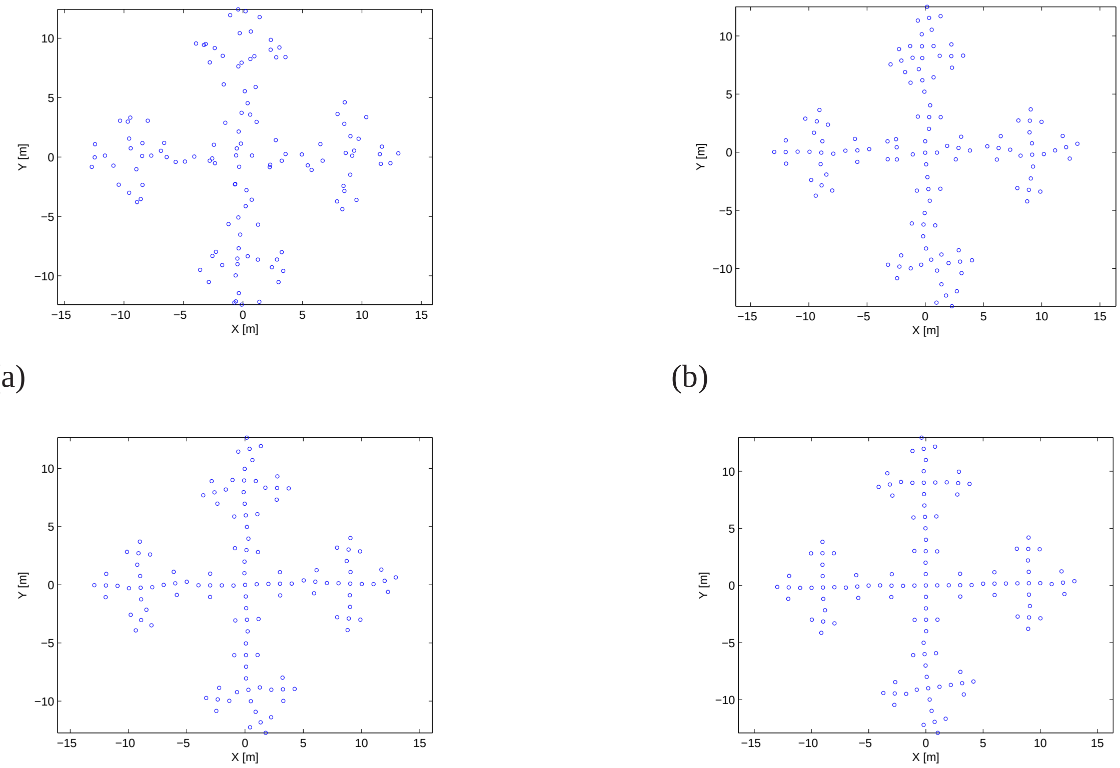

(a)

(b)

(c)

(d)

Figure 4.12: Formation deployment in GEO, with snapshots taken at (a) $t = 0$s, (b), $t = 60$s, (c), $t = 3600\text{s} = 1\text{h}$, and (d) $t = 86400\text{s} = 24\text{h}$.

triggering avoidance manoeuvres in case of closeness revealed by any sensor scanning of the local neighbours. These kinds of avoidance manoeuvres are to be designed not to introduce persistent instability in the control of the agents already linked through the network and their analysis is beyond the scope of this work.

Although the thesis is not focussed on the dynamics of the formation in the orbit environment, the definition of the simulation scenario imposes to consider specific orbit parameters and suitable actuators. Here, a geostationary orbit was considered although agents are not specifically targeted at telecommunication purposes. When dealing with actuator modelling, it was decided to keep the topic as close as possible to one of control, that is, actuator characteristics were considered only in part. Although the response of the actuators was not included, their choice took into account the close proximity scenario and the use of inter-agent electromagnetic forces was proposed rather than thrusters, which may imply plume impingement problems. Moreover the APF methods drive the system through an oscillatory stage before the achievement of the equilibrium configuration during which residual energy (both virtual potential and real kinetic) is dissipated. This translates into fuel wasting when considering the use of thrusters. The introduction of a duty cycle in the control operation is a consequence of the choice of actuators. Another advantage of having actuators that

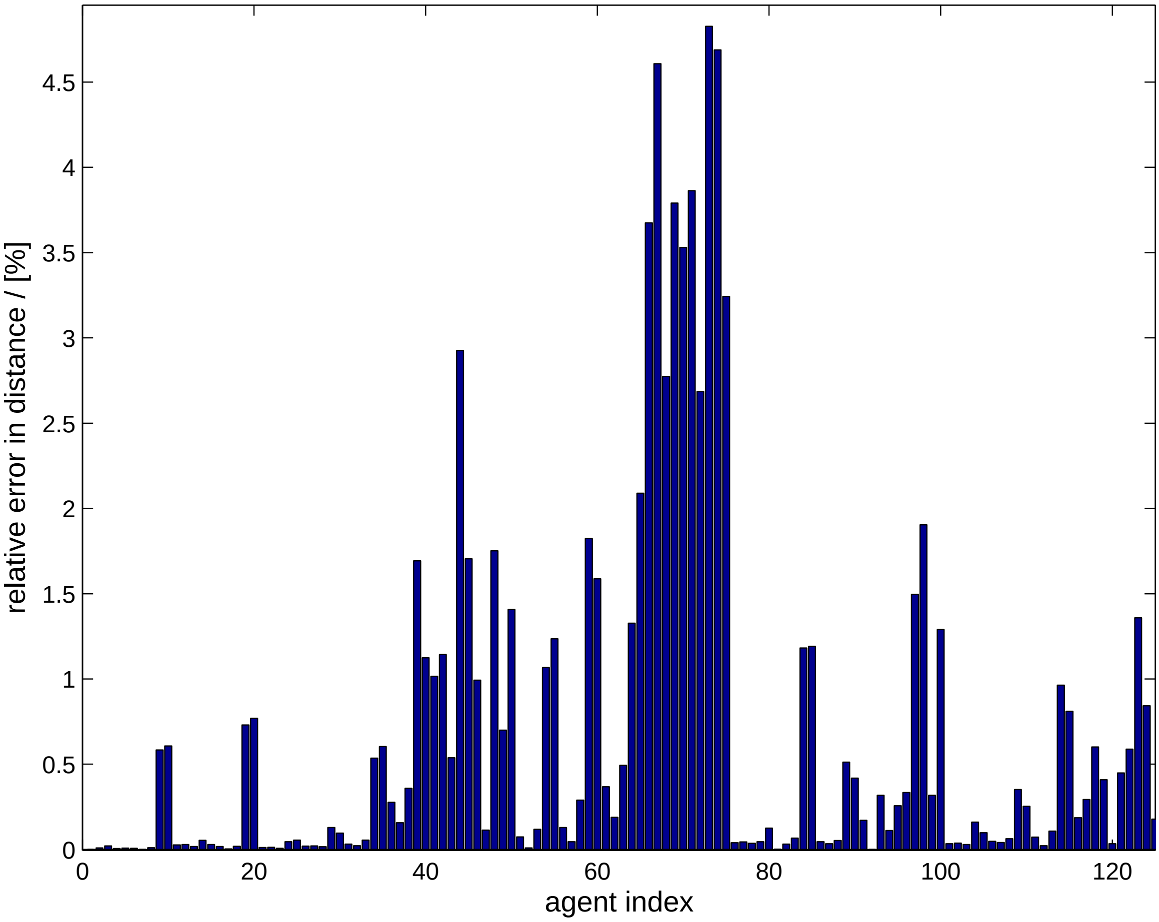

Figure 4.13: Errors in relative design positioning after 1 day from release of the formation. Distances are computed with respect to the agent at the centre of the formation, and the distance error expressed as a percentage of the ideal design distance.

mimic the virtual inter-agent action of the artificial potential makes the analysis applicable to a wider selection of possible actuators. The duty cycle just applies to inter agent actions for which Coulomb forces can be considered. Indeed in [96] and [94] it was shown how a closely spaced formation can be maintained in GEO orbit using this type of actuation. For what concerns the z-axis, the use of Lorentz forces as in [95] might be considered, although their effectiveness is to be investigated further in relation to the magnetic environment.

The communication network was intended in the first place for control purposes only, but the need for task assignment in the fractionated architecture as well as array phasing can be carried out through the same architecture. In particular, the system inherits a structured hierarchical network, where the ranking of the agents depends on the number of links they are connected to. This does not imply that the resulting architecture is centralised, but allows the task assignment to be carried out on the basis of the hierarchy of the agents. For instance the guidance for the whole formation can be carried out by a number of spacecraft which communicate in an all-to-all scheme in order to share the computational efforts (e.g. the centres of the 25 agent groups), and then passed to another module able to compare this to the navigation to eventually generate a control input for the whole formation. This is different from the guidance navigation and control functions that each spacecraft carries out: while each spacecraft should find its position in a distributed architecture, the whole system follows a guidance law that enables the mission task achievement. It is worthwhile stressing how the position of each agent is not pre-determined in a strict sense. The links of each agent are pre-assigned, but this does not prevent agents, or groups of agents belonging to the same level to swap their positions.

A final consideration about the planarity of the formation can be done. The main claim of this chapter, for what concerns the control part, is to propose a control architecture that exploits emergent behaviour shaped by the connection network. It was considered that a 2D application is sufficient to prove the main feature of the technique. Nevertheless the same considerations about the emergence of a central symmetry and the building up of several hierarchical levels in a self-similar fashion can be applied to 3D formations as well as an initiator composed of a different number of agents.

4.7 Summary

In this chapter the deployment of a self-similar formation of autonomous agents aimed at producing a fractal geometry array was for the first time investigated in the context of a space-based distributed antenna array. Artificial potential functions and self-similar adjacency matrices were used to obtain self-similar patterns in a formation of mobile agents, while electrodynamic analysis was used to assess the performance and potential benefits that arise from the fractal patterns. The formation deployment was simulated in geostationary Earth orbit, and demonstrated the feasibility of the concept.

The exploitation of emergent self-similar, or fractal, patterns in space-based beamforming arrays is encouraged by the performance for a relatively low cost and complexity, as well as by the possibility to account for positioning errors through actively controlling the phasing of the array elements. Moreover the fractal geometry of the array allows for performances in terms of directivity that are comparable, or even improved, to that of a classical square lattice scheme which makes use of a higher number of elements. However, there is a need to quantify the quality of the fractal beamformer and this is investigated in the following chapter.

The APF method enables the use of analytic tools to draw the characteristics of the control law in terms of the stability and achievement of final desired configuration. The self-similar connection scheme used accounts for multiple redundancy towards dispersion, that is any link between two agents can be lost without catastrophic consequences for the whole formation. The system is cooled-down using artificial damping which, in terms of control, represents an improvable means as the dissipation of artificial potential energy may translate into real fuel waste for the actual agents. The aim of avoiding undesirable effects due to the choice of thrusters as actuators drove towards considering electromagnetic inter-agent forces to control the formation for simulation purposes in GEO environment.

Finally, the use of multiple independent elements to form the array allows for relaxation of attitude control requirements for the single agents, shifting from an attitude problem to one of relative agent/group positioning that defines the attitude for the whole formation.

Chapter 5

Analysis of a Fractal Beamformer

5.1 Introduction

Chap. 4 demonstrated how the benefits of fractal geometries, as described by [9], can be exploited for satellite formation flying and fractionated spacecraft. This chapter analyses the impact of the Purina fractal geometry of such an array when utilised for beamforming, with a comparison to equivalent full, i.e. non-sparse, lattice arrays of comparable complexity and aperture. The beam pattern — as used in Chap. 4 — generally offers a good visualisation of the directivity of an array, but makes comparisons for 2D or 3D arrays difficult due to their dependency on azimuth, elevation and frequency. To reduce this parameter space, in this chapter a new metric termed power concentration is introduced, which assesses the power dissipated within a cone aligned with the array's look direction, i.e. an assessment how much of the radiated power will reach a specific footprint defined by a — likely small — angular spread. Using this metric the performance for beamformers of varying complexity can be compared, independent of the number of sensor elements used to form the array and across a range of frequencies. Furthermore the robustness of the array with respect to element displacement and failure is investigated.

The fractionated nature of a satellite as proposed in Chap. 4 and low-power nature of the nodes in this network motivates distributed processing when using such an array as a beamformer. We aim to mirror its fractal structure in the processing architecture, since the lack of a central processing node motivates the design of a distributed beamformer. The proposed idea demonstrates that benefits such as strictly limited local processing capability independent of the array's dimension and local calibration can be bought at the expense of a slightly increased overall cost.

5.2 Performance Analysis: Full vs Fractal Arrays

5.2.1 Array Complexity and Spatial Aperture

The aim of this chapter is to investigate sparse beamformers based on fractal formations. In particular we are interested in their performance when compared to equivalent full-lattice arrays i.e. uniform planar arrays. Fractal geometries provide a means to generate large spatial apertures using a low-number of elements, offering a reduction in the operational complexity while still providing an equivalent or better level of performance. The Purina array introduced in Chap. 4 demonstrated the general theory that there is a correlation between a beamformer's ability to focus a beam and the size of aperture formed by the array elements. In order to compare fractal to full arrays, the relationship between array complexity and spatial aperture is demonstrated here.

Some of the array parameters such as element numbers and aperture can be derived from the fractal's repetition in Eq. 4.16. Assume that the generating sub-array contains N_1 elements and that the minimum element distance is d. Note that according to Eq. 4.37 and Fig. 4.9, this minimum distance is achieved by diagonally positioned neighbours, as per Fig. 5.1. Therefore at growth scale P, the N_P elements will form a square $D_P \times D_P$ aperture with

$$N_p = N_1^P \quad , \qquad D_P = \tilde{D}_1^P \left(\frac{d}{\sqrt{2}} \right) \quad , \tag{5.1}$$

whereby for the Purina sub-array in (4.37), $N_1 = 5$ and dimension $\tilde{D}_1 = 3$. The parameters in (5.1) will directly impact on the complexity and spatial resolution of the fractal array.

To compare complexity and aperture to a full $N \times N$ lattice array, we first consider the reduction in complexity if aiming for the same aperture D_p as a Purina array at scale P. This requires $N = \frac{D_P}{d}$, yielding a relative complexity

$$C = \frac{N_P}{N^2} = \frac{N_1^P}{D_1^{2P}} = \frac{2N_1^P}{\tilde{D}_1^{2P}} = 2\left(\frac{5}{9}\right)^P \tag{5.2}$$

for the Purina fractal under the assumption of linear processing. If adaptive processing with e.g. recursive least squares-type algorithms of quadratic order in the coefficients is performed, the advantage would be further biased towards the Purina array.

Secondly, given a Purina fractal at grow scale P with aperture D_P, a full lattice array to equal its complexity N_p would occupy a $\sqrt{N_P}d \times \sqrt{N_P}d$ aperture. Therefore

$$A = \frac{D_P}{\sqrt{N_P}d} = \frac{1}{\sqrt{2}}\left(\frac{\tilde{D}_1}{\sqrt{N_1}}\right)^P = \frac{1}{\sqrt{2}}\left(\frac{3}{\sqrt{5}}\right)^P \tag{5.3}$$

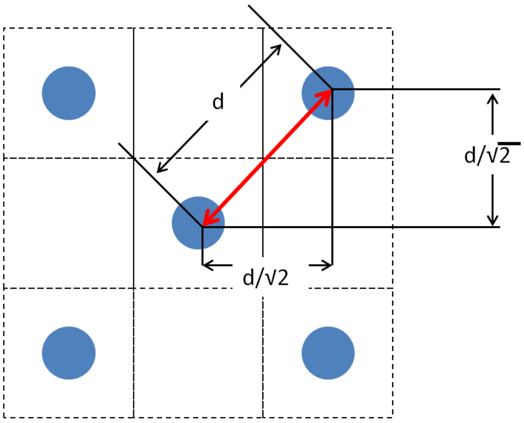

Figure 5.1: Relative spacing for the Purina array construction.

	fractal	full lattice array	
	$P = 3$	11×11	19×19
number of elements	125	121	361
aperture / d	19.07	11.00	19.00

Table 5.1: Comparison of complexity and aperture of Purina fractal ($P = 3$) with equivalent full lattice arrays.

represents the increase in aperture afforded by the Purina fractal compared to a full lattice array of equal complexity. This ratio, together with a decrease in complexity, is demonstrated in Fig. 5.2. The equivalent full lattice arrays for a Purina fractal at growth scale $P = 3$ are listed in Tab. 5.1. The comparison based on (5.2) and (5.3) suggest clear advantages for the Purina array, but omits effects such as the impact of grating lobes to the fractal array's sparse element population. Therefore, below metrics for the assessment of such arrays will be discussed, with the beam patterns to be defined in Sec. 4.3.3 leading to a new proposed metric in the following section.

5.2.2 Power Concentration as a Metric for Beam Pattern Analysis

The beamformer presented in Chap. 4 illustrated the performance characteristics/capabilities of the Purina fractal array. Beampatterns are traditionally used to describe the performance characteristics of a beamformer, usually in 2-dimensional space only i.e. reducing the set of variables by fixing either the azimuth or elevation angles. It provides a useful tool to analyse the ability of a beamformer to effectively focus energy in a particular direction. However, while the beam pattern is very descriptive its dependency on azimuth φ, elevation ϑ and normalised angular frequency Ω makes a comparison between different arrays difficult. Since the purpose of the fractal array created by our spacecraft formation is to concentrate as much of the transmitted power onto a limited footprint at the receiver, we below introduce a

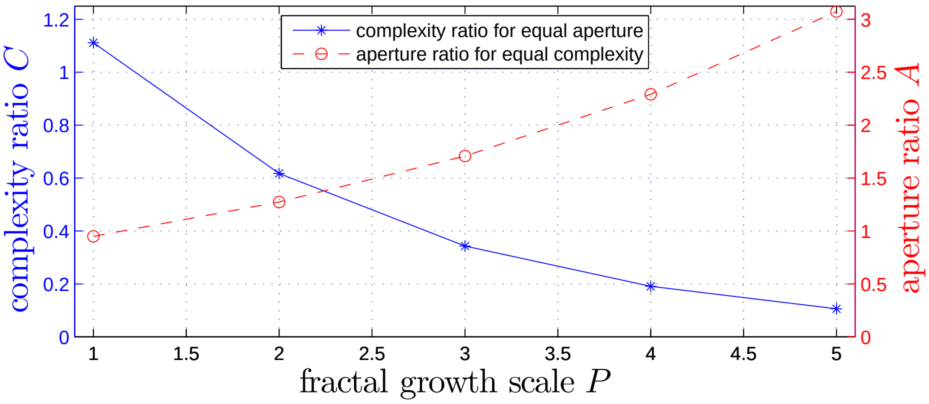

Figure 5.2: Comparison between Purina fractal array for growth scales $P = 1 \ldots 5$ and equivalent full scale lattice arrays.

metric that captures the power which an array can dissipate within a cone of opening angle α, for simplicity towards broadside as look-direction, as shown in Fig. 5.3.

The transmitted power within a cone of opening angle α is obtained by integrating the square beam pattern over the shaded area in Fig. 5.3, which is formed by a hemisphere in the far-field of the array intersecting the cone, such that

$$\psi(\alpha, \Omega) = \int_0^{2\pi} \int_0^{\alpha} |G(\vartheta, \varphi, \Omega)|^2 \sin\vartheta \; \partial\vartheta \; \partial\varphi \quad . \tag{5.4}$$

Normalising this power by the total transmit power dissipated across the hemisphere at a specific frequency Ω,$\psi(\frac{\pi}{2}, \Omega)$,

$$\rho(\alpha, \Omega) = \frac{\psi(\alpha, \Omega)}{\psi(\frac{\pi}{2}, \Omega)} \tag{5.5}$$

forms a measure $\rho(\alpha, \Omega)$, that is monotonically increasing with $\rho(0, \Omega) = 0$ and $\rho(\frac{\pi}{2}, \Omega) = 1$ akin to a cumulative density function. We hereby refer to this measure as power concentration, and the ability of an array, at a frequency Ω, to better direct energy closer to the main beam will result in a faster rising power concentration $\rho_1(\alpha, \Omega)$ that majorises the power concentration $\rho_2(\alpha, \Omega) \le \rho_1(\alpha, \Omega)$, $\forall \alpha, \Omega$ of a less directive array. For a full derivation of the power concentration metric, see App. A.

The power concentration metric defined here is used to compare a Purina fractal array at growth scale $P = 3$ with full lattice arrays of equivalent complexity and performance, as characterised in Tab. 5.1. Fig. 5.4 (a-d) show the power concentration curves at high, medium and low normalised angular frequencies $\Omega = \pi$, $\Omega = \frac{\pi}{2}$, $\Omega = \frac{\pi}{4}$ and $\Omega = \frac{\pi}{8}$ respectively. In general, with increasing array size, power concentration curves are majorised except for the fractal array, where grating lobes particularly at higher frequencies, such as $\Omega = \pi$ disturb convergence for increasing cone angles α. However, for $\Omega = \frac{\pi}{2}$ in Fig. 5.4 (b), at low angles

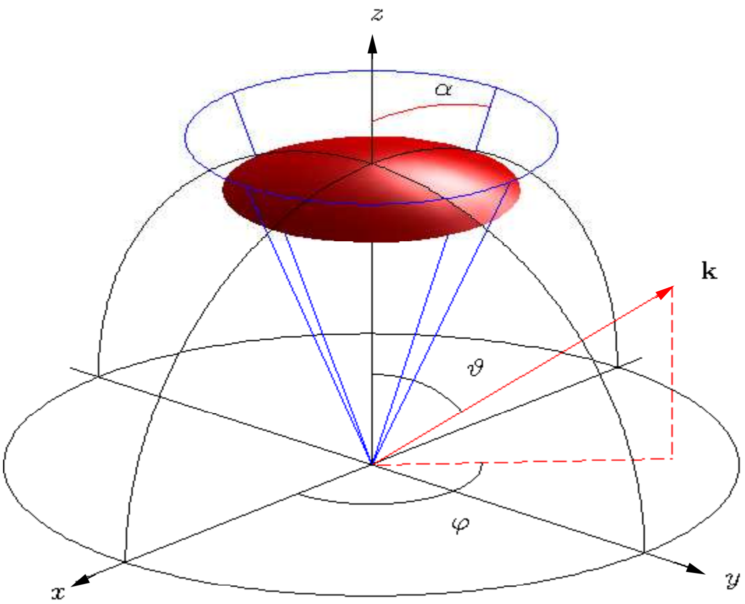

Figure 5.3: Coordinate system with a planar array located at the origin in the xy plane; the cone serves to measure the dissipated power within an elevation angle α by integrating over the shaded surface.

α — relating to a sensibly sized footprint when emitting from an orbiting fractionated space craft to ground — the power concentration of the Purina array outperforms the 11×11 array of equal complexity and performs close to a 12×12 full lattice array.
At a normalised angular frequency $\Omega = \frac{\pi}{8}$ — a fraction of $\frac{1}{16}$ of the sampling rate —, the aperture of the array becomes the dominating factor in determining spatial resolution. As evident from Fig. 5.4 (d), the Purina array performance is comparable to the 19×19 full lattice array of equal aperture, while significantly outperforming the 11×11 system. To demonstrate power concentration over the entire frequency range, we measure the power concentrated within the footprint of a cone with opening angle $\alpha = 4^\circ$. The result for variable Ω is shown in Fig. 5.5 whereby for the majority of frequencies the Purina fractal array is able to concentrate a higher proportion of its energy than a full lattice array of similar complexity. Compared to a full lattice array of equivalent spatial aperture, containing almost 3-times as many elements, the fractal array offers comparable performance in the lower frequency ranges.

Using the power concentration, a metric similar to the beam efficiency, we have shown the Purina array to offer performance advantages over equivalent full lattice arrays. The performance advantages are more pronounced towards the lower frequencies supported by the array.

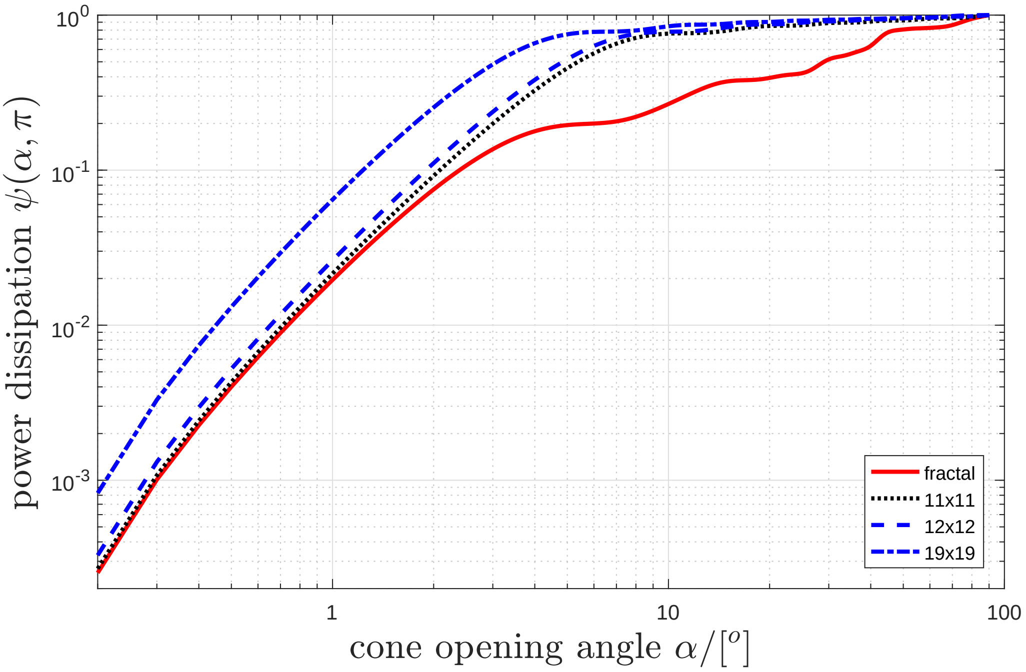

(a) $\Omega = \pi$

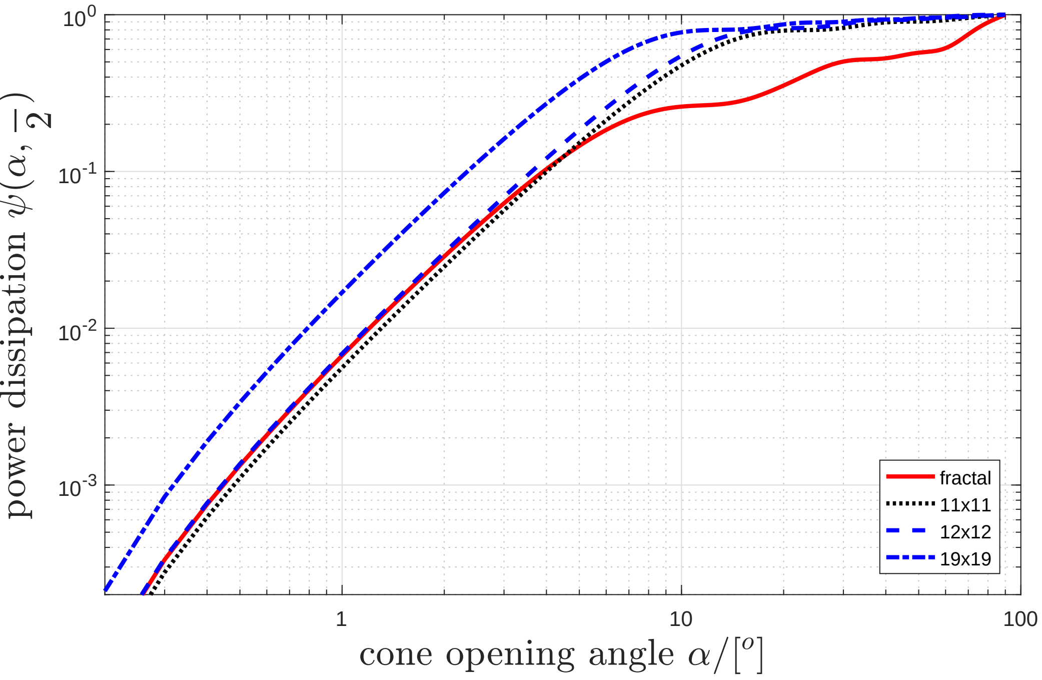

(b) $\Omega = \frac{\pi}{2}$

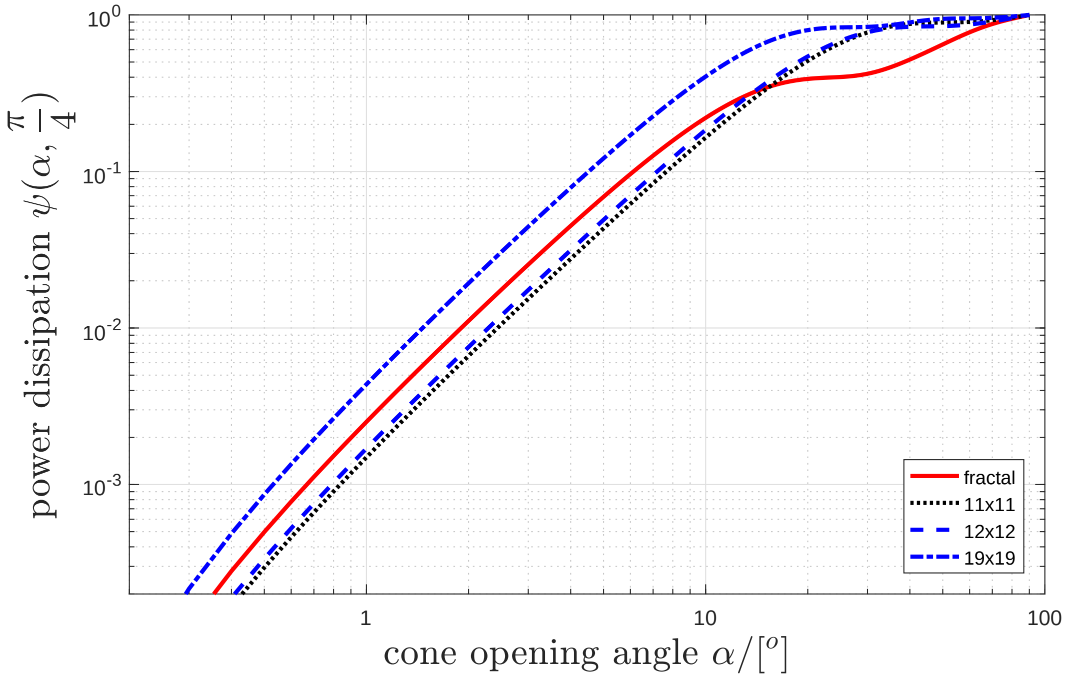

(c) $\Omega = \frac{\pi}{4}$

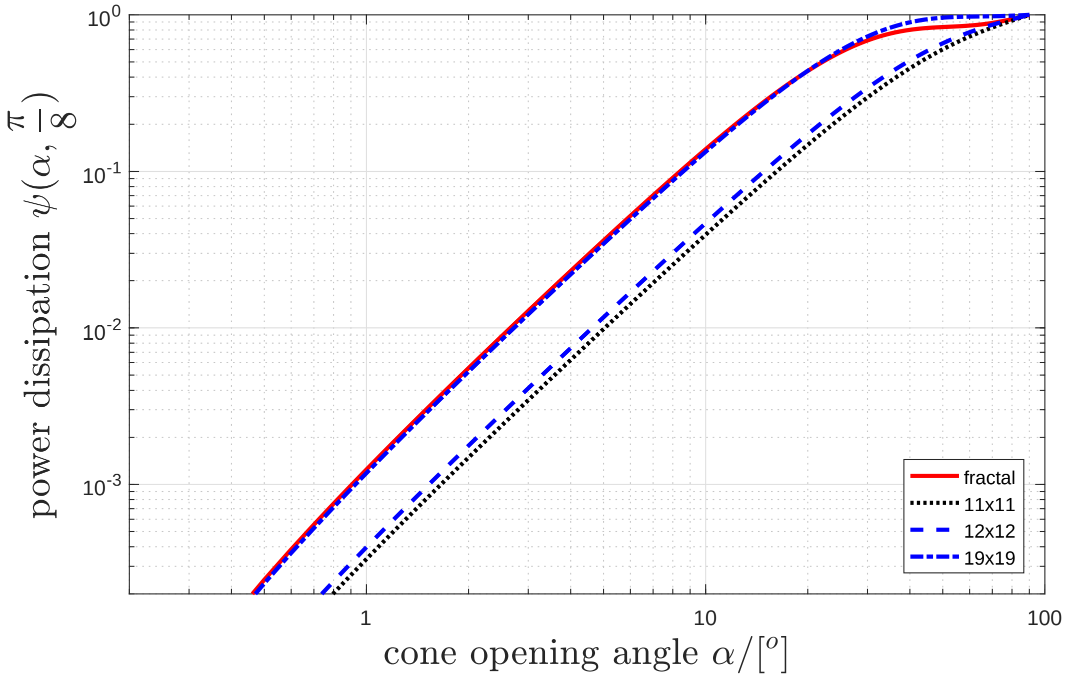

(d) $\Omega = \frac{\pi}{8}$

Figure 5.4: Power concentration curves for the Purina fractal array with $P = 3$, compared to a number of equivalent full lattice arrays of same complexity (11×11) and aperture (19×19) at a range of normalised angular frequencies $\Omega = [\pi, \frac{\pi}{2}, \frac{\pi}{4}, \frac{\pi}{8}]$.

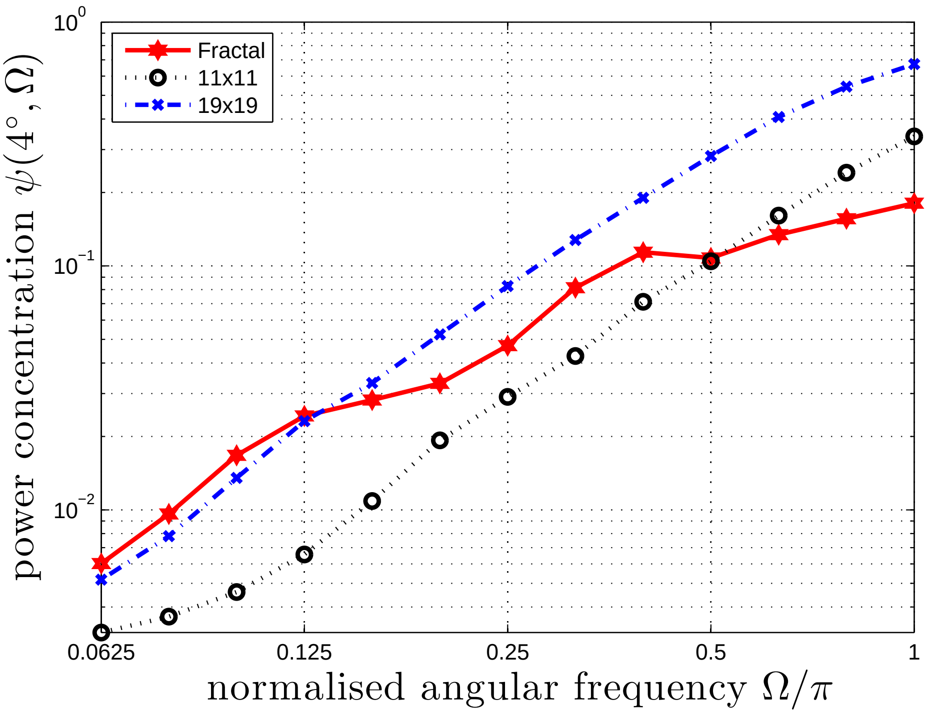

Figure 5.5: Power concentration for fixed cone opening $\alpha = 4^\circ$ and variable normalised angular frequency Ω.

5.2.3 Impact of Element Dislocation and Failures

During the deployment of the array there will be a settling in period, where the elements will be displaced from their ideal positions. This displacement error relates the position of an element w.r.t. the ideal location in terms of a percentage of the minimum inter-element spacing. Put simply, the displacement error for each spacecraft is randomly picked (using a Gaussian distribution) within a sphere centred on its ideal position and radius equal to 1.0 times the distance to its nearest neighbour. Using the power concentration metric, the array is analysed for a range of element displacements and failures.

Fig. 5.6 shows the percentage loss of total power concentration for element displacement, averaged over an ensemble of 200 random realisation. Given Fig. 5.6, the Purina fractal array appears relatively robust to displacement errors at low frequencies, and therefore maintains its performance advantage over full lattice arrays. At higher frequencies even small errors in location result in significant loss of ability to maintain the power concentration for all the array configurations tested.

Fig. 5.7 shows the percentage loss of total power concentration for node failures using a footprint defined by $\alpha = 4^\circ$, averaged over an ensemble of 200 random realisation. In terms of node failure the array performances shown in Fig. 5.7 exhibit a characteristic similar to the displacement error, with a much slower decay of performance at lower frequencies, where the Purina array possesses performance advantages anyway. The larger degradation at high

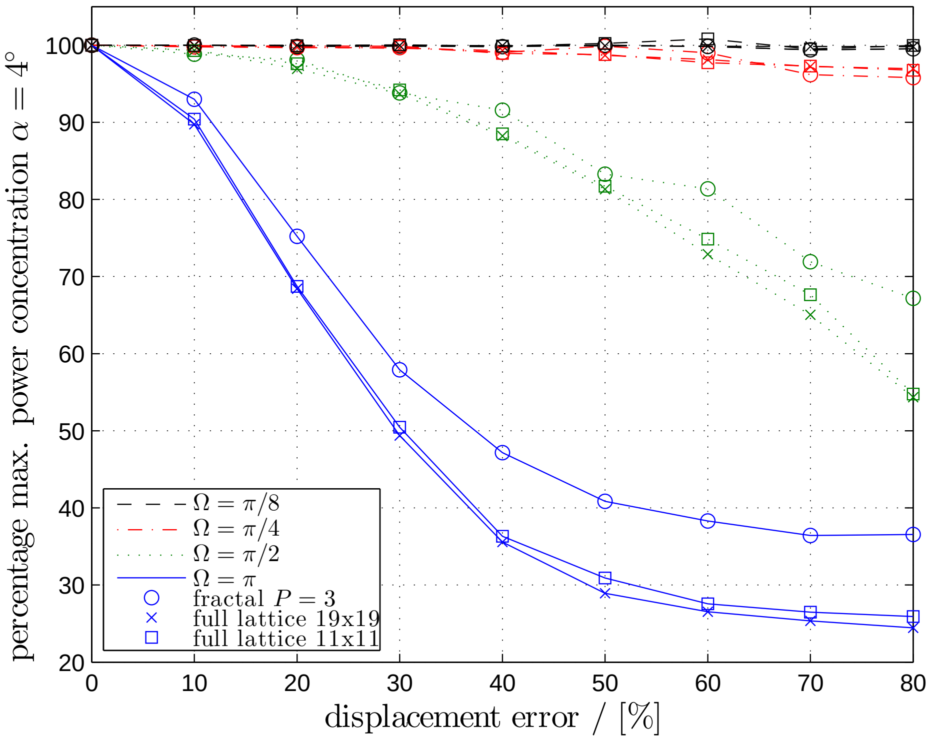

Figure 5.6: Percentage of power lost due to element positional error, averaged over an ensemble of 200 random realisations.

frequencies, where the Purina array would not be selected over the benchmarkers, therefore is of little relevance.

5.3 Control Analysis: Distributed Array Processing

In order to exploit the fractionated nature of a satellite as proposed in [91], we aim to mirror its fractal structure in the processing architecture, since the lack of a central processing node motivates the design of a distributed beamformer. In the past such efforts have e.g. concentrated on the distributed estimation of the covariance matrix [97], distributed signal enhancement with bandwidth constraints [98] or the use of factor graphs [99] and specifically Pearl's algorithm [100], which could lead to the implementation of general algorithms in a distributed fashion. Some distributed algorithms have also been developed for spatially separated subarrays [101, 102] with the main emphasis on the iterative approximation of jointly optimal results.

Our aim here is to use a hierarchical distributed processing structure which closely mirrors the fractal architecture of the array. In particular, we propose to use nested subarrays,

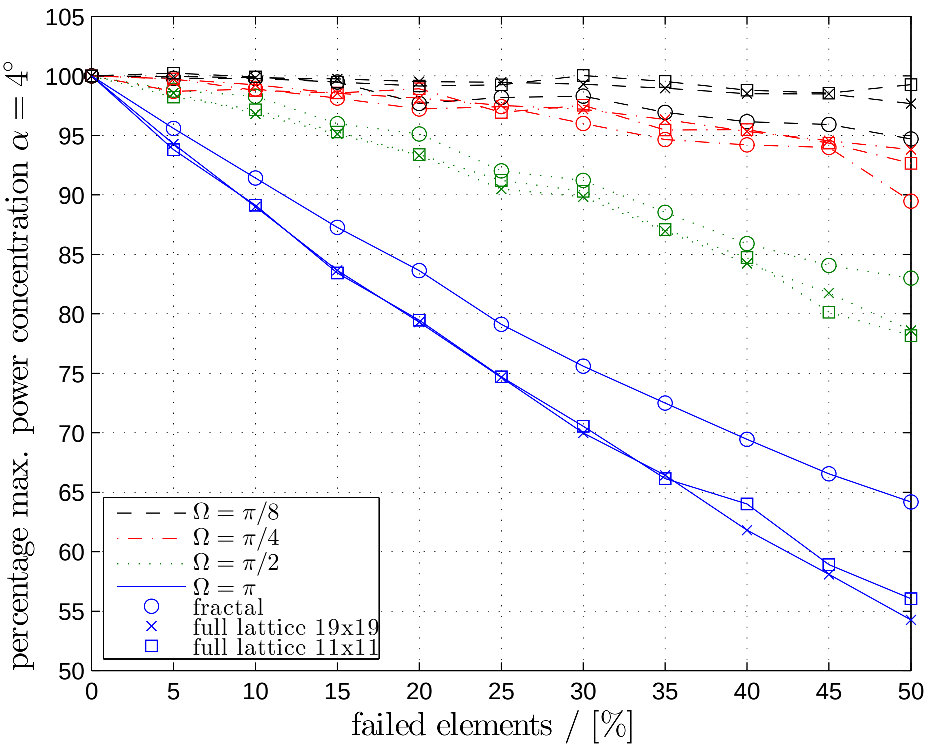

Figure 5.7: Percentage of power lost due to element failure, averaged over an ensemble of 200 random realisations.

whereby a subarray takes the shape of the generating fractal. The beamformer output can be hierarchically computed such that, independent of the dimension of the Purina array, the number of computations per node are strictly limited, even though the overall number of computations is slightly increased compared to directly processing the samples collected by all sensors.

5.3.1 Hierarchy and Labelling

For the analysis below, we will organise sensors according to their fractal scale, $p \in \mathbb{Z}$, $p \leq P$, which describes the different hierarchical layers of the architecture up to the full growth stage P. The elements at the coarsest level, $p = 1$, are given a single index, elements at fractal scale $p = 2$ a double index, and so on, until the elements at the finest scale $p = P$ are labelled using P subscripts. For the three coarsest levels of a Purina fractal array, an example is provided in Fig. 5.8. Note that in general,

$$\mathbf{r}_{k,l,\ldots,r,q,1} = \mathbf{r}_{k,l,\ldots,r,q} \quad , \tag{5.6}$$

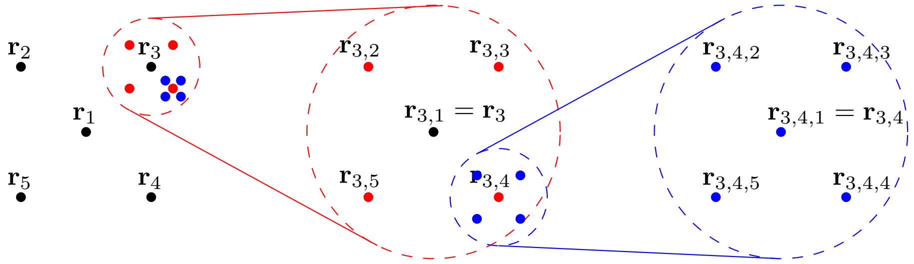

Figure 5.8: Nested labelling of array elements at fractal scale $p = 1$ with sensor locations $\mathbf{r}_k$, fractal scale $p = 2$ with locations $\mathbf{r}_{k,l}$, and fractal scale $p = 3$ with locations $\mathbf{r}_{k,l,m}$, with $k, l, m \in \{1 \dots 5\}$.

and in particular

$$\mathbf{r}_{1,1,\dots,1,1} = \mathbf{r}_{1,1,\dots,1} = \cdots = \mathbf{r}_1 \qquad . \tag{5.7}$$

Using these sensor locations, below we will be able to define a distributed beamforming system exploiting the fractal scale structure of the Purina array, by labelling the narrowband beamforming coefficient and the data sample collected at time instance n in the sensor location denoted by a vector $\mathbf{r}_{k,l,\dots,p,q}$ as $w_{k,l,\dots,p,q}$ and $x_{k,l,\dots,p,q}[n]$, respectively.

5.3.2 Distributed Beamformer

This section derives a beamformer formulation for using distributed processing of inputs based on the definition of the beamformer output in Sec. 5.3.2 and its coefficients for the quiescent case in Sec. 5.3.2. A restructuring of the equations in Sec. 5.3.2 yields a formulation with a slightly increased cost, which however allows to calibrate information that is only available within subarrays.

Beamformer Output

The overall beamformer response is given by

$$\begin{aligned} y[n] &= \mathbf{w}^{\mathrm{H}} \mathbf{x}[n] && (5.8) \\ &= \underbrace{\sum_{u_P=1}^{5} \cdots \sum_{u_2=1}^{5} \sum_{u_1=1}^{5}}_{P \quad \text{terms}} w_{u_P,\dots u_2,u_1} x_{u_P,\dots,u_2,u_1}[n] \quad , && (5.9) \end{aligned}$$

whereby $\mathbf{w}$ and $\mathbf{x}[n]$ are the stacked coefficient and data vectors at time n, and $\{\cdot\}^{\mathrm{H}}$ denotes Hermitian transpose. The computations that are required for one output sample $y[n]$ are constituted by 5^P multiply-accumulate operations, that would under normal circumstances be executed in a central processing node. Interestingly, the nesting of the summation terms in (5.9) provides a natural hierarchy in calculating the output, whereby intermediate outputs of nested subarrays are defined as

$$
\begin{aligned}
y[n] &= \sum_{u_P=1}^{5} y_{u_P}[n] && (5.10)\\
&\vdots \\
&= \sum_{u_P=1}^{5} \cdots \sum_{u_2=1}^{5} y_{u_P,\ldots,u_2}[n] && (5.11)\\
&= \sum_{u_P=1}^{5} \cdots \sum_{u_2=1}^{5} \sum_{u_1=1}^{5} y_{u_P,\ldots,u_2,u_1}[n] \quad . && (5.12)
\end{aligned}
$$

The quantities under the sum on the r.h.s. of (5.12) denote the output of subarrays at different fractal scales of the array, such that $y_P[n]$ are the outputs at the 5 nodes at the coarsest level as shown on the left side of Fig. 5.8, and outputs with an increasing number of subscripts refer to intermediate outputs at finer fractal scales.

Quiescent Beamformer Coefficients

Assuming a far field source at a narrowband frequency f which arrives at the array as a planar wave front with normal vector $\mathbf{k}$,

$$
\mathbf{k}_{\varphi,\vartheta} = \begin{bmatrix} \cos\varphi \sin\vartheta \\ \sin\varphi \sin\vartheta \\ \cos\vartheta \end{bmatrix} \quad , \tag{5.13}
$$

i.e. with azimuth φ and elevation angle ϑ, the relative time delay $\tau_{u_P,\ldots u_2,u_1}$ experienced at location $\mathbf{r}_{u_P,\ldots,u_2,u_1}$ relative to the centre element at $\mathbf{r}_1$ is given by

$$
\tau_{u_P,\ldots,u_2,u_1} = \frac{1}{c}\mathbf{k}^{\mathrm{T}}_{\varphi,\vartheta}(\mathbf{r}_{u_P,\ldots,u_2,u_1} - \mathbf{r}_1) \tag{5.14}
$$

with c denoting the propagation speed in the medium. The quantity $\mathbf{k}_{\varphi,\vartheta}/c$ is also known as the slowness vector of the source.

Given a sampling rate f_s, the narrowband source is characterised by a steering vector $\mathbf{s}_{\varphi,\vartheta}$,

$$\mathbf{s}_{\varphi,\vartheta} = \begin{bmatrix} e^{-j\Omega\tau_{1,\dots,1,1}} \\ \vdots \\ e^{-j\Omega\tau_{1,\dots,1,5}} \\ e^{-j\Omega\tau_{1,\dots,2,1}} \\ \vdots \\ e^{-j\Omega\tau_{5,\dots,5,5}} \end{bmatrix} \quad , \tag{5.15}$$

with $\Omega = 2\pi f/f_s$. For the quiescent case, (5.15) defines the optimum filter coefficients $\mathbf{w} = \mathbf{s}^*_{\varphi,\vartheta}$, i.e. the matched filter, in the mean square error sense.

Distributed Processing with Local Calibration

On the finest fractal scale, different from (5.14) we define the time shift relative to the centre of a subarray,

$$\tilde{\tau}_{u_P,\dots,u_2,u_1} = \frac{1}{c}\mathbf{k}^{\mathrm{T}}_{\varphi,\vartheta}(\mathbf{r}_{u_P,\dots,u_2,u_1} - \mathbf{r}_{u_P,\dots,u_2}) \quad . \tag{5.16}$$

Therefore, 5^{P-1} steering vectors $\tilde{\mathbf{s}}_{u_P,\dots,u_2|\varphi,\vartheta} \in \mathbb{C}^5$,

$$\tilde{\mathbf{s}}_{u_P,\dots,u_2|\varphi,\vartheta} = \begin{bmatrix} 1 \\ e^{-j\Omega\tilde{\tau}_{u_P,\dots,u_2,2}} \\ \vdots \\ e^{-j\Omega\tilde{\tau}_{u_P,\dots,u_2,5}} \end{bmatrix} \tag{5.17}$$

emerge at the finest scale. The time delays can therefore be adjusted based on local knowledge of the actual locations $\mathbf{r}_{u_P,\dots,u_2,u_1}$ within each subarray.

At the next coarser level, 5^{P-2} groups of steering vectors $\tilde{\mathbf{s}}_{u_P,\dots,u_3|\varphi,\vartheta} \in \mathbb{C}^{25}$ are assembled by weighting contributions of the sub-steering vectors in (5.17). This weighting reflects the calibation w.r.t. the time difference at this fractal scale,

$$\tilde{\mathbf{s}}_{u_P,\dots,u_3|\varphi,\vartheta} = \begin{bmatrix} \tilde{\mathbf{s}}_{u_P,\dots,u_3,1|\varphi,\vartheta} \\ e^{-j\Omega\tilde{\tau}_{u_P,\dots,u_3,2}}\,\tilde{\mathbf{s}}_{u_P,\dots,u_3,2|\varphi,\vartheta} \\ \vdots \\ e^{-j\Omega\tilde{\tau}_{u_P,\dots,u_3,5}}\,\tilde{\mathbf{s}}_{u_P,\dots,u_3,5|\varphi,\vartheta} \end{bmatrix} \quad , \tag{5.18}$$

whereby the time delays $\tilde{\tau}_{u_P,\dots,u_3,u_2}$ represent calibrations w.r.t. the central nodes of the next finer fractal scale,

$$\tilde{\tau}_{u_P,\dots,u_3,u_2} = \frac{1}{c}\mathbf{k}^{\mathrm{T}}_{\varphi,\vartheta}(\mathbf{r}_{u_P,\dots,u_3,u_2} - \mathbf{r}_{u_P,\dots,u_3}) \quad . \tag{5.19}$$

The process of (5.17) and (5.18) can be iterated until the coarsest fractal scale $p = 1$ is reached.

At the coarsest fractal scale $p = 1$, finally the complete steering vector

$$\mathbf{s}_{\varphi,\vartheta} = \begin{bmatrix} \tilde{\mathbf{s}}_{1|\varphi,\vartheta} \\ e^{-j\Omega\tilde{\tau}_2}\ \tilde{\mathbf{s}}_{2|\varphi,\vartheta} \\ \vdots \\ e^{-j\Omega\tilde{\tau}_5}\ \tilde{\mathbf{s}}_{5|\varphi,\vartheta} \end{bmatrix} \quad , \tag{5.20}$$

with

$$\tilde{\tau}_{u_p} = \frac{1}{c}\mathbf{k}^{\mathrm{T}}_{\varphi,\vartheta}(\mathbf{r}_{u_P} - \mathbf{r}_1) \tag{5.21}$$

is obtained, which matches the original steering vector $\mathbf{s}_{\varphi,\vartheta} \in \mathbb{C}^{5^P}$ in (5.15).

The computational structure in calculating the output (5.12) can be performed to match the nested iterative structure of steering vectors presented by (5.17), (5.18) and (5.20). At the finest scale, outputs $\tilde{y}_{u_P,\ldots,u_3,u_2}[n]$ are determined as

$$\tilde{y}_{u_P,\ldots,u_3,u_2}[n] = \sum_{u_1=1}^{5} \tilde{w}_{u_P,\ldots,u_2,u_1} \cdot x_{u_P,\ldots,u_2,u_1}[n] \quad , \tag{5.22}$$

with the coefficients $\tilde{w}_{u_P,\ldots,u_2,u_1}$ matched to the modified steering vectors $\tilde{\mathbf{s}}_{u_P,\ldots,u_2|\varphi,\vartheta}$ in (5.17). From this finest level upwards, at each fractal scale phase corrections as in (5.18) and (5.20) are applied when adding up outputs in a divide-and-conquer fashion to finally reach $y[n]$ at the coarsest fractal scale.

5.3.3 Discussion, Simulations and Results

Computational Complexity

The complexity of the direct formulation in (5.9) via a scalar product requires $C = 5^P$ multiply-accumulates, which might need to be afforded in a central processing node, where data, weights, and any calibration for displaced sensors might be required. For the proposed computational structure in Sec. 5.3.2, the hierachical processing structure requires a total of

$$\tilde{C} = \sum_{p=1}^{P} 5^p > C \quad . \tag{5.23}$$

However, for sufficiently large P, the relative difference between $\tilde{C}$ and C diminishes as shown in Fig. 5.9, since both approaches possess a complexity of order $\mathcal{O}(5^P)$. However, for

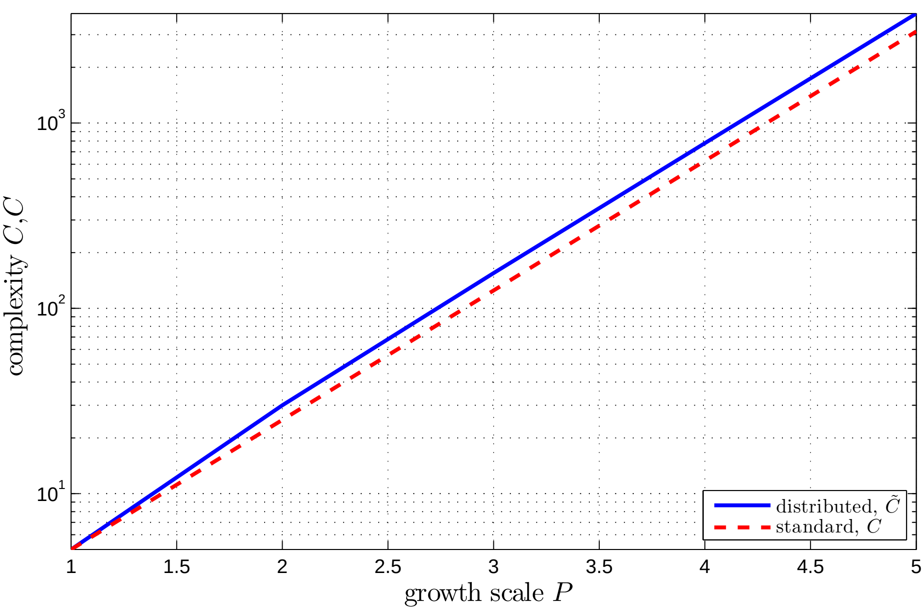

Figure 5.9: Complexity for standard (C) and distributed processing ($\tilde{C}$) as a function of the growth stage P.

the distributed approach, the requirement of not more than 5 multiply-accumulate operations per sensor node — independent of P — emerges as a major benefit. Also, the distributed structure is easier to calibrate, as dislocations of sensors only have to be known at the local subarray level, which matches the control strategy for flying a Purina array in formation, as outlined in [92].

Beampatterns

A number of sample beampatterns for the Purina array beamformer are shown in Figs. 5.10 and 5.11. These beampatterns emerge from a beamformer $D_P(\vartheta, \varphi)$ matched to receive a signal from broadside, $\vartheta = 0°$, and are calculated by probing the array with a set of steering vectors $\mathrm{s}_{\varphi,\vartheta}$ as defined in (5.15) for variable elevation ϑ,

$$D_P(\vartheta, \varphi) = \mathbf{w}^{\mathrm{H}}\mathbf{s}_{\varphi,\vartheta} \qquad . \tag{5.24}$$

The azimuth is in this case set to zero, $\varphi = 0°$. Since for every value of P, the minimum distance between array elements is set to fulfil correct spatial sampling, no aliasing occurs, and an increase in P corresponds to an increase in resolution as characterised by the narrowing beamwidth at $\vartheta = 0°$, and lower sidelobe levels. Note that the fractal structure of the array results in "inscribed" or majorised beampatterns where $|D_{P+1}(\vartheta, \varphi)| < |D_P(\vartheta, \varphi)| \forall \vartheta, \varphi, P$.

For illustration purposes, Figs. 5.12 and 5.13 show a Purina array with element distances adjusted to satisfy correct spatial sampling for the case $P = 4$, with the beam pattern matching the one showns in Figs 5.10 and 5.11. If only coarser fractal scales $p < P$ are processed, subarrays are spatially subsampled and spatial aliasing can be noticed. Interestingly, again the fractal structure of the array results in majorised beampatterns.

5.4 Summary

The Purina fractal array, based on its use as a formation for a fractionated spacecraft, has been utilised in this chapter as a beamformer, which we have compared in terms of complexity and aperture to full lattice array beamformers with comparable system parameters. To better assess the array's ability to concentrate transmit power within a cone, power concentration has been introduced as a metric, which can be derived from the array's beam pattern. The dependency on azimuth and elevation is thereby compressed into a single variable. The analysis performed with this metric indicates that, compared to full lattice arrays, the fractal geometry has very distinct advantages if energy has to be concentrated within a small angular spread, particularly at lower frequencies. It has been shown that this advantage can be maintained in the case of element displacement and element failures.

Further, we have considered distributed processing for a Purina fractal array, which emerges from a generating subarray to reach a growth stage P over a number of fractal scales $p = 1 \ldots P$. The considered processing consisted of the calculation of a beamformer output, which can exploit the fractal structure to define the distributed processing architecture. As a simple example, we have assumed a quiescent beamformer, which is optimal in a scenario where a single source is embedded in isotropic noise.

The advantages of the discussed processing architecture lie in the fixed maximum complexity per node in the distributed procedure. In addition to limiting the processing power, transmit power is conserved through short hops. Further, the distributed approach matches the position control strategy of the Purina array for formation flying, and allows to consider calibration information in the form of locally known dislocation of sensor elements when computing the beamformer output.

The next chapter will expand on the aspects not given full coverage in this doctoral investigation. These include methods to further improve the fractal beamformer's performance across a wider range of frequencies. In addition what further work can be looked at to leverage the distributed array as demonstrated in this chapter.

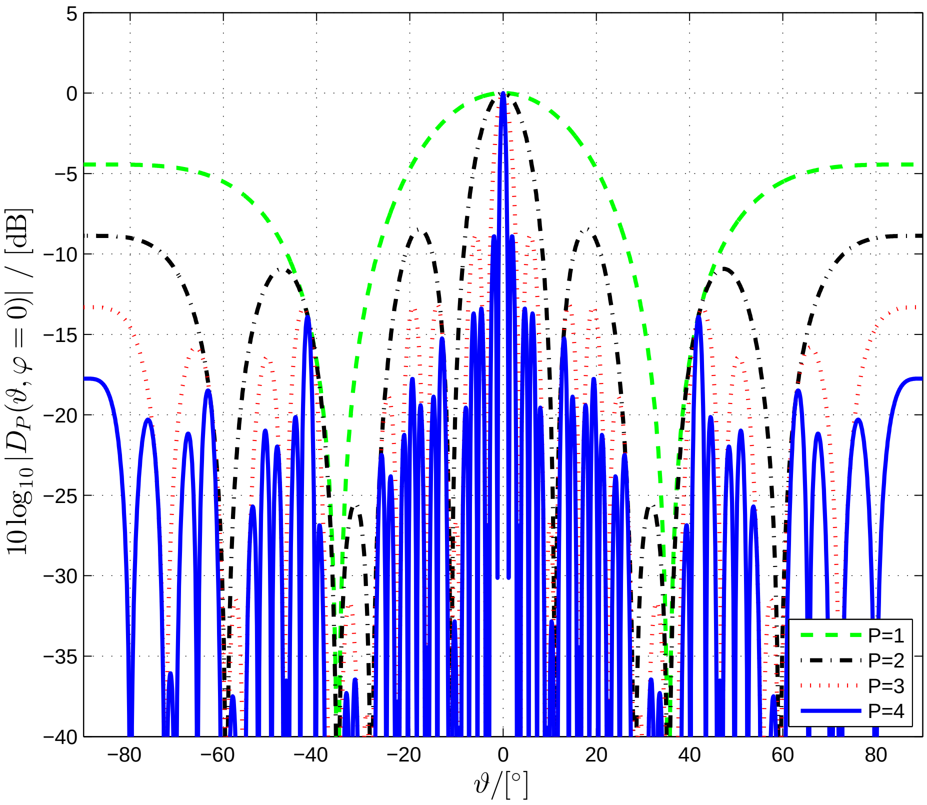

Figure 5.10: Quiescent beampatterns of Purina array for different growth stages $P = 1$, 2, 3 and 4, assuming that in each case the array elements' minimum spacing satisfies spatial sampling.

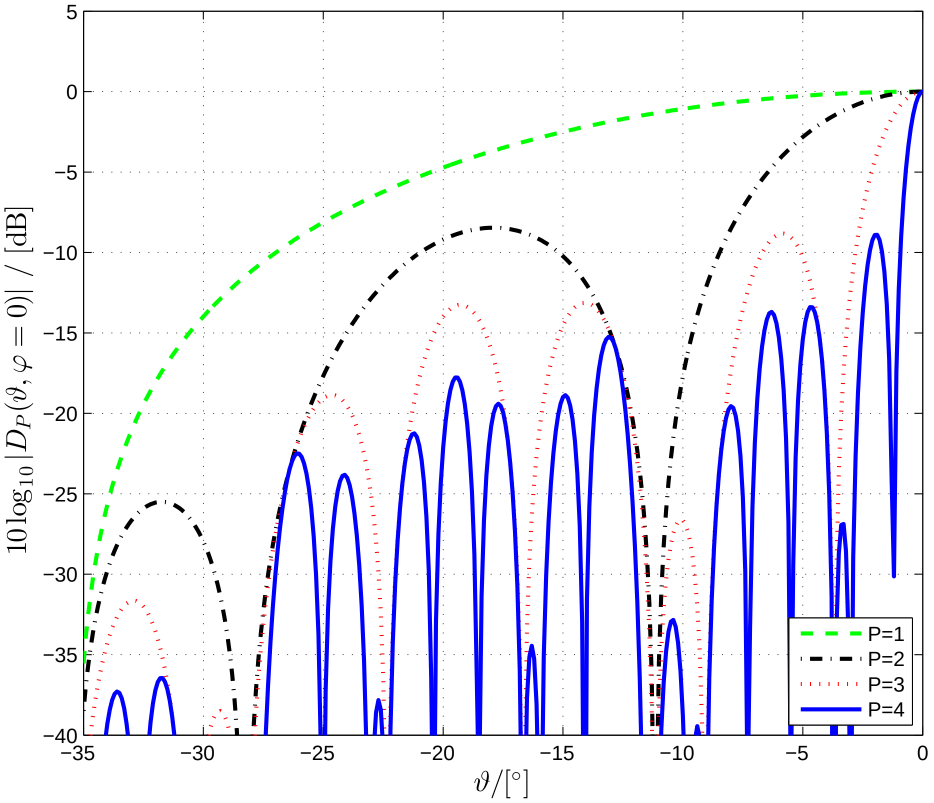

Figure 5.11: Detail view of Fig. 5.10, showing the main beam for $P = 1$ and the iterative inscribed characteristics for finer fractal scaled Purina fractal arrays.

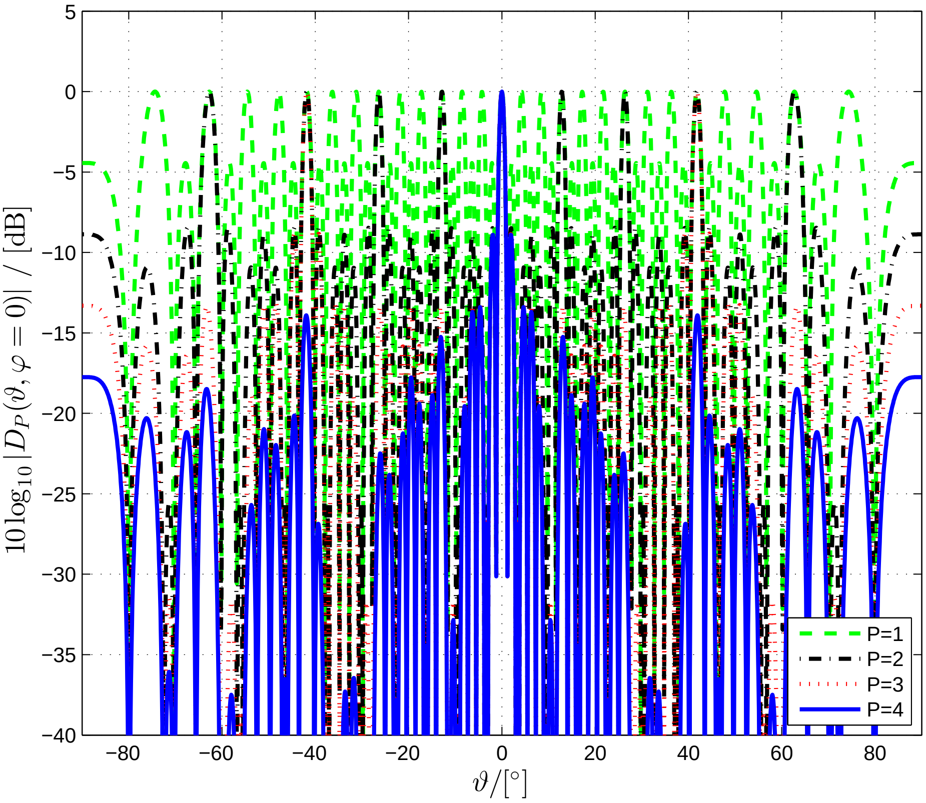

Figure 5.12: Quiescent beampatterns of Purina array adjusted to sample correctly with growth stage $P = 4$, while processing of finer fractal scales for $p = 1$, 2, and 3 operate on a subsampled array.

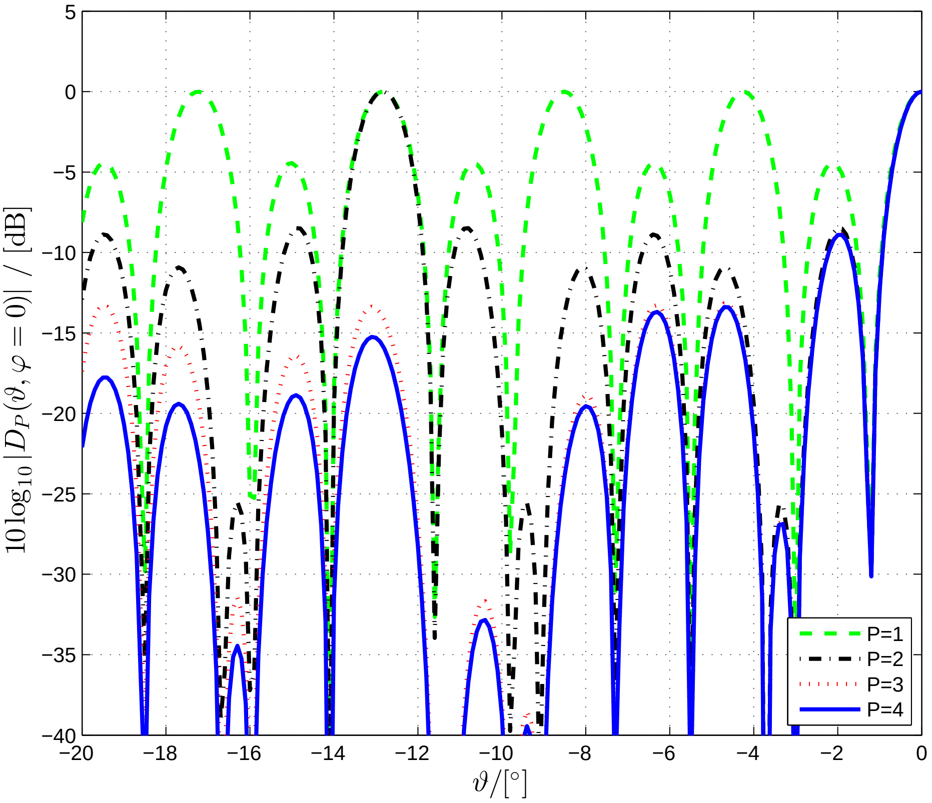

Figure 5.13: Detail view of Fig. 5.12, showing the main beam for $P = 4$ and the iterative inscribed characteristics for coarser fractal scales of the Purina arrays.

Chapter 6

Conclusions and Future Work

This thesis investigated the design of a mission interface computer, and the application of CubeSats within a fractionated fractal beamformer. Below, the findings of this thesis are summarised in Sec. 6.1, leading to starting points for future research in Sec. 6.2.

6.1 Conclusions

The role of CubeSats in the exploitation of space is beginning to rival that of small-to-medium size satellites. Chap. 2 provided a general introduction to CubeSats and associated technologies. Although much smaller than traditional satellites, they follow a very similar design and development path. They are fast becoming a respected platform for performing space science and the on-board control functionality — provided by the on-board processing — is a key component of their success.

Initially the increase in popularity was a result of the low-cost and short development cycles representative of these nano-satellites. However, more recently, it has been found that although they are small, innovative use of the available resources can produce very valuable results. The ambition of some missions coupled with multiple payloads and the fact more sophisticated platform units are becoming commonplace means that a highly-reliable, low-power, low-cost yet capable on-board computing capability is essential.

When designing for space a number of environmental challenges imposed by the spacecraft's remoteness from Earth pose some interesting design challenges. Chap. 2 showed how traditional efforts to overcome these challenges have utilised expensive techniques and bespoke technology. Often larger satellites use a fully redundant, complex system to manage the operation of the satellite [103]. This level of reliability comes at the expense of added complexity and processing requirements. This approach deviates from the off-the-shelf nature and low-cost philosophy of CubeSats.

The Mission Interface Computer presented in Chap. 3 demonstrated the same outcomes can be achieved through clever component selection and design techniques. The MIC represents the next generation in processing capabilities for CubeSats as it combines the high-speed processing capabilities of an FPGA with robust and error handling design features achieved through intelligent component selection, error protected memory, glue logic and clock mitigation techniques. The methodology used in the design of the MIC has produced a scaled down version of the safety critical design elements, but has done so utilising a low-power, scalable solution implemented using a combination of FPGA and Commercial Off The Shelf (COTS) components. The design of the MIC brings large-satellite processing performance to this small, power-constrained platform.

The UK Space Agency's first ever CubeSat mission was UKube-1 and represented an exciting and novel collaboration between the UK Space Agency, industry and academia. The successful launch and operation of the UKube-1 CubeSat mission [71] included the maiden flight of the MIC. Launched on the 8th of July 2014, the CubeSat successfully completed its operational goals and the mission officially ended on 8th August 2015. The management and operation of the satellite have been handed over to AMSAT, who continue to use their FUNCUBE payload within the the satellite in their educational outreach program. UKube-2 is being prepared for launch in 2018 with many of the lessons and successes of UKube-1 influencing the design. The FLASH SoC/FPGA-based design of the MIC has influenced future on-board computer design. Clyde-Space the main contractor in the UKube programme have developed their own on-board computer, centred around a FLASH based FPGA.

The ability of CubeSats to perform increasingly complex processing is a key step towards the realisation of CubeSat constellations. There is currently wide spread interest in the notion of fractionalised spacecraft, where the functional and operational aspects of a large satellite are spread across a network of smaller satellites. The use of low-cost CubeSats in the context of satellite networks appears favourable due to their small size, relatively low launch cost, short development cycle and utilisation of commercial off the shelf components. However, the task of communicating between satellites in low Earth orbit is not a trivial one, and is further exacerbated by low-power and processing constraints in CubeSats. Technology enablers such as the MIC, offering next generation performance, open up the possibility of formation flying and the application to space-based distributed antenna arrays.

Chap. 4 introduced fractals and exploited their self-similarity for the deployment of a distributed antenna array. The Purina fractal chosen offers a promising compromise of low-complexity control and high performance antenna pointing. The grouping of a number of independent antenna elements into a cooperative structure was achieved by coupling reliable formation flying capabilities with the possibility of producing complex fractal patterns using spacecraft. The notion of exploiting such a distributed fractal antenna was shown to offer a promising compromise of low-complexity control and high performance antenna pointing.

Chap.5 further explored the Purina fractal beamformer by comparing it in terms of complexity and aperture to full lattice array beamformers with comparable system parameters. Calculations show how such an architecture surpassed in performance both large monolithic antennas and distributed, regularly spaced array lattices. To better assess the array's ability to concentrate transmit power within a cone, power concentration was introduced as a metric, which can be derived from the array's beam pattern. The analysis performed with this metric indicated that, compared to full lattice arrays, the fractal geometry has very distinct advantages if energy has to be concentrated within a small angular spread, particularly at lower frequencies. It has been shown that this advantage can be maintained in the case of element displacement and element failures.

Further, Chap.5 investigated the notion of distributing the beamforming processing in a similar fashion to the control methods described in Chap. 4. The possibility of distributed beamforming based on local processing within smaller groups of the fractal shape, lends itself well to the self-similarity possessed by the fractal. The advantages of the discussed processing architecture lie in the fixed maximum complexity per node in the distributed procedure. In addition to limiting the processing power, transmit power is conserved through short hops. Further, the distributed approach matches the position control strategy of the Purina array for formation flying, and allows to consider calibration information in the form of locally known dislocation of sensor elements when computing the beamformer output.

6.2 Future Work

A number of key elements can be identified from the work presented each with their own future paths.

The performance of the MIC in space and how this related to the original design provides a number of opportunities to gain a deeper understanding into the electronic devices in space as well as the design practices adopted during the development of the MIC. A full analysis of the radiation and electronic device degradation characteristics would provide valuable information which can then be fed back into the UKube program for future missions.

Only the merits and performance characteristics of the Purina array were investigated. A comparison to other fractal arrays would provide a more complete assessment of this fractal array and its performance relative to equivalent full lattice arrays.

The limitations of the Purina fractal array when used as a beamformer relate to its poor performance at higher frequencies. Three potential methods for future investigation have been identified: grating lobe reduction through iterative techniques, 2D smoothing using a Dolph-Chebyshev approximation and an array shifting methods that lends itself well to the distributed nature of the control system.

Further investigations into distributed fractal beamformers could include using adaptive techniques for interference suppression/nulling with distributed beamforming [104, 105]. This approach could be used to switch off some of the nodes, thus relaxing the inter-element communication burden and further reducing the overall system complexity.

There are some assumptions made within this work which when removed provide interesting problems to be resolved.

- There has been the implicit understanding that inter-satellite communications is available and functions perfectly. The communication between satellites entails considerable technical challenges, ranging from the protocol used, to the antenna and pointing capabilities of each satellite. Power is a concern, as is the implementation of the inter-communications subsystem.
- Isotropic sensitivity and radiation patterns for antennas have been used throughout the discussions and analysis of the fractal beamformer. What could be learned from applying specific antenna types, especially those designed for CubeSats?

The actuators and control method discussed here to achieve and maintain the fractal formation relies on the use of actuators and inter-satellite communication methods. The actuators used to control the antenna formation could present a form of interference. This offers the opportunity to study the relationship between the actuators used for overall system control and how they affect the communication aspect and antenna pointing.

The above starting points for further research would further enhance the hardware and algorithmic components that have been designed for CubeSats as part of this thesis with the view to create fractionated, distributed spacecraft.

Appendix A

Power Concentration Derivation

A.1 Introduction

Beam patterns as discussed in Chaps. 4 & 5 offer insight into the gain of a beamformer measured with respect to different directions. For two- and three-dimensional arrays, beampatterns provide a good visualisation but are not easy when comparing different designs. Therefore, power concentration is proposed as a measure, which calculates the far-field dissipated power in dependency on the angle of a cone a whose axis is aligned with the array's look direction.

A.2 Proposed Measure

We seek a measure that defines the ratio of far field power dissipated inside a cone of angle α to the total dissipated power. The faster this curve approaches unity, the better the array concentrates transmit power. This measure is similar to a cumulative density function.

Given the beam pattern $G(\vartheta, \varphi)$, we define a function

$$P(\alpha) = \int_0^{2\pi} \int_0^{\alpha} |G(\vartheta, \varphi)|^2 \sin\vartheta \; \partial\vartheta \; \partial\varphi \quad ,$$

which calculates the quadratic gain within a cone of angle α. Subsequently, power concentration can be defined as

$$p(\alpha) = \frac{P(\alpha)}{P(\frac{\pi}{2})} \quad .$$

This specific measure is defined for a planar array, and only considers one hemisphere. Due to symmetry between front and back of a planar array, the second hemisphere is omitted. For a 3-dimensional array, the normalisation should occur w.r.t. the total dissipated power in all directions.

A.3 Derivation

A.3.1 Main Approximation

In a discrete approximation, the beam pattern is only measured at discrete angles ϑ_i and φ_j, $i = 1 \ldots I$ and $j = 1 \ldots J$. For simplicity, we assume that the beam pattern is sampled uniformly at equidistant angles $\Delta\vartheta = \vartheta_i - \vartheta_{i-1}$, with $\vartheta_1 = 0$ and $\vartheta_I = \frac{\pi}{2}$. Similarly, $\Delta\varphi = \varphi_j - \varphi_{j-1}$ with $\varphi_1 = 0$ and $\varphi_J = 2\pi - \Delta\varphi$. Therefore:

- $0 \leq \alpha \leq \frac{\Delta\vartheta}{2}$:

$$P(\alpha) \approx \sum_{j=1}^{J} |G[0,\varphi_j]|^2 \int\limits_{\varphi_j-\frac{\Delta\varphi}{2}}^{\varphi_j+\frac{\Delta\varphi}{2}} \int\limits_{0}^{\alpha} \sin\vartheta \, \partial\vartheta \, \partial\varphi \tag{A.1}$$

- $\frac{\Delta\vartheta}{2} < \alpha \leq \frac{\pi}{2} - \frac{\Delta\vartheta}{2}$, with $\hat{I} = \text{round}\{\frac{\alpha}{\Delta\vartheta}\}$

$$\begin{aligned} P(\alpha) \quad \approx \quad & \sum_{j=1}^{J} |G[0,\varphi_j]|^2 \int\limits_{\varphi_j-\frac{\Delta\varphi}{2}}^{\varphi_j+\frac{\Delta\varphi}{2}} \int\limits_{0}^{\frac{\Delta\vartheta}{2}} \sin\vartheta \, \partial\vartheta \, \partial\varphi \quad + \qquad (\text{A.2}) \\ + \quad & \sum_{i=2}^{\hat{I}} \sum_{j=1}^{J} |G[\vartheta_i,\varphi_j]|^2 \int\limits_{\varphi_j-\frac{\Delta\varphi}{2}}^{\varphi_j+\frac{\Delta\varphi}{2}} \int\limits_{\vartheta_i-\frac{\Delta\vartheta}{2}}^{\vartheta_i+\frac{\Delta\vartheta}{2}} \sin\vartheta \, \partial\vartheta \, \partial\varphi \quad + \qquad (\text{A.3}) \\ + \quad & \sum_{j=1}^{J} |G[\vartheta_{\hat{I}+1},\varphi_j]|^2 \int\limits_{\varphi_j-\frac{\Delta\varphi}{2}}^{\varphi_j+\frac{\Delta\varphi}{2}} \int\limits_{\vartheta_{\hat{I}}-\frac{\Delta\vartheta}{2}}^{\alpha} \sin\vartheta \, \partial\vartheta \, \partial\varphi \qquad (\text{A.4}) \end{aligned}$$

- $\frac{\pi}{2} - \frac{\Delta\vartheta}{2} < \alpha \leq \frac{\pi}{2}$:

$$P(\alpha) \approx \sum_{j=1}^{J} |G[0,\varphi_j]|^2 \int\limits_{\varphi_j-\frac{\Delta\varphi}{2}}^{\varphi_j+\frac{\Delta\varphi}{2}} \int\limits_{0}^{\frac{\Delta\vartheta}{2}} \sin\vartheta\;\partial\vartheta\;\partial\varphi \quad + \tag{A.5}$$

$$+ \sum_{i=2}^{I-1}\sum_{j=1}^{J} |G[\vartheta_i,\varphi_j]|^2 \int\limits_{\varphi_j-\frac{\Delta\varphi}{2}}^{\varphi_j+\frac{\Delta\varphi}{2}} \int\limits_{\vartheta_i-\frac{\Delta\vartheta}{2}}^{\vartheta_i+\frac{\Delta\vartheta}{2}} \sin\vartheta\;\partial\vartheta\;\partial\varphi \quad + \tag{A.6}$$

$$+ \sum_{j=1}^{J} |G[\frac{\pi}{2},\varphi_j]|^2 \int\limits_{\varphi_j-\frac{\Delta\varphi}{2}}^{\varphi_j+\frac{\Delta\varphi}{2}} \int\limits_{\frac{\pi}{2}-\frac{\Delta\vartheta}{2}}^{\alpha} \sin\vartheta\;\partial\vartheta\;\partial\varphi \tag{A.7}$$

Due to interval changes, the integration at the pole and equator need to be performed separately.

A.3.2 Calculations

Main Integration

For the main integration, we obtain

$$\int\limits_{\varphi_j-\frac{\Delta\varphi}{2}}^{\varphi_j+\frac{\Delta\varphi}{2}} \int\limits_{\vartheta_i-\frac{\Delta\vartheta}{2}}^{\vartheta_i+\frac{\Delta\vartheta}{2}} \sin\vartheta\;\partial\vartheta\;\partial\varphi = [-\cos\vartheta]_{\vartheta_i+\frac{\Delta\vartheta}{2}}^{\vartheta_i-\frac{\Delta\vartheta}{2}}\;[\varphi]_{\varphi_j+\frac{\Delta\varphi}{2}}^{\varphi_j-\frac{\Delta\varphi}{2}} \tag{A.8}$$

$$= \left\{\cos(\vartheta_i - \frac{\Delta\vartheta}{2}) - \cos(\vartheta_i + \frac{\Delta\vartheta}{2})\right\}\;\Delta\varphi \tag{A.9}$$

$$= 2\sin(\vartheta_i)\sin(\frac{\Delta\vartheta}{2})\;\Delta\varphi \tag{A.10}$$

Towards the equator

$$\int\limits_{\varphi_j-\frac{\Delta\varphi}{2}}^{\varphi_j+\frac{\Delta\varphi}{2}} \int\limits_{\vartheta_{\hat{I}+1}-\frac{\Delta\vartheta}{2}}^{\alpha} \sin\vartheta\;\partial\vartheta\;\partial\varphi = \Delta\varphi\,[-\cos\vartheta]_{\vartheta_{\hat{I}+1}-\frac{\Delta\vartheta}{2}}^{\alpha} \tag{A.11}$$

$$= \Delta\varphi\left\{\cos(\vartheta_{\hat{I}+1} - \frac{\Delta\vartheta}{2}) - \cos\alpha\right\} \quad . \tag{A.12}$$

Pole

At the pole

$$\int_{\varphi_j-\frac{\Delta\varphi}{2}}^{\varphi_j+\frac{\Delta\varphi}{2}}\int_{0}^{\alpha}\sin\vartheta\,\partial\vartheta\,\partial\varphi = \Delta\varphi\,[-\cos\vartheta]_0^{\alpha} \tag{A.13}$$

$$= \Delta\varphi(1-\cos\alpha) \tag{A.14}$$

$$= 2\Delta\varphi\sin^2(\frac{\alpha}{2}) \quad . \tag{A.15}$$

or

$$\int_{\varphi_j-\frac{\Delta\varphi}{2}}^{\varphi_j+\frac{\Delta\varphi}{2}}\int_{0}^{\frac{\Delta\vartheta}{2}}\sin\vartheta\,\partial\vartheta\,\partial\varphi = \Delta\varphi\,[-\cos\vartheta]_0^{\frac{\Delta\vartheta}{2}} \tag{A.16}$$

$$= \Delta\varphi(1-\cos\frac{\Delta\vartheta}{2}) \tag{A.17}$$

$$= 2\Delta\varphi\sin^2(\frac{\Delta\vartheta}{4}) \quad . \tag{A.18}$$

Equator

At the equator

$$\int_{\varphi_j-\frac{\Delta\varphi}{2}}^{\varphi_j+\frac{\Delta\varphi}{2}}\int_{\frac{\pi}{2}-\frac{\Delta\vartheta}{2}}^{\alpha}\sin\vartheta\,\partial\vartheta\,\partial\varphi = \Delta\varphi\,[-\cos\vartheta]_{\frac{\pi}{2}-\frac{\Delta\vartheta}{2}}^{\alpha} \tag{A.19}$$

$$= \Delta\varphi\left\{\cos(\frac{\pi}{2}-\frac{\Delta\vartheta}{2})-\cos(\alpha)\right\} \tag{A.20}$$

$$= \Delta\varphi\left\{\sin(\frac{\Delta\vartheta}{2})-\cos(\alpha)\right\} \quad . \tag{A.21}$$

A.3.3 Overall Formulation

- $0 \leq \alpha \leq \frac{\Delta\vartheta}{2}$:

$$P(\alpha) \approx 2\Delta\varphi\sin^2(\frac{\alpha}{2})\sum_{j=1}^{J}|G[0,\varphi_j]|^2 \tag{A.22}$$

- $\frac{\Delta\vartheta}{2} < \alpha \leq \frac{\pi}{2} - \frac{\Delta\vartheta}{2}$, with $\hat{I} = \text{round}\{\frac{\alpha}{\Delta\vartheta}\}$

$$P(\alpha) \approx \Delta\varphi \left\{ 2\sin^2(\frac{\Delta\vartheta}{4}) \sum_{j=1}^{J} |G[0,\varphi_j]|^2 + \right. \tag{A.23}$$

$$+ \; 2\sin(\frac{\Delta\vartheta}{2}) \sum_{i=2}^{I-1} \sum_{j=1}^{J} |G[\vartheta_i,\varphi_j]|^2 \sin(\vartheta_i) \; + \tag{A.24}$$

$$\left. + \; \left\{ \cos(\vartheta_{\hat{I}+1} - \frac{\Delta\vartheta}{2}) - \cos\alpha \right\} \sum_{j=1}^{J} |G[\frac{\pi}{2},\varphi_j]|^2 \right\} \tag{A.25}$$

- $\frac{\pi}{2} - \frac{\Delta\vartheta}{2} < \alpha \leq \frac{\pi}{2}$:

$$P(\alpha) \approx \Delta\varphi \left\{ 2\sin^2(\frac{\Delta\vartheta}{4}) \sum_{j=1}^{J} |G[0,\varphi_j]|^2 + \right. \tag{A.26}$$

$$+ \; 2\sin(\frac{\Delta\vartheta}{2}) \sum_{i=2}^{I-1} \sum_{j=1}^{J} |G[\vartheta_i,\varphi_j]|^2 \sin(\vartheta_i) \; + \tag{A.27}$$

$$\left. + \; \left\{ \sin(\frac{\Delta\vartheta}{2}) - \cos(\alpha) \right\} \sum_{j=1}^{J} |G[\frac{\pi}{2},\varphi_j]|^2 \right\} \tag{A.28}$$

Bibliography

[1] H. Heidt, J. Puig-Suari, A. Moore, S. Nakasuka, and R. Twiggs, “CubeSat: A new generation of picosatellite for education and industry low-cost space experimentation,” 2000.

[2] J. Puig-Suari, C. Turner, and W. Ahlgren, “Development of the standard CubeSat deployer and a CubeSat class picosatellite,” in *2001 IEEE Aerospace Conference Proceedings (Cat. No.01TH8542)*, 2001, pp. 1/347–1/353 vol.1.

[3] A. Chin, R. Coelho, R. Nugent, R. Munakata, and J. Puig-Suari, “CubeSat: the picosatellite standard for research and education,” in *AIAA Space 2008 Conference & Exposition*, 2008, p. 7734.

[4] C. Balanis, *Antenna theory: analysis and design*. Wiley, 1997.

[5] D. H. Johnson, *Array signal processing:concepts and techniques*. Englewood Cliffs, NJ : P T R Prentice Hall, 1993.

[6] M. J. Bentum, C. J. M. Verhoeven, and A. J. Boonstra, “OLFAR - orbiting low frequency antennas for radio astronomy,” in *Proceedings of the ProRISC 2009, Annual Workshop on Circuits, Systems and Signal Processing, Veldhoven*, November 2009, pp. 1–6.

[7] M. Ayre, I. Izzo, and L. Pettazzi, “Self assembly in space using behaviour based intelligent components,” in *Proceedings of the Towards Autonomous Robotic Systems: Incorporating the Autumn Biro-Net Symposium*, Imperial College, London, United Kingdom, September 2005.

[8] D. Izzo and L. Pettazzi, “Autonomous and distributed motion planning for satellite swarm.” *Journal of Guidance, Control, and Dynamics*, 2007.

[9] D. H. Werner and R. Mittra, “The theory and design of fractal antenna arrays,” in *Frontiers in Electromagnetics*, 1st ed. Wiley-IEEE Press, 2000, ch. 3, pp. 94–203.

[10] C. Puente-Baliarda and R. Pous, “Fractal design of multiband and low side-lobe arrays,” *Antennas and Propagation, IEEE Transactions on*, vol. 44, no. 5, pp. 730–739, May 1996.

[11] J. R. Wertz, D. F. Everett, and J. J. Puschnell, *Space Mission Engineering: The New SMAD*. Microcosm Press, 2011.

[12] *CubeSat Design Specifications (Rev 13); last accessed on 02/05/2017*, CubeSat Organisation. [Online]. Available: www.cubesat.org/resources/

[13] 1U Cubesat; last accessed on 02/05/2017. [Online]. Available: https://www.nasa.gov/sites/default/files/thumbnails/image/m15-146_lunar_orbiter_cubesat.jpg

[14] PPOD Orbital Deployer; last accessed on 02/05/2017. [Online]. Available: https://www.researchgate.net/figure/264854518_fig5_Figure-11-Poly-Pico-Satellite-Deployer-Cal-Poly-SLO-2010.png

[15] P. Fortescue, G. Swinerd, and J. Stark, *Space System Engineering*. Wiley, 2011.

[16] J. Straub, “CubeSats: A low-cost, very high return space technology,” in *Reinventing Space Conference*, 2012.

[17] Surrey Satellite Technology Ltd.: Microsat-100; last accessed on 02/05/2017. [Online]. Available: http://space.skyrocket.de/doc_sat/sstl_microsat-100.htm

[18] L. Muhammad, A. Ali, and I. Iliya, “Security challenges for building knoweldge-based economy is Nigeria,” *International Journal of Security and Its Applications*, vol. 9, no. 1, pp. 119–124, 2015.

[19] E. Kulu. Nanosatellite database. [Online]. Available: www.nanosats.eu

[20] C. Anderson, C. Brunskill, and C. Guillo, “Small is the new big.” [Online]. Available: https://sa.catapult.org.uk/documents/10625/98458/Small+is+the+new+Big1.2.pdf/a669be4b-0881-4e36-8958-e85e41a19792

[21] E. Buchen, “Small satellite market observations,” in *Small Satellite Conference*, 2015.

[22] J. Wells, L. Stras, and T. Jeans, “Canada’s Smallest Satellite: The Canadian Advanced Nanospace eXperiment (CanX-1),” in *Small Satellite Conference*, 2003.

[23] Danish Technical University. [Online]. Available: http://www.dtusat.dtu.dk/

[24] L. Alminde, M. Bisgaard, D. Vinther, T. Viscor, and K. Ostergard, “Educational value and lessons learned from the AAU-Cubesat project,” in *Recent Advances in Space Technologies, 2003. RAST ’03. International Conference on. Proceedings of*, Nov 2003, pp. 57–62.

[25] S. Flagg, “Using nanosats as proof of concept for space science missions: QuakeSat as an operational example,” in *Small Satellite Conference*, 2004.

[26] K. Nakaya *et al.*, “Tokyo tech CubeSat: Cute-I,” in *21st International Communications Satellite Systems Conference and Exhibit*, 2003.

[27] C. Kitts *et al.*, “The Genesat-1 microsatellite mission a challenge in small satellite design,” in *Small Satellite Conference*, 2006.

[28] S. Speretta, M. T. P. Soriano, M. J. Bouwmeester, M. J. Carvajal-Godinez, A. Menicucci, M. T. Watts, M. P. Sundaramoorthy, J. Guo, and E. Gill, “CubeSats to Pocketqubes: Opportunities and challenges,” 2016.

[29] T. Vladimirova and A. da Silva Curiel, “ChipSat–a system-on-a-chip for small satellite data processing and control architectural study and FPGA implementation,” *Surrey Satellite Technology Ltd*, 2004.

[30] B. Klofas, “A survey of CubeSat communication systems,” in *CubeSat Developers Conference*, 2008.

[31] W. Beech, D. Nielsen, and J. Taylor, “AX.25 link access protocol for amateur packet radio,” Tucson Amateur Packet Radio Incoporation, Tech. Rep., 1998.

[32] Pumpkin Inc. CubeSat kit; last accessed on 02/05/2017. [Online]. Available: http://www.cubesatkit.com/

[33] Clyde Space 1U CubeSat structure; last accessed on 02/05/2017. [Online]. Available: https://www.clyde.space/products/4-cs-1u-cubesat-structure

[34] J. Constantine, Y. Tawk, C. Christodoulou, J. Banik, and S. Lane, “CubeSat deployable antenna using bistable composite tape-springs,” *IEEE Antennas ans Wirelesss Propagation*, vol. 11, 2012.

[35] J. Plaza *et al.*, “Xatxobeo: Small mechanisms for CubeSat satellites - antenna and solar array deployment,” in *Proceedings of the 40th Aerospace Mechanisms Symposium*, 2010.

[36] ESMAT (Estec Materials); last accessed on 02/05/2017. ESA. [Online]. Available: www:esmat.esa.int

[37] NASA electronic part and packaging program; last accessed on 02/05/2017. NASA. [Online]. Available: www.nepp.nasa.gov/npsl

[38] D. E. Johnson *et al.*, “Detection of configuration memory upsets causing persistent errors in SRAM-based FPGAs,” 2004.

[39] K. Holland and J. Tront, “Probability of latching single event upset errors in VLSI circuits,” 1991.

[40] P. Liden, P. Dahlgren, R. Johansson, and J. Karlsson, “On latching probability of particle induced transients in combinational networks,” 1994.

[41] R. Koga, S. Penzin, K. Crawford, and W. Crain, “Single event functional interrupt sensitivity in microcircuits,” 1997.

[42] R. Koga, “Single event functional interrupt sensitivity in EEPROMs,” 1998.

[43] G. Swift *et al.*, “Dynamic testing of xilinx virtex-II field programmable gate array (FPGA) input/output blocks (IOBs),” *IEEE Transactions Nuclear Science*, 2004.

[44] F. Irom and D. Nguyen, “Single event effect characterization of high density commercial NAND and NOR nonvolatile FLASH memories,” *IEEE Transactions on Nuclear Science*, 2007.

[45] C. Poivey *et al.*, “Heavy ion single event latch-up test of Virtex4 FPGA XC4VFX60,” Tech. Rep., 2007.

[46] T. Speers, J. J. Wang, B. Cronquist *et al.*, “0.25 um FLASH memory based FPGA for space applications,” 1999.

[47] K. LaBel and K. Barth, “Radiation effects on emerging technologies,,” 2000.

[48] R. M. Manning. (1993) Low cost spacecraft computers: Oxymoron or future trend?

[49] J. Rotteveel and A. Bonnema, “Thermal control issues for nano- and picosatellites,” 2005.

[50] M. Dowd. (2002) "How rad hard do you need? The changing approach to space parts selection.". Maxwell Technologies Microelectronics.

[51] K. LaBel and M. Gates, “Single-event-effect mitigation from a system perspective,” *IEEE Transactions on Nuclear Science*, 1996.

[52] B. Pratt, M. Caffrey, J. Carroll, P. Graham, K. Morgan, and M. Wirthlin, “Fine-grain SEU mitigation for FPGAs using partial TMR,” *IEEE Transactions on Nuclear Science*, 2008.

[53] F. Kastensmidt, L. Sterpone, L. Carro, and M. Reorda, “On the optimal design of triple modular redundancy logic for SRAM-based FPGAs,” 2005.

[54] C. Bolchini, A. Miele, and M. Santambrogio, “TMR and partial dynamic reconfiguration to mitigate SEU faults in FPGAs,” 2007.

[55] J. Johnson *et al.*, “Using duplication with compare for on-line error detection in FPGA-based designs,” 2008.

[56] D. Czajkowski, P. Samudrala, and M. Pagey, “SEU mitigation for reconfigurable FPGAs,” 2006.

[57] B. Sklar, *Digital Communications: Fundamentals and Applications*. Prentice Hall, 1988.

[58] S. B. Wicker, *Error Control Systems for Digital Communication and Storage*. Prentice Hall, 1995.

[59] V. Dubourg, J. Carayon, P. Danto, and G. Galea, “An innovative onboard computer for CNES microsatellites,” 2002.

[60] Global geostationary satellite coverage; last accessed on 02/05/2017. [Online]. Available: https://www.rap.ucar.edu/~djohnson/satellite/geo_coverage2.html

[61] Polar orbit satellite coverage; last accessed on 02/05/2017. [Online]. Available: http://www.rap.ucar.edu/~djohnson/satellite/coverage.html#polar

[62] L. J. Ippolito, *Radiowave Propagation in Satellite Communications*. Springer Publishing Company, Incorporated, 1986. [Online]. Available: http://chapters.comsoc.org/vancouver/NASAHandbook-Sec1.pdf

[63] *Attenuation by atmospheric gases*, International Telecommunications Union Std., 2005.

[64] *Characteristics of precipitation for propagation modeling*, International Telecommunications Union Std., 2003.

[65] M. Taraba, C. Rayburn, A. Tsuda, and C. MacGillivray, “Boeing’s CubeSat TestBed 1 attitude determination design and on-orbit experience,” in *Small Satellite Conference*, 2009.

[66] D. Bekker, T. Werne, T. Wilson, P. Pingree, K. Dontchev, M. Heywood, R. Ramos, B. Freyberg, F. Saca, B. Gilchrist, A. Gallimore, and J. Cutler, “A CubeSat design to validate the Virtex-5 FPGA for spaceborne image processing,” in *Aerospace Conference, 2010 IEEE*, March 2010, pp. 1–9.

[67] H. Kayal, F. Baumann, K. Briess, and S. Montenegro, “BEESAT: A Pico satellite for the on orbit verification of micro wheels,” in *3rd International Conference on Recent Advances in Space Technologies*, 2007, pp. 497–502.

[68] M. Richard, “Swisscube lessons learned after 2 years in space,” 2012.

[69] F. Aguado *et al.*, “The HumSat constellation,” in *Proceedings of the 61st International Astronautical Congress*, 2010.

[70] E. Gill, P. Sundaramoorthy, J. Bouwmeester, B. Zandbergen, and R. Reinhard, “Formation flying within a constellation of nano-satellites: The {QB50} mission,” *Acta Astronautica*, vol. 82, no. 1, pp. 110 – 117, 2013.

[71] U. S. Agency. (2014, April) The UK’s miniature space tech pioneer. [Online]. Available: https://www.gov.uk/government/case-studies/ukube-1

[72] C. Bridges, S. Kenyon, C. Underwood, and V. Lappas, “STRaND-1: The world’s first smartphone nanosatellite,” in *Space Technology (ICST), 2011 2nd International Conference on*, 2011, pp. 1–3.

[73] S. Arnold, R. Nuzzaci, and A. Gordon-Ross, “Energy budgeting for cubesats with an integrated FPGA,” in *Aerospace Conference, 2012 IEEE*, March 2012, pp. 1–14.

[74] GomSpace. [Online]. Available: http://gomspace.com/index.php?p=home

[75] Xilinx Fast Fourier Transform v7.1, product specification; last accessed on 02/05/2017. [Online]. Available: http://www.xilinx.com/support/documentation/ip_documentation/xfft_ds260.pdf

[76] J. Leitner, “Formation flying: The future of remote sensing from space,” NASA, Goddard Space Flight Center, MD, United States, Tech. Rep., 2004.

[77] E. A. Barnes and B. E. Bishop, “Utilizing navigational capability to control cooperating robotic swarms in reconnaissance- based operations,” *Proceedings of the 40th Southeastern Symposium on System Theory*, pp. 338–342, March 2008.

[78] S. Schwartz, “Cross-scale - multi-scale coupling in space plasmas,” ESA, Tech. Rep., December 2009.

[79] M. Bester, M. Lewis, B. Roberts, J. McDonald, D. Pease, J. Thorsness, S. Frey, D. Cosgrove, and D. Rummel, “THEMIS operations,” *Space Science Reviews*, vol. 141, no. 1-4, pp. 91–115, December 2008.

[80] P. R. Lawson, O. P. Lay, S. R. Martin, C. A. Beichman, K. J. Johnston, W. C. Danchi, R. O. Gappinger, S. L. Hunyadi, A. Ksendzov, B. Mennesson, R. D. Peters, D. P. Scharf, E. Serabyn, and S. C. Unwin, “Terrestrial planet finder interferometer 2006-2007 progress and plans - art. no. 669308,” *Techniques and Instumentation for Detection of Exoplanets III*, vol. 6693, pp. 69 308–69 308, September 2007.

[81] K. Danzmann, “LISA - An ESA cornerstone mission for the detection and observation of gravitational waves,” *Advances in Space Research*, vol. 32, no. 7, pp. 1233 – 1242, 2003.

[82] F. Sjoberg, A. Karlsson, and B. Jakobsson, “PROBA-3: A formation flying demonstration mission on the verge to be realised,” no. 654 SP, April 2008.

[83] G. Blackwood, O. Lay, A. Deininger, W.and Ahmed, R. Duren, C. Noecker, and B. Barden, “The StarLight mission: A formation-flying stellar interferometer,” *Proceedings of SPIE - The International Society for Optical Engineering*, vol. 4852, no. 2, pp. 463 – 480, February 2002.

[84] C. R. McInnes, “Velocity field path-planning for single and multiple unmanned aerial vehicles,” *Aeronautical Journal*, vol. 107, no. 1073, pp. 419–426, July 2003.

[85] H.-S. A. Kwang-Kyo Oh, Myoung-Chul Park, “A survey of multi-agent formation control,” *Automatica*, vol. 53, pp. 424–440, 2015.

[86] D. J. Bennet and C. R. McInnes, “Verifiable control of a swarm of unmanned aerial vehicles,” *Proceedings of the Institution of Mechanical Engineers, Part G: Journal of Aerospace Engineering*, vol. 223, no. 7, pp. 939–953, November 2009.

[87] C. R. McInnes, “Vortex formation in swarms of interacting particles,” *Physical Review E (Statistical, Nonlinear, and Soft Matter Physics)*, vol. 75, no. 3, March 2007.

[88] M. R. D’Orsogna, Y. L. Chuang, A. L. Bertozzi, and L. S. Chayes, “Self-propelled particles with soft-core interactions: Patterns, stability, and collapse,” *Physical Review Letters*, vol. 96, no. 10, pp. 1–4, March 2006.

[89] A. Maffett, “Array factors with nonuniform spacing parameter,” *Antennas and Propagation, IRE Transactions on*, vol. 10, no. 2, pp. 131 –136, March 1962.

[90] B. B. Mandelbrot, *The Fractal Geometry of Nature*. Henry Holt and Company, 1983.

[91] G. Punzo, “Fractal patterns in fractionated spacecraft,” in *62nd International Astronautical Congress*, 2011.

[92] G. Punzo, P. Karagiannakis, D. J. Bennet, M. Macdonald, and S. Weiss, “Enabling and exploiting self-similar central symmetry formations,” *IEEE Transactions on Aerospace and Electronic Systems*, vol. 50, no. 1, pp. 689–703, 2014.

[93] H. Schaub and J. Junkins, *Analytical mechanics of space systems*. Reston, Va.: American Institute of Aeronautics and Astronautics, 2003.

[94] L. King, G. Parker, S. Deshmukh, and J. Chong, “Study of interspacecraft coulomb forces and implications for formation flying,” *Journal of Propulsion and Power*, vol. 19, no. 3, pp. 497 – 505, May/June 2003.

[95] M. A. Peck, B. Streetman, S. C. M., and V. Lappas, “Spacececraft formation flying using Lorentz forces,” *Journal of the British Interplanetary Society*, vol. 60, pp. 263–267, 2007.

[96] J. Berryman and H. Schaub, “Static equilibrium configurations in geo Coulomb spacecraft formations,” in *Advances in the Astronautical Sciences/ American Institute of Aeronautics and Astronautics*, Copper Mountain, CO, United states, January 2005, pp. 51 – 68.

[97] U. Khan and J. M. F. Moura, “Distributing the Kalman filter for large-scale systems,” *IEEE Transactions on Signal Processing*, vol. 56, no. 10, pp. 4919–4935, November 2008.

[98] A. Bertrand and M. Moonen, “Distributed LCMV beamforming in a wireless sensor network with single-channel per-node signal transmission,” *IEEE Transactions on Signal Processing*, 2013.

[99] H.-A. Loeliger, “An introduction to factor graphs,” *IEEE Signal Processing Magazine*, vol. 21, no. 1, pp. 28–41, January 2004.

[100] I. Proudler, S. Roberts, S. Reece, and I. Rezek, “An iterative signal detection algorithm based on bayesian belief propagation ideas,” in *In 15th International Conference on Digital Signal Processing*, July 2007, pp. 355 – 358.

[101] K. Zarifi, S. Affes, and A. Ghrayeb, “Distributed processing techniques for beamforming in wireless sensor networks,” 2009.

[102] H. Ge, I. Kirsteins, and X. Wang, “Adaptive beamforming using distributed antenna arrays: Joint versus distributed processing,” in *Conference Record of the 44th Asilomar Conference on Signals, Systems and Computers*, 2010, pp. 1107 – 1111.

[103] J. Eickhoff, *Onboard Computers, Onboard Software and Satellite Operations: An Introduction*. Springer Publishing Company, Incorporated, 2011.

[104] R. M. Leahy and B. D. Jeffs, “On the design of maximally sparse beamforming arrays,” *IEEE Transactions on Antennas and Propagation*, vol. 39, no. 8, pp. 1178–1187, 1991.

[105] M. B. Hawes and W. Liu, “Sparse microphone array design for wideband beamforming,” in *2013 18th International Conference on Digital Signal Processing (DSP)*, 2013, pp. 1–5.